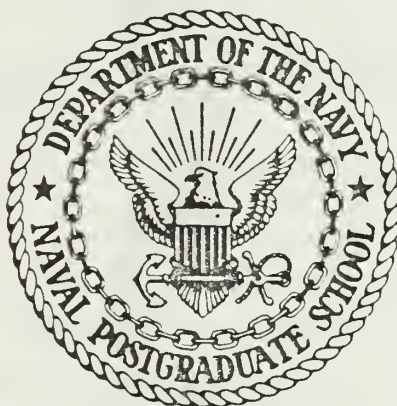


DUDLEY KNOX LIBRARY
NAVAL POSTGRADUATE SCHOOL
MONTEREY, CALIFORNIA 93943-5002

NAVAL POSTGRADUATE SCHOOL

Monterey, California



THESIS

A MOLECULAR DYNAMICS SIMULATION STUDY
OF SMALL SCALE SURFACE DEFECTS UPON
ATOM EJECTION PROCESSES

by

Steven Gregory Miller

December 1986

Advisor:
Co-advisor:

Don E. Harrison, Jr.
Karlheinz E. Woehler

Approved for public release; distribution is unlimited.

T232056

REPORT DOCUMENTATION PAGE

REPORT SECURITY CLASSIFICATION UNCLASSIFIED			1b. RESTRICTIVE MARKINGS			
SECURITY CLASSIFICATION AUTHORITY			3 DISTRIBUTION/AVAILABILITY OF REPORT Approved for public release; distribution is unlimited.			
DECLASSIFICATION/DOWNGRADING SCHEDULE						
PERFORMING ORGANIZATION REPORT NUMBER(S)			5 MONITORING ORGANIZATION REPORT NUMBER(S)			
NAME OF PERFORMING ORGANIZATION aval Postgraduate School		6b OFFICE SYMBOL (If applicable) 61	7a NAME OF MONITORING ORGANIZATION Naval Postgraduate School			
ADDRESS (City, State, and ZIP Code) onterey, California 93943-5000			7b. ADDRESS (City, State, and ZIP Code) Monterey, California 93943-5000			
NAME OF FUNDING/SPONSORING ORGANIZATION		8b. OFFICE SYMBOL (If applicable)	9 PROCUREMENT INSTRUMENT IDENTIFICATION NUMBER			
ADDRESS (City, State, and ZIP Code)			10 SOURCE OF FUNDING NUMBERS			
			PROGRAM ELEMENT NO	PROJECT NO	TASK NO	WORK UNIT ACCESSION NO
TITLE (Include Security Classification) MOLECULAR DYNAMICS SIMULATION STUDY OF SMALL SCALE SURFACE DEFECTS UPON ATOM EJECTION PROCESSES						
PERSONAL AUTHOR(S) Miller, Steven G.						
TYPE OF REPORT Master's Thesis		13b TIME COVERED FROM TO		14 DATE OF REPORT (Year, Month, Day) 1986 December		15 PAGE COUNT 116
SUPPLEMENTARY NOTATION						
COSATI CODES			18 SUBJECT TERMS (Continue on reverse if necessary and identify by block number)			
FIELD	GROUP	SUB-GROUP	Molecular Dynamics Simulation			
			Sputtering Processes			
			Rhodium/Argon System, Rh(111)/Ar ⁺			
ABSTRACT (Continue on reverse if necessary and identify by block number)						
<p>A molecular dynamics simulation has been used to investigate the sensitivity of atom ejection processes, from a single crystal target, to surface roughness (in the form of single and multiple surface vacancies and adatoms). A Rh(111)/Ar⁺ system was examined for normally incident ions at energies of 500 eV and 2 keV, using a modified Moliere/Morse atom-atom potential function. Comparisons are made between the effects of vacancies and adatoms on sputtering yield, ejection times, layer yield ratios, and ejected atom energy and angular distributions. Clean surface results are compared to those of a Born-Mayer/Morse potential function. Calculations show that the effects of vacancies exceed those of adatoms, requiring a surface density of 0.0153 vacancies/A² (at 500 eV) to produce a 5% change in the yield. The choice of the potential function affects the sputtering properties to the same degree as the surface defects, and tends to cast some doubt on quantitative results from this type of simulation.</p>						
DISTRIBUTION/AVAILABILITY OF ABSTRACT <input checked="" type="checkbox"/> UNCLASSIFIED/UNLIMITED <input type="checkbox"/> SAME AS RPT <input type="checkbox"/> DTIC USERS			21 ABSTRACT SECURITY CLASSIFICATION UNCLASSIFIED			
NAME OF RESPONSIBLE INDIVIDUAL Don E. Harrison, Jr.			22b TELEPHONE (Include Area Code) (408) 646-2877		22c OFFICE SYMBOL 61HX	

Approved for public release; distribution is unlimited.

A Molecular Dynamics Simulation Study
of Small Scale Surface Defects upon
Atom Ejection Processes

by

Steven Gregory Miller
Lieutenant, United States Navy
B.S., Carnegie-Mellon University, 1976

Submitted in partial fulfillment of the
requirements for the degree of

MASTER OF SCIENCE IN PHYSICS

from the

NAVAL POSTGRADUATE SCHOOL
December 1986

ABSTRACT

A molecular dynamics simulation has been used to investigate the sensitivity of atom ejection processes, from a single-crystal target, to surface roughness (in the form of single and multiple surface vacancies and adatoms). A Rh(111)/Ar⁺ system was examined for normally incident ions at energies of 500 eV and 2 keV, using a modified Molière/Morse atom-atom potential function. Comparisons are made between the effects of vacancies and adatoms on sputtering yields, ejection times, layer yield ratios, and ejected atom energy and angular distributions. Clean surface results are compared to those of a Born-Mayer/Morse potential function. Calculations show that the effects of vacancies exceed those of adatoms, requiring a surface density of 0.0153 vacancies/Å² (at 500 eV) to produce a 5% change in the yield. The choice of the potential function affects the sputtering properties to the same degree as the surface defects, and tends to cast some doubt on quantitative results from this type of simulation.

TABLE OF CONTENTS

LIST OF TABLES -----	6
LIST OF FIGURES -----	7
I. INTRODUCTION -----	11
A. WHAT IS SPUTTERING? -----	11
B. APPLICATIONS OF SPUTTERING -----	12
C. HISTORICAL OVERVIEW -----	13
D. COMPUTER MODELING -----	20
II. OBJECTIVES -----	24
III. THE MODEL -----	28
A. MULTIPLE INTERACTION (MI) SIMULATION -----	28
B. PHYSICAL CONSIDERATIONS -----	30
1. Lattice Orientation and Constants -----	30
2. Lattice Size and Containment Criteria ----	30
3. Statistical Ensemble -----	34
4. Adatom and Vacancy Placement -----	35
C. POTENTIAL FUNCTIONS -----	36
1. Background -----	36
2. Functional Form -----	38
3. Potential Functions Used in the Model ----	40
IV. RESULTS -----	43
A. OVERVIEW -----	43
B. SPUTTERING YIELDS -----	45
C. ATOMS EJECTED PER SINGLE ION -----	50

D.	EJECTION TIMES -----	51
E.	LAYER YIELD RATIOS -----	52
F.	EJECTED ATOM ENERGY DISTRIBUTIONS -----	52
G.	EJECTED ATOM ANGULAR DISTRIBUTIONS -----	53
H.	SPOT PATTERNS -----	54
I.	BORN-MAYER POTENTIAL FUNCTION -----	55
V.	CONCLUSIONS -----	58
	LIST OF REFERENCES -----	61
	APPENDIX: FIGURES -----	65
	INITIAL DISTRIBUTION LIST -----	115

LIST OF TABLES

1.	LATTICE DIMENSIONS -----	32
2.	500 eV ENSEMBLE RESULTS -----	35
3.	POTENTIAL FUNCTION PARAMETERS -----	42
4.	CUBIC SPLINE PARAMETERS -----	42
5.	QDYN OPERATING PARAMETERS -----	44
6.	NUMBER OF REFLECTED Ar IONS -----	47
7.	SURFACE DENSITY OF DEFECTS CAUSING $\pm 5\%$ DEVIATION IN YIELD -----	49
8.	COMPARISON OF RAW YIELDS -----	57

LIST OF FIGURES

To simplify notation, all figures that are comparisons of several sets of data will have the parameter(s) that are common to all data enclosed in parathesis. Energies listed here refer to the impacting argon ion energies.

1.	Yield vs. Lattice Size -----	66
2.	Lattice Plane Numbering System -----	67
3.	18x5x12 Lattice Numbering System -----	68
4.	21x6x17 Lattice Numbering System -----	69
5.	Impact Point Positions within the Representative Area -----	70
6.	Adatom Numbering System; 3-Fold Bridge Position ---	71
7.	Rhodium-Rhodium Potential Function, Comparison of RH74 and RHBM -----	72
8.	Rhodium-Rhodium Forces, Comparison of RH74 and RHBM -----	73
9.	Rhodium-Rhodium Potential Function, Comparison of RH7X and RHBM -----	74
10.	Rhodium-Rhodium Forces, Comparison of RH7X and RHBM -----	75
11.	Relative Vacancy Positions -----	76
12.	Relative Adatom Positions -----	77
13.	Yield vs. Distance from Center of Representative Area (500 eV); Comparison of: 1 Vacancy and 1 Adatom -----	78
14.	Yield vs. Distance from Center of Representative Area (2 keV); Comparison of: 1 Vacancy and 1 Adatom -----	79

15.	Yield vs. Distance from Center of Representative Area (1 Vacancy); Comparison of: 500 eV and 2 keV -----	80
16.	Yield vs. Distance from Center of Representative Area (1 Adatom); Comparison of: 500 eV and 2 keV -----	81
17.	Distributed Vacancy Positions -----	82
18.	Distributed Adatom Positions -----	83
19.	Atoms per Single Ion Distribution (500 eV); Comparison of: Clean Surface, 1 & 3 Vacancies, and 1 & 3 Adatoms -----	84
20.	Atoms per Single Ion Distribution (2 keV); Comparison of: Clean Surface, 1 & 3 Vacancies, and 1 & 3 Adatoms -----	85
21.	Atom Yield per Impact Point (500 eV) -----	86
22.	Atom Ejection Time Distribution (500 eV); Comparison of: Clean Surface, 1 & 3 Vacancies, and 1 & 3 Adatoms -----	87
23.	Atom Ejection Time Distribution (2 keV); Comparison of: Clean Surface, 1 & 3 Vacancies, and 1 & 3 Adatoms -----	88
24.	Yield Ratio vs. Size of Defect (500 eV) -----	89
25.	Yield Ratio vs. Size of Defect (2 keV) -----	90
26.	Energy Distribution (2 keV); Comparison of: 0, 1, 2, 3 & 7 Vacancies -----	91
27.	Energy Distribution (2 keV); Comparison of: 0, 1, 2, 3 & 7 Adatoms -----	92
28.	Energy Distribution (500 eV); Comparison of: 0 and 1 Vacancy -----	93
29.	Angular Distribution (Clean Surface); Comparison of: 500 eV and 2 keV -----	94
30.	Angular Distribution (2 keV); Comparison of: 1 Vacancy and 1 Adatom -----	95
31.	Angular Distribution (2 keV); Comparison of: 2 Vacancies and 2 Adatoms -----	96

32.	Angular Distribution (2 keV); Comparison of: 3 Vacancies and 3 Adatoms -----	97
33.	Angular Distribution (2 keV); Comparison of: 7 Vacancies and 7 Adatoms -----	98
34.	Angular Distribution (500 eV); Comparison of: 1 Vacancy and 1 Adatom -----	99
35.	Angular Distribution (500 eV); Comparison of: 2 Vacancies and 2 Adatoms -----	100
36.	Angular Distribution (500 eV); Comparison of: 3 Vacancies and 3 Adatoms -----	101
37.	Angular Distribution (500 eV); Comparison of: 7 Vacancies and 7 Adatoms -----	102
38.	Angular Distribution (2 keV); Comparison of: 0, 2 and 7 Vacancies -----	103
39.	Angular Distribution (2 keV); Comparison of: 0, 2 and 7 Adatoms -----	104
40.	Angular Distribution (500 eV); Comparison of: 0, 2 and 7 Vacancies -----	105
41.	Angular Distribution (500 eV); Comparison of: 0, 2 and 7 Adatoms -----	106
42.	Spot Patterns (Clean Surface); Comparison of: 500 eV and 2 keV -----	107
43.	Atoms per Single Ion Distribution (Clean Surface); Comparison of: 1) 500 eV, RH74 Potential 2) 500 eV, RHBM Potential 3) 2 keV, RH7X Potential 4) 2 keV, RHBM Potential -----	108
44.	Atom Ejection Time Distribution (Clean Surface); Comparison of: 1) 500 eV, RH74 Potential 2) 500 eV, RHBM Potential 3) 2 keV, RH7X Potential 4) 2 keV, RHBM Potential -----	109
45.	Energy Distribution (Clean Surface); Comparison of: 1) 500 eV, RH74 Potential 2) 500 eV, RHBM Potential 3) 2 keV, RH7X Potential 4) 2 keV, RHBM Potential -----	110

46.	Angular Distribution (Clean Surface, 500 eV); Comparison of: RH74 and RHBM Potentials -----	111
47.	Angular Distribution (Clean Surface, 2 keV); Comparison of: RH7X and RHBM Potentials -----	112
48.	Atom Yield per Impact Point (Clean Surface, 500 eV); Comparison of: RH74 and RHBM Potentials -----	113
49.	Atom Yield per Impact Point (Clean Surface, 2 keV); Comparison of: RH7X and RHBM Potentials -----	114

I. INTRODUCTION

A. WHAT IS SPUTTERING?

The ejection of surface atoms from solid surfaces under bombardment by energetic particles is known as sputtering. The particles may be ions, neutral atoms, neutrons, electrons or photons. Ejection is caused by collisions between the incoming particles and atoms in the selvage, i.e., the surface layers of the solid. The processes involved in sputtering are, in principle, similar to those causing radiation damage in the bulk of a solid. These processes occur far from thermal equilibrium, which means that sputtering is different from evaporation, which does occur at thermal equilibrium.

Generally, an incoming particle will collide with the atoms of the solid, thereby transferring energy to the atomic nuclei. If the energy transferred to an atomic nucleus is greater than the binding energy at the lattice site, a primary knock-on atom (PKA) is created. The PKA will collide with other target atoms distributing the energy by way of a collision cascade. An atom is sputtered if the energy transferred to it has a component normal to

the surface which is larger than the surface potential energy barrier¹.

One measure of sputtering is the sputtering yield, Y , defined as the mean number of atoms removed per incident particle. In counting the removed atoms, only those of the solid are included, while reflected ions or incident atoms that have been reemitted are not taken into account. The particles removed by sputtering are emitted with a broad distribution of energy, in different excitation and charge states, and at all exit angles. Differential yields are defined to describe the variation of the yield with these parameters.

B. APPLICATIONS OF SPUTTERING

Sputtering was long regarded as an undesirable effect which: i) destroys cathodes and grids in gas discharge tubes or ion sources, ii) contaminates a plasma and surrounding walls, making it a major research area in fusion technology, and iii) causes the destruction of diaphragms and targets in accelerators and in high-voltage electron microscopes. However, sputtering is used today for many applications and has become an indispensable process in modern technology.

¹ The potential energy of a surface layer atom is normally referred to as the surface binding energy (SBE). The SBE, however, only has meaning in an undamaged lattice and does not define the energy required to remove a surface atom once the collision process has begun.

Sputtering allows a controlled removal of tightly bound surface layers on a nearly atomic scale and possible submicron spacial resolution if a well focused or rastered beam is used. The atoms removed can be analyzed in a mass spectrometer, which gives information about surface concentration, or can provide a depth profile if the surface is continuously bombarded.

Both the removal of atoms from a surface and the flux of atoms leaving the surface are successfully applied, for example: in sputter ion sources, to obtain atomically clean surfaces; in micromachining; and for depth profiling of thin films and surfaces. One of the largest applications of sputtering is the deposition of thin films on a large variety of substrates. These films may be several square meters in area, or may be extremely small as in microelectronics.

C. HISTORICAL OVERVIEW

Sputtering has been investigated in most detail for bombardment of monatomic solids with mercury ions, with noble gas ions and with hydrogen ions. Sputtering yields may lie between 0 and 10^4 atoms per incident ion, but are typically one to five. The yields depend on: i) the incident particle's energy, mass and angle of incidence; ii) the mass of the target atoms; iii) the range of crystal

order² and the crystal orientation of the solid and iv) the surface binding energies of the target. The yield is, however, nearly independent of the temperature [Refs. 1, 2, 3]. Below a threshold energy, which is about 20-40 eV for normally incident ions, no sputtering takes place. Above this threshold the yield increases with incident ion energy and reaches a broad maximum in the energy region of 5-50 keV. At higher energies the sputtering yield decreases. This decrease is related to the larger penetration of the ions into the solid and the lower energy deposition into the surface layers.

Several versions of the theory of sputtering currently exist in the literature, each of which exhibits the propensities of their authors. Each version has some experimental support, but certain approaches are in better repute than others. This review makes no attempt to rationalize the various approaches, but rather it is concerned with providing a historical overview of the development of the theories.

Sputtering was first recorded in 1852 by Grove [Refs. 4, 5] who noticed the disintegration of cathodes in glow-discharge tubes with subsequent deposition of the material on the surrounding glass walls. This became known as

² The range of crystal order refers to the distance over which the crystal maintains the regular, repetitive gridlike arrangement of atoms, known as a lattice.

"cathode sputtering" in the literature. It took almost fifty years before Goldstein [Ref.6] presented compelling evidence that the sputtering effect was caused by positive ions of the discharge striking the cathode.

Unfortunately, early investigations of sputtering were wasted before it was realized that the pressure surrounding the target was a critical parameter and had to be low enough to allow the sputtered atoms to escape the surface. Many anomalies in early experimental results can be accounted for by the simple fact that the mean free path of the sputtered particles was less than the distance to some "collector surface", which allowed the liberated particles to diffuse back to the surface after collision with a gas atom. Penning and Moubis [Ref. 7] were the first to conclusively demonstrate the effect of ambient pressure, even though the view that pressure was an important factor had been held for a few years prior to their publication.

The work of Guntherschultze and Meyer [Refs. 8, 9] is one of the few early experiments preceding the findings of Penning and Moubis which satisfied the conditions for a reproducible sputtering determination. Guntherschultze and Meyer operated their discharge tube at relatively high vacuum (for that era) with a copper target and took the precautions of removing initial layers of the target material.

The elimination of adsorbed gases and surface oxide layers as a critical factor in determining the true yield was further described by Arifov, et al., in 1963 [Ref. 10]. Yonts and Harrison also presented evidence [Ref. 11] that surface recontamination from background gases was a significant factor in quantitative sputtering yield measurements. Criteria were therefore developed for conducting "clean" experiments. For a single crystal metal this means the removal of surface and near-surface damage and impurities by mechanical abrasion and polishing, with thermal annealing and "sputter cleaning" used to remove any residual damage. It is possible to go to greater lengths to ensure damage- and contaminant-free surfaces, for example, using low energy heavy ion bombardment to remove surface oxide (conducted in ultrahigh vacuum) followed by thermal annealing to remove surface damage caused by the ion bombardment. Information about the atomic structure of the surface can then be obtained by low energy electron diffraction (LEED), field ion microscopy or the new tunneling electron microscopy. Subsequent sputtering experiments could then be conducted in an ultrahigh vacuum environment (less than 10^{-10} Torr) to preclude adsorption of gas molecules on the surface.

The concept of an individual sputtering event on an atomic scale was first recognized and analyzed by Stark.

He originated the so-called 'hot-spot model' of sputtering [Ref. 12], and subsequently, a collision theory viewing sputtering as a sequence of binary collision events initiated by one bombarding ion at a time [Ref. 13]. Utilizing the conservation laws of the theory of elastic collisions and the concept of collision cross sections in his analysis, Stark correctly interpreted the observed energy dependence of the sputtering yield of hydrogen ions bombarding a metallic target.

Subsequent investigators took a different stand on the issue. After Kingdon and Langmuir successfully applied Stark's collision theory [Ref. 14], the erroneous impression arose that the collision theory would imply that sputtering was a single-collision process resulting in a strongly peaked angular distribution of the flux of sputtered particles. Only after the demonstration by Wehner [Refs. 15, 16] of crystal structure effects in the flux of sputtered particles did it become evident that local evaporation alone could hardly explain the sputtering phenomena. Wehner discovered that the angular distributions of the atoms ejected from single crystal targets showed maximum intensities in directions

¹ The hot-spot model was considered to be the evaporation of target material from a microscopically small region with a high local temperature due to individual ion impact.

corresponding to the more closely spaced atomic rows passing through the target surfaces.

The discovery of such ejection patterns or "Wehner spots" revived the interest in the collision theory of sputtering. Independently, Keywell [Refs. 17, 18] made a first attempt to formulate Stark's multiple-collision model in terms familiar from neutron transport theory. Keywell's work, as well as subsequent calculations by Harrison [Ref. 19] were important steps in the sense that probability concepts as expressed by collision cross sections finally made their entrance into sputtering theory.

The theory of collision cascades has been further advanced by the work of Leibfried [Ref. 20], Lindhard, et al. [Ref. 21], Dederichs [Ref. 22], Robinson [Ref. 23], Thompson [Ref. 24], and Sigmund [Refs. 25, 26], who has also collected the available knowledge in a transport theory of sputtering [Ref. 27]. In an amorphous solid the collision cascades have been described by a Boltzmann transport equation. Sigmund was able to obtain first order asymptotic solutions for the linear cascade regime*. However, only polycrystalline solids with randomly oriented crystallites can be approximated by an amorphous solid.

* The linear cascade regime applies to bombardment with ions of medium to large atomic number in the keV energy region. Here large collision cascades can develop, however, moving target atoms are considered to collide only with target atoms at rest.

Despite its shortcomings, this theory has become successful as a reference standard for sputtering yield measurements. It has also been a reasonable starting point for further refinements of the theory. During the rapid development of the theory of collision cascades, the hot-spot (or "spike") theory has received little attention despite repeated claims of a thermal component observed in energy spectra of sputtered atoms [Ref. 28].

In the period from 1955 to 1965, the dominant effort in the study of sputtering on metals was actually spent in the investigation of crystal lattice effects. These effects fell into two distinct groups, the channeling theory of the sputtering yield and the focusing collision theory of ejection patterns. The channeling theory accounts for the angular variations of the yield close to the principle crystal axes and planes, but is not very successful for more general directions. The focusing collision theory gives a qualitative description of the ejection pattern spots from cubic metals at high bombarding energies, but cannot successfully interpret low energy irradiation results or observations on hexagonal or other low symmetry materials. The discovery of spot patterns by Wehner [Refs. 15, 16] inspired Silsbee's identification [Ref. 29] of the focusing collision sequence as a means for long-range transport of momentum in crystals at low energy. An alternative to the focusing theory of the ejection pattern

spots was proposed by Lehmann and Sigmund [Ref. 30]. Their model stipulates that the target surface have an ordered structure, but not necessarily long straight rows of atoms intersecting the surface. This model emphasizes the role of surface structure and of the surface binding energy in monocrystal sputtering.

D. COMPUTER MODELING

In the past, sputtering theory needed only to predict the sputtering yield as a function of energy for a given incident particle and polycrystalline target of a single metal. The experimental environment led the theorists to statistical theories involving ensemble averages over distribution functions, ultimately culminating in the work of Thompson [Ref. 24] and Sigmund [Ref. 25] which predict the yield reasonably well. However, the chief limitation of these theories is their inability to deal with experimental results attributable to the regular structure in a single crystal target. As is the case with most theory, the statistical sputtering theories are also constrained by the lack of analytic tractability.

With the advent of high speed computing capabilities it became practical to include the full three-dimensional structures of crystals in the theoretical models of sputtering. The investigations of Vineyard and his colleagues [Ref. 31] demonstrated the power of computer simulations in isolating and understanding the elementary

processes of defect production and migration in radiation damage. Such techniques were first applied to monocrystal sputtering problems by Harrison and his co-workers [Ref. 32]. They proposed ejection mechanisms to account for the Wehner spots which differ from both the focusing collision theory and the model of Lehmann and Sigmund.

These computer simulations can be divided into two categories. Historically, the binary collision (BC) simulation models were developed first. The binary collision simulation is known as an "event store" model. The program follows a cascade of moving particles sequentially, moving only one particle at a time, but remembering events, i.e., collisions, as it progresses. The models usually invoke the binary collision approximation [Ref. 35]. This assumes that each particle interacts with only one other particle at any time, with the other particle usually considered to be stationary. Thus these models are inherently linear calculations and therefore they have many of the same restrictions as the linear transport calculations.

Initially, these models simply mimicked the statistical theories, then Robinson and Den included the target crystal structure [Ref. 33] and effectively discovered channeling. The channeling concept fed back into sputtering theory and Onterderlinden [Ref. 34] introduced the "channeling" sputtering model, which satisfactorily explained the

relative magnitude of the sputtering yield from single crystal target surfaces at low keV ion energies. Since their inception, the BC programs, MARLOWE [Ref. 35], TRIM [Ref. 36] and MORLAY [Ref. 37], have assumed that the physical model was well understood and that the simulation should be designed to compute results from it efficiently. Each program has its particular strengths and efficiencies, because each was designed to address specific criteria.

The second method of simulation is the multiple interaction (MI) simulation and is based on molecular dynamics. MI simulation was motivated by the work of Gibson, Goland, Milgram and Vineyard [Ref. 31], with the proponents of this model having concentrated on understanding the fundamentals of ejection processes.

This type of simulation is known as a "timestep" model and involves solving Newton's laws of motion, often expressed in Hamiltonian form, for many particles. These calculations proceed sequentially in time, following the collisions of many particles simultaneously. An advantage of the model is that there are no built in constraints as to the behavior of a collision cascade and, given enough cpu time and memory, will accurately follow an ion induced cascade to its ultimate thermalization.

A new development is that of a hybrid between the two types of codes by Harrison, et. al. [Ref. 38]. The goal of which is to have a simulation which retains the "exact"

treatment of the time step model in the surface region and minimizes computation time for the remainder of the cascade.

As the simulations have become increasingly more sophisticated, attention has turned to studying semiconductor materials. These materials present a distinct problem due to their nonspherical interatomic potentials. Computer modelling of silicon and other semiconductor materials may soon be a reality due to the pioneering work of B. J. Garrison in the use of embedded potential functions⁵.

⁵ Private communications between Professor B. J. Garrison of Pennsylvania State University and Professor D. E. Harrison, Jr. of the Naval Postgraduate School.

II. OBJECTIVES

Numerous experimental and theoretical investigations of the energy and angular distributions of atoms and molecules ejected from single crystal surfaces due to ion bombardment have been made over the years. Wehner was the first to observe spots, or anisotropic angular distributions [Ref. 15, 16]. His method of detection, however, did not allow him to distinguish the mass or energy of the ejected species. In more recent times energy and angular distributions of ions have been measured by angle-resolved Secondary Ion Mass Spectroscopy (SIMS) [Refs. 39, 40, 41, 42]. The theoretical investigations, mainly computer simulations, have been used to predict the distribution of neutral species [Refs. 43, 44, 45, 46]. These molecular dynamics calculations of the ion impact event have helped to i) formulate the mechanisms of particle emission from single crystal surfaces, ii) provide an atomistic picture of the damage created within the material itself, and iii) unravel the origin of angular anisotropies.

Experimental measurements of particle trajectories have not been possible at the level necessary to make direct comparisons to theoretical predictions. However, qualitatively and semi-quantitatively favorable comparisons have been made between the predicted neutral distributions

and the measured ion distributions [Refs. 40, 41, 42]. Rigorous quantitative comparisons are difficult since the ionization probability is not known. The ionization probability is required since the ions experience a different interaction potential than the neutrals as they leave the surface. In particular, it would be advantageous to be able to directly compare experimental and theoretical distributions in order to use the measured distributions to gain structural information about the surface and to improve the theoretical model so as to gain a better understanding of the scattering process.

With the recent advent of the energy- and angle-resolved neutral-particle (EARN) detector by N. Winograd, et. al. [Ref. 47], distributions for rhodium atoms ejected from clean and oxygen covered Rh(111) surfaces due to ion bombardment have been obtained [Refs. 48, 49, 50]. Energy and angular distributions reported by this method constitute the first reported neutral-particle ejection distributions for material desorbing from genuinely clean well-defined surfaces. Surface cleanliness and structure were monitored by low energy electron diffraction (LEED) and by Auger electron spectroscopy (AES) as well as by the reproducibility of the EARN measurements.

The results of computer simulations of argon ion bombardment of Rh(111) still do not correlate quantitatively with the reported EARN results. This lack

of correlation has provided the impetus to investigate possible mechanisms that could be the cause of the divergence between the simulated and experimental results. One of the assumptions that is commonly made in computer simulations is that the target surface is completely free of defects, i.e., atomically smooth. The degree of surface detail provided by LEED and AES in the EARN experiments does not preclude the presence of small scale topographical defects in the form of adatoms or vacancies. The only method that is currently available that could provide more precise characterization of the surface detail without disrupting the surface itself is scanning tunneling microscopy (STM) [Refs. 51, 52].

This study attempts to expand the scope of variables that are normally considered in computer simulations by investigating the effect of small scale surface defects, in the form of single and multiple adatoms and vacancies, on quantities such as the yield and the angle and energy distributions of sputtered particles. The Rh(111)/Ar⁺ system was chosen for investigation because the EARN experiments have set a new standard as being the most accurate, reproducible results obtained for sputtering to date, and provide the best baseline of experimental information. No attempt is made at this time to directly compare the results of the classical dynamics model to

experimental results, this being left for future studies when more experimental data becomes available.

III. THE MODEL

A. MULTIPLE INTERACTION (MI) SIMULATION

The MI simulation used to model the ion bombardment events is QDYN, developed by Professor Don E. Harrison, Jr. at the Naval Postgraduate School. A detailed description of the computer simulation method, the mathematical model it is based on, and the integration scheme have been published previously by Harrison, et. al. [Refs. 32, 53, 54].

Briefly, QDYN is a sputtering simulation which proceeds through a series of timesteps, each of which consists of the following: i) summation of the pairwise forces for each atom; ii) calculation of new velocities and positions at the end of the timestep; iii) movement of atoms to their new positions; and iv) test of energy conservation.

QDYN computes the interaction forces by performing a numerical solution of Hamilton's classical equations of motion, using a predictor-corrector integration scheme which bases the time increment of each step on the fastest moving particle. This differs from the form of most other numerical integrators because position and velocity are calculated for the same instant of time. More sophisticated integration schemes do not improve the calculations and only increase the computation costs.

The system consists of an incoming argon ion and a single-crystal rhodium target containing up to 1854 atoms. Each particle is characterized by i) its mass, ii) the force laws by which it interacts with other particles, iii) its position, and iv) its velocity. Once the incoming ion strikes the target at a specified impact point the positions and momenta of the ion and all the atoms in the single-crystal target are allowed to develop in time. This calculation, called a trajectory, is a simulation of a single collision cascade. The collision cascade is terminated when the momentum has dissipated through the lattice and no more atoms can be ejected. In this metallic rhodium system, this corresponds to a maximum particle energy, in the solid, of 2.0 eV. Finite lattice temperature effects and energy losses due to electronic excitations have not been included in this calculation.

Two ancillary programs were used to investigate each simulation. ANMOL analyzes the final positions and momenta to determine yields, the energy distribution, possible multimer formation, and the angular distribution of the ejected atoms, all of which are experimentally measurable quantities. In addition, information about atoms ejected per single ion (ASI) and ejection times is provided. Graphical representations of the distributions and quantities mentioned above were provided by ANPLOT. An alternate output available from QDYN allows sufficient

information to be printed out so that the collision cascade can be traced.

B. PHYSICAL CONSIDERATIONS

1. Lattice Orientation and Constants

A Rh{111} orientation was chosen to match the conditions of the energy- and angle-resolved neutral-particle (EARN) experiments [Refs. 48, 49, 50]. Rhodium is a face centered cubic (fcc) metal with a lattice constant (a_0) of 3.804Å. Other physical constants of rhodium used in the development of a Rh-Rh potential function, include: the bulk heat of atomization (5.76 eV) and the bulk compressibility (3.626×10^{-7} cm²/kg).

The basic distance unit defined for this simulation is the lattice unit (LU), which is one half the lattice constant for cubic materials.

$$1 \text{ LU} = 0.5 a_0 = 1.902\text{\AA}$$

2. Lattice Size and Containment Criteria

To model the 5 keV bombardment of the EARN experiments and describe most of the ejection events would require a target size that is computationally not feasible. In order to gain the most complete information about the Rh{111}/Ar⁺ system this study conducted its computations at ion bombardment energies of 500 eV and 2 keV. These energies and their corresponding lattice size were chosen in order to 1) optimize containment of the collision

cascade within the lattice, ii) maximize the number of atoms sputtered to ensure statistical confidence in the results, and iii) minimize the computational time necessary to complete a simulation.

The inability of the lattice of target atoms to contain the entire cascade created by the incident ion is called a failure of "containment". In principle, there is no problem for a moderate-size computer to store the information for even tens of thousands of atoms, but, in practice, running time considerations (i.e., money) limit the target to roughly 2000 atoms. Cascades created by keV ions are known to involve many more than 2000 atoms, so the problem seems insoluble. After long experience with these computations, Harrison has defined a more practical definition of containment [Ref. 55]: "If an increase in target size does not change the results of the computation, the trajectory is effectively contained for the purposes of that computation".

In practice, for any observable, one finds that containment is approached asymptotically as the target size increases. Harrison also states that:

As one might anticipate from experimental experience with absolute values, yield provides the most severe test of containment; so absolute yield containment guarantees everything else. As the target size increases, all other global results reach constant values for much smaller targets than those required to produce stable yield values.

This fact is born out by Figure 1, which is a graphical summary of numerous calculations done on clean Rh{111} at various ion energies and lattice sizes. These calculations provide the baseline information on clean Rh{111} as well as acting as verification of containment.

The following lattice sizes (see Table 1) correspond to the information provided in Figure 1. The lattice dimensions are given in terms of the number of lattice planes in the x, y, and z directions. Figure 2 provides a graphical description of the lattice plane numbering system.

TABLE 1
LATTICE DIMENSIONS

Lattice Dimension	# Rh Atoms in the Lattice
18 x 5 x 12	541
18 x 6 x 12	648
21 x 5 x 13	683
21 x 6 x 13	820
23 x 6 x 15	1036
25 x 6 x 17	1276
27 x 6 x 19	1540
25 x 8 x 17	1701

The lattice sizes chosen for the computations were:

Ion Energy	Lattice Size
500 eV	18 x 5 x 12
2000 eV	25 x 6 x 17

Even though appreciable movement of the edge atoms was observed prior to the last atom leaving the surface, the significant features of the dynamics were not altered

when a larger lattice size was used. All simulations were run on an IBM 3033 at the Naval Postgraduate School with computation times on the order of 1 CPU hour for the 500 eV simulations, and 3 CPU hours for the 2 keV simulations.

For the $18 \times 5 \times 12$ lattice there are 108 atoms in the first layer and for the $25 \times 6 \times 17$ lattice there are 213 atoms. To aid in describing the simulation events all atoms (and ions) in the simulation are numbered, with the ion being number 1 and the lattice atoms numbered beginning with number 2 at the origin and progressing upward across the rows, one layer at a time. Figures 3 and 4 delineate the numbering system for the first layer of each lattice system.

Another containment consideration deals with those atoms that leave the microcrystallite through the bottom and sides. The simulation program considers these atoms to be lost to the collision process, but continues to track them for energy conservation purposes until the model is terminated. This is justified for those atoms that depart the lattice through the bottom, since almost all of the collision events that contribute to sputtering occur in the first four layers of the lattice. The atoms that are ejected from the sides of the crystal are ignored in order to improve computational efficiency. Harrison, through long experience with this model has determined that the

deletion of these atoms has little impact on the number of atoms sputtered, altering the results by about 0.1%.

Alternate approaches to those atoms lost through the sides of the microcrystal would be: i) to reflect them at the side boundaries, or ii) to reintroduce them on the opposite side of the lattice from which they exited, with the same momenta.

3. Statistical Ensemble

An ensemble average is an average of any property over a group of similar systems. Simulations produce ensemble averages, where each trajectory is a sample from an ensemble of all possible trajectories realizable from a particular atom ejection. For a monatomic ion, each impact point on the target surface leads to a different trajectory. Using point and line symmetry transformations, one establishes a *representative area* in the target, which is an elementary symmetry zone of the surface of that lattice orientation. An ensemble of trajectories is developed by uniform sampling of the representative area.

For our purposes a rectangular representative area, of dimensions 0.707 LU by 1.225 LU, was chosen, with its origin placed at the center of a target atom (Figs. 3 and 4). Uniform sampling of the representative area was accomplished by designating 300 impact points within the rectangle (Fig. 5).

In order to reduce computation time, the necessity of using a uniform distribution of 300 trajectories was investigated. The impact points were divided into two groups of 150 points each (indicated by x's and +'s in Fig. 5) and the results of separate simulations of 500 eV Ar⁺ on clean Rh(111) were compared (Table 2).

TABLE 2
500 eV ENSEMBLE RESULTS

Number of trajectories	300	150 (x's)	150 (+ 's)
# Rh atoms sputtered	902	457	445
ASI	3.01	3.05	2.97
Average energy of sputtered Rh (eV)	13.272	13.192	13.355
1st layer yield ratio	0.970	0.969	0.971

Note: the x's and +'s denote the separate groups of impact points delineated in Figure 5.

In addition, the angular and energy distributions of the 150 trajectory simulations were identical in form, and nearly so numerically. Since all the measurable results were very similar, it was deemed prudent to conduct all subsequent simulations using only 150 trajectories (those designated by an x in Fig. 5).

4. Adatom and Vacancy Placement

Adatoms are placed at the 3-fold bridge position (Fig. 6) of a clean Rh(111) surface by designating, within the simulation, their relative position from a surface layer atom, as measured from atom center to atom center.

This corresponds to 2.187Å in the negative y direction and 1.560Å in the positive z direction from the surface atom. For simplicity, an adatom will be designated by the number of the surface atom with which it is associated (e.g., adatom 108). See Figure 6 for an example of this designating system, and Figures 3 and 4 for the atom numbering system.

Vacancies are treated in a much simpler fashion. At those positions where a vacancy is desired, the atom is simply removed from the lattice. The vacancy location is designated by the original atom's number (e.g., vacancy 52).

A perfect crystal lattice is always assumed in these simulations. No attempt is made to account for any distortion from the equilibrium position of atoms in the lattice due to the introduction of adatoms or vacancies. For example, the relaxing of surrounding atoms inward toward a vacancy.

C. POTENTIAL FUNCTIONS

1. Background

At present, the knowledge about interatomic potential is relatively good at large separation distances (i.e., in the region of equilibrium separation and greater), due to the large amount of experimental data available. Also, the theory is satisfactory at very small separations where nuclear scattering is predominant.

However, there is a serious lack of information in the region between the two extremes, which is normally compensated for by extrapolating either high energy or equilibrium potentials based on a reasonable physical model. The potentials used in sputtering models lie in this intermediate region and are therefore very approximate.

A typical two-body interatomic potential consists of an attractive part at large separation approaching a minimum in the region of equilibrium separation, then becoming repulsive and increasing rapidly as the interatomic separation decreases further and the closed shells of electrons of the atoms begin to overlap. The exact form of the interaction in the low energy region will differ for two atoms interacting in a crystal and in a diatomic molecule since in the former case it is influenced by atoms in its neighborhood.

Like the analytic theories, molecular dynamics simulations treat atom-atom repulsive interaction as two-body central forces. The assumption is made that the forces and potential energies are functions only of the properties of the atoms or ions and the internuclear separation. During an MI timestep, several atoms may be exerting forces on a single particle; so the resultant is calculated as a sum of the individual pair-wise interactions, improving the calculation.

Attractive forces are included in this model, even though they have little effect on the particle dynamics. They do, however, dominate the processes by which atoms escape the surface; so their magnitude strongly influence the atom yield from a single trajectory.

The cohesive energy and atom separation of the material determine a well depth and "width", establishing a reasonable approximation to a pair-potential well, but an attractive force range must be assumed. Prior to this study, test trajectories were run using nearest-neighbor, NN(1), interactions, next nearest-neighbor interactions, NN(2), etc., out to NN(4). In the fcc lattice, differences beyond NN(2) are very minor, so normally a potential function is truncated between NN(2) and NN(3). The well-depth of the attractive potential function is adjusted so that the calculated potential energy of an atom in the center of the target equals the heat of atomization of the target material.

2. Functional Form

Since the early days of the statistical theories it has been predicted that the sputtering yield would be relatively insensitive to the form of a particular interaction potential function [Refs. 27, 56]. The critical assumption in any sputtering calculation continues to be, however, the choice of the potential functions.

The potential functions used in this simulation are empirical in nature. They do, however, provide a more realistic view of the atomic interactions within a cascade than potentials derived exclusively from theoretical considerations which themselves contain approximations. The empirical potentials are based on simple analytic expressions which may or may not be justifiable from theory, and which contain one or more parameters adjusted to the model or deduced from crystal equilibrium data.

In general, the atom-atom potentials are compound functions consisting of a repulsive "wall", joined smoothly to an attractive section, the "well", by a cubic spline function. Much of the recent work has been done with the Born-Mayer function repulsive potential [Ref. 57],

$$V(r) = A \exp (-Br)$$

The parameters can be thought of as two degrees of freedom in the function corresponding to an ion size and hardness. Here the size is the separation at 1.0 eV, and the hardness is the pre-exponential factor A.

Many calculations have also been performed with a modified Molière potential. The original Molière form is:

$$V(r) = [(Z_1 Z_2 e^2 / a) / (r/a)] \phi(r/a)$$

$$\phi(r/a) = [0.35 \exp(-0.3 r/a) + 0.55 \exp(-1.2 r/a) + 0.10 \exp(-6.0 r/a)]$$

$$a = 0.8853 a_0 / [Z_1^{1/2} + Z_2^{1/2}]^{2/3} \quad (\text{Firsov screening length})$$

where a_0 is the Bohr radius, and Z_1 and Z_2 are the atomic numbers of the ion and atom respectively. Because this function is intended as an approximation to a Thomas-Fermi potential function, Torrens [Ref. 27] has shown justification for using the Firsov screening length, a , as an adjustable constant. The resulting function is called a modified Molière function: $a' = ka$.

The attractive portion of the compound potential function has the Morse potential function form:

$$V(r) = D_e [\exp\{-2\alpha(r - r_e)\} - 2\exp\{-\alpha(r - r_e)\}]$$

with D_e the well depth, r_e the equilibrium separation of an atom pair and α controlling the well width.

3. Potential Functions Used in the Model

For this study the atom-atom potential was chosen as a repulsive, modified Molière potential joined to an attractive Morse potential. The composite pair potentials V_{ij} between the i th and j th atoms separated by a distance R is given by:

$$\begin{aligned} V_{ij} &= A \exp(-BR) & R < R_a \\ V_{ij} &= C_0 + C_1R + C_2R^2 + C_3R^3 & R_a < R < R_b \\ V_{ij} &= D_e [\exp\{-2\alpha(R - R_e)\} - 2 \exp\{-\alpha(R - R_e)\}] & R_b < R < R_c \\ V_{ij} &= 0 & R \geq R_c \end{aligned}$$

The functions are joined smoothly by a cubic spline at points R_a and R_b . The modified Molière function is

truncated at R_C so only NN(1) and NN(2) interactions are included.

A Born-Mayer/Morse composite function used by Garrison [Ref. 58] is provided for comparison in this study, and is of the form:

$$V_{ij} = A \exp(-BR) \quad R < R_a$$

$$V_{ij} = C_0 + C_1R + C_2R^2 + C_3R^3 \quad R_a < R < R_b$$

$$V_{ij} = D_e[\exp\{-2\alpha(R - R_e)\} - 2 \exp\{-\alpha(R - R_e)\}] \quad R_b < R < R_c$$

$$V_{ij} = 0 \quad R \geq R_c$$

The interaction of Ar^+ with Rh is represented in both cases by a purely repulsive, unmodified Molière function:

$$V_{ij} = [(Z_1Z_2e^2/a)/(r/a)] \phi(r/a) \quad R < R_a$$

$$V_{ij} = 0 \quad R \geq R_a$$

The parameters that define the potential functions used in this study are presented in Tables 3 and 4. The modified Molière potential functions for both RH74 and RH7X are created by multiplying the Firsov length, a , by 0.740.

TABLE 3
POTENTIAL FUNCTION PARAMETERS

Designation	Rh-Rh RH74 ⁶	Rh-Rh RH7X ⁷	Rh-Rh RHBM ⁸	Ar-Rh
A (keV)	0.0	0.0	54.330	0.0
B (\AA^{-1})	0.0	0.0	-5.088	0.0
D _e (eV)	0.8237	0.7595	0.8237	0.0
R _e (\AA)	2.750	2.750	2.750	0.0
α (\AA^{-1})	1.080	1.080	1.560	0.0
R _a (LU)	0.73	0.73	0.70	2.20
R _b (LU)	0.80	0.80	0.85	2.20
R _c (LU)	2.20	2.20	2.40	2.20
k	0.740	0.740	1.0	1.0

TABLE 4
CUBIC SPLINE PARAMETERS

	Rh-Rh RH74	Rh-Rh RH7X	Rh-Rh RHBM
C ₀	-4.264x10 ³	-5.613x10 ³	4.469x10 ³
C ₁	1.666x10 ⁴	2.198x10 ⁴	-1.548x10 ⁴
C ₂	-2.159x10 ⁴	-2.859x10 ⁴	1.812x10 ⁴
C ₃	9.299x10 ³	1.235x10 ⁴	-7.130x10 ³

The Rhodium-Rhodium potential functions and forces of RH74 and RH7X are compared graphically with the RHBM function in Figures 7-10. The force between rhodium atoms is determined by taking the derivative of the analytic potential functions. The two force functions are then joined by a log-linear spline, which causes the distinctive break in the graphs as seen in Figures 8 and 10.

⁶ Function used in 500 eV Ar⁺ simulations.

⁷ Function used in the 2 keV Ar⁺ simulations.

⁸ Garrison's Born-Mayer/Morse potential function [Ref. 58].

IV. RESULTS

A. OVERVIEW

The results presented in this study are the product of a series of QDYN simulations totalling nearly 100 in number. Two basic avenues of investigation were pursued to determine the effects of small scale surface defects on sputtering. They include: i) the effect of the defect size on sputtering; and ii) the effect of the distance between a single surface defect and the representative area. The second area of investigation has provided a measure of the surface defect density required to induce a noticeable change in the sputtering.

The variation in sputtering as a function of defect size was examined by comparing a series of simulations that included a clean Rh(111) surface and surfaces containing 1, 2, 3, and 7 vacancies or adatoms. The locations of the defects, relative to the impact area, are depicted in Figures 11 and 12. Deviation in sputtering was similarly studied by comparing the results from a clean Rh(111) surface with simulations that included a single adatom or vacancy at various distances from the impact area. Both sequences of simulations were carried out at bombarding Ar⁺ energies of 500 eV and 2 keV. The investigation of several

side issues such as the comparison of potential functions and containment criteria (see Fig. 1) were also conducted.

Voluminous amounts of data were collected from this series of computer simulations. Presented here are portions of this information, assembled into a series of tractable comparisons, including: i) the effect of vacancies as compared to adatoms, and ii) the differences between simulations run with ion energies of 500 eV and 2 keV. The comparisons are made amongst various experimentally measurable quantities such as the energy and angular distribution of sputtered atoms to aid in discerning trends in the data. Various mechanisms are also discussed to account for the variations observed in these quantities.

Table 5 provides a summary of the operating parameters used in the majority of the Rh{111}/Ar⁺ simulations conducted for this study.

TABLE 5
QDYN OPERATING PARAMETERS

Ion energy (eV)	500	2000
Ion angle of incidence	90°	90°
Lattice dimensions	18x5x12	25x6x17
Rh-Rh potential function ⁹	RH74	RH7X
Ar-Rh potential function ¹⁰	Born-Mayer	Born-Mayer
Number of trajectories	150	150
Representative area pin point (atom #)	51	108

⁹ Modified Molière/Morse composite potential function. See Tables 3 and 4 for function parameters.

¹⁰ See Table 3.

B. SPUTTERING YIELDS

In his pursuit of containment of the sputtering process within the microcrystal of a simulation, Harrison has shown that: *"Only the first few layers of the target are needed to completely explain ALL experimental sputtering results, including the total yield"*. [Ref. 55] Since absolute containment is not achieved in this model the total yield will be low when compared to experimental results. All other computed quantities, however, will be very close to their "infinite crystal" values for the lattice sizes used in these simulations. Relative yields are therefore reported, with the values being normalized to the clean surface results.

Figures 13 - 16 detail the effect of a single defect on the normalized yield as measured by the defect's distance from the center of the representative area. The center of the representative area was chosen as the reference point rather than the pin point, since the impact points are almost uniformly distributed about the center.

For the low energy case a significant portion of the yield is initiated by the recoiling primary knock-on atom (PKA) or "target atom". The comparison at Ar⁺ energy of 500 eV (Fig. 13) indicates that a vacancy has a greater effect on the yield than an adatom does. This is to be expected, since the incoming ion has the opportunity to transfer its energy to a second layer atom through direct

collision, thereby involving atoms much deeper in the lattice. Subsequent collision sequences would distribute the energy through layers deeper in the microcrystal than would normally be expected. The likelihood of a surface atom having enough energy imparted to it to eject it from the surface (about 25 eV) is thereby decreased.

The presence of a peak at 1.5 LU for the adatom curve at Ar⁺ energy of 500 eV (Figs. 13 and 16), corresponding to an adatom at positions 42 and 61¹¹, cannot be reconciled by a similar mechanism and further study of the detailed collision sequence is required.

At Ar⁺ energy of 2 keV (Fig. 14), significant yield is attained from both the recoiling target atom and the scattered ion, where the "ion" yield is increased by contributions from second and third PKA's. Again, the vacancy has a greater effect on yield. This effect is most probably caused by the same mechanism described above, but in this case the energy is lost from the microcrystal by having more atoms ejected from the sides and bottom of the microcrystal, as compared to a clean surface.

The ability of a single adatom (at position 108) to increase the yield can be explained by visualizing the adatom being driven into the surface at an angle by the impacting ion. The propagating secondary collisions would

¹¹ See Fig. 3 for adatom positiona.

tend to be closer to the surface, than an ion impacting a clean surface. The recoiling atoms would then have an opportunity to transfer a greater portion of their momenta to the surface atoms directly, causing more atoms to be ejected. This effect is not present at 500 eV since the Ar⁺ is more likely to be reflected off the adatom. A brief comparison of reflected Ar⁺ is presented in Table 6 to support this hypothesis.

TABLE 6
NUMBER OF REFLECTED Ar IONS

Ion energy (eV)	500	2000
Clean surface	58	46
1 adatom*	96	56

*Note: adatoms are at the same positions relative to the representative area.

The scattering of data points for the 2 keV adatom case (Figs. 14 and 16) was investigated in some detail. The data points at approximately 1.8 LU correspond to adatoms at positions 95 (normalized yield of 1.028) and 120. While these adatoms are the same distance from the center of the representative area, they are not the same distance from each of the individual impact points. Where there existed a significant difference in yield per single ion, the sequence of collision was traced. The most significant difference between the two trajectories was the position on the surface where the ion actually made contact. This was caused by a slight difference in distance between the ion's

starting position and the adatom. The long range of the Ar-Rh potential function (2.2 LU for cutoff) caused the incoming ions to follow different paths to impact which yielded two different collision sequences. This was confirmed by reducing the Ar-Rh potential function cutoff to 1.6 LU, at which time the trajectory results coincided exactly. No trend can be observed for the dispersed data points as a whole concerning their relative positions to one another.

In general the graphs asymptotically approach a normalized yield of 1.0. This corresponds to the defect being moved farther from the area of collision events until it has no effect on the trajectories at all. The distance at which the curve reaches ± 5 percent of the clean surface results is an indication of the density of defects required to visibly affect the yield. This takes into account an average error of 3% as measured by the deviation of the curves from 1.0, and uses only the upper data points of the 2 keV adatom curve. Table 7 presents the approximate distances as determined from the straight line extrapolation of Figures 13 and 14, and the surface density corresponding to a circle enclosing a defect at that position.

TABLE 7
SURFACE DENSITY OF DEFECTS
CAUSING $\pm 5\%$ DEVIATION IN YIELD

	Distance of defect from center of representative area (LU)	Surface Density (defects/ \AA^2)
500 eV, 1 vacancy	1.69	0.0153
500 eV, 1 adatom	0.57	0.0539
2 keV, 1 vacancy	1.22	0.0237
2 keV, 1 adatom	0.63	0.0492

To add some credence to the predicted defect density results, simulations were run at 2 keV that evenly distributed the defects over the surface. Figures 17 and 18 depict the positions of the vacancies and adatoms respectively. The closest defect to the center of the representative area is actually outside the distance listed in Table 7 in order to provide a check on the outer limit of results. For the vacancies a raw yield of 957 was obtained, versus 1022 for a clean surface; a 6.4% decrease in the yield. The adatoms produced a raw yield of 1001, which is only a 2.1% decrease in yield; not quite the 5% that was desired.

The difficulty with the adatom case is that the next closest position, nearer the representative area, to place an adatom would have located it within the representative area. This was felt to be too biased a test to confirm the results, since it would have essentially duplicated the original simulation, and was therefore not conducted. Despite the lack of confirmation of the adatom results, I

believe the the defect densities necessary to produce a 5% change in the yield, as shown in Table 7, to be an accurate estimate.

C. ATOMS EJECTED PER SINGLE ION

With the advent of computer modelling the ability to determine a distribution of atoms ejected per single ion (ASI) became available. This quantity cannot be determined experimentally but it does present some insight into the mechanics of the system.

Figures 19 and 20 present a series of comparisons within a single ion energy regime for: a clean surface; 1 and 3 vacancies; and 1 and 3 adatoms. For the 500 eV case, little difference is seen between the clean surface distribution and both of the adatom results. This is as expected from the sputtering yield results, where adatoms have been shown to have little impact on the total yield.

Again, as expected from the sputtering yield results, vacancies have a significant effect on the ASI distribution. The mass of the distribution tends to shift to the left as the size of the pit formed by the vacancies gets larger, with the low yield trajectories becoming dominant.

At 2 keV much the same behavior can be seen happening to the distributions, with the same effect now being observable for the adatoms, but to a smaller extent when compared with the vacancy cases.

An alternate form of displaying the ASI distribution which accentuates the atom ejection process is shown in Figure 21. The number of rings in each circle is proportional to the ASI value for an impact point at the center of the circle. The resulting pattern indicates the areas of the representative area which produce high yield, or low, by the relative darkness of the circle. Since the RH(111) surface does not contain any true channels, there is no significant difference noted in any *atom yield per impact point* diagrams created during this study, Figure 21 being provided as an example only.

D. EJECTION TIMES

Figures 22 and 23 provide a comparison of ejection time distributions for Rh, within an ion energy regime, as they are affected by 1 and 3 vacancies, and 1 and 3 adatoms. At 500 eV there is a slight shift to lower ejection times for an increasing number of vacancies, and a very considerable shift for the adatom cases. The shift to lower ejection times at 2 keV is barely discernable in all cases.

The most significant fact that can be seen from these distributions is that more than 95% of the atoms ejected during the simulation occur prior to 250 femtoseconds ($1 \text{ fs} = 10^{-15} \text{ sec}$) for the 500 eV cases and prior to 300 fs at 2 keV.

E. LAYER YIELD RATIOS

The layer yield ratio is defined as $L_n = N_n/N$, where N_n is the number of ejected atoms which originally resided in the n th layer of the target, and N is the total number of atoms ejected. L_1 values at 500 eV and 2 keV are plotted in Figures 24 and 25. At both energies, the adatoms effectively act as a "new" first layer causing the yield ratio to decrease more rapidly than the vacancy cases.

For all cases, except at low energy and high number of defects, the ejected atoms come primarily from the first target layer. This agrees with Harrison's statement that: "Under all conditions 85% or more of the ejected atoms come from the surface layer of the target, and essentially all of the remainder come from the second layer". [Ref. 55] However, as the number of defects increase in the low energy case, the target is more able to accomplish a momenta reversal and have atoms ejected from deeper layers.

F. EJECTED ATOM ENERGY DISTRIBUTIONS

The ejected atom energy distributions were created by tallying the energy of all Rh atoms sputtered from the surface of the target (whether the Rh was single atoms or multimers) into energy bins 0.5 eV wide. Figures 26 - 28 are plots of the individual tallies. An attempt to plot a smooth curve through the data points is not made, since significant noise is present in the plotted values.

Figures 26 and 27 present information obtained from 2 keV simulations. It can be seen that there is little difference between the energy distributions as the number of defects increase. These distributions, as a group, can be viewed as one ensemble. By averaging the energy values in each bin, their statistical plausibility could be improved.

Figure 28 was compiled from simulations run at 500 eV with 300 trajectories each, since those completed using 150 trajectories did not contain enough information to discern anything beyond the noise.

By allowing the data points to be interpolated by eye, these energy distributions can be seen to follow a Maxwellian form, with a maxima at about 2.5 eV. Additionally, there is a slight secondary peak at 9.3 eV for the 2 keV cases and one at 8.0 eV for the 500 eV graph. At this time no explanation is forwarded to account for these secondary peaks.

G. EJECTED ATOM ANGULAR DISTRIBUTIONS

Since a major thrust of Garrison's work [Ref. 58] has been to explain the location of the peak of the polar angle distributions, as compared to experimental results [Refs. 48 - 50], an extensive group of plots (Figures 29 - 41) has been developed to compare the effect of ion energy and defect size on the distributions.

The polar angle distributions are created by tallying only those ejected Rh atoms with energies greater than 5.0 eV and summing over all azimuthal angles. Discriminating against the very low energy species will help align the results more closely with the experimental measurements.

At 2 keV the shift in the distribution is very slight with the vacancies forcing the distribution to smaller angles and the adatoms to larger ones. This effect is much more pronounced in the 500 eV results, with Figures 37, 40 and 41 showing the shifts most clearly. In general, as the number of defects increase; from a clean surface through 1, 2, 3, and 7 defects^{1,2}; the amount of the shift in the peak increases.

H. SPOT PATTERNS

An alternate method for displaying angular distribution is the sputtered atom spot pattern. Unlike the angular distributions discussed in section G above, this method reveals both the azimuthal and polar angle dependence of the sputtered atoms simultaneously.

Little difference was noted between the spot patterns of the simulations conducted for this study, therefore only two examples are presented here for illustration (Figure

^{1,2} See Figs. 11 and 12 for relative position of defects.

42). Of note is the expected six-fold symmetry of the pattern characteristic of a fcc(111).

These graphs were produced by plotting the ejection angles of all sputtered atoms. To obtain spot patterns more similar to those experimentally obtained, such as SIMS data, many more trajectories would be required (on the order of 1000). Atoms ejected with energy less than 5.0 eV would then be eliminated to produce a sharper image.

I. BORN-MAYER POTENTIAL FUNCTION

The majority of theoretical work on the Rh(111)/Ar⁺ system has been conducted at Pennsylvania State University by B. J. Garrison [Ref. 58], in conjunction with the experimental studies of N. Winograd, et. al. [Refs. 48-50]. Due to the close collaboration between Professor Harrison and Professor Garrison, it was considered de rigueur to compare the results obtained using the Born-Mayer Rh-Rh potential function (RHBM) with the modified Molière potential function, which is used throughout this study (refer to Chapter 3, section D.3 for details of these functions).

Simulations were run on clean surfaces only, at ion energies of 500 eV and 2 keV. Significant differences in results are apparent. Summaries of the graphical comparisons are listed below, with the statements being couched as to the effect of the RHBM function when compared to the Molière function.

- 1) Figure 43. Atoms sputtered per single ion (ASI):
At 500 eV a noticeable shift to lower ASI is observed, with only a minor shift appearing at 2 keV.
- 2) Figure 44. Atom ejection time distribution: At both energies a shift to lower ejection times is evident, with the times required for 95% ejection being reduced by 60 fs.
- 3) Figure 45. Ejected atom energy distribution: The data presented has a low order of confidence due to insufficient atoms ejected and the noise present in the distributions. However, some details can be determined. There is a slight shift to lower energies for both 500 eV and 2 keV cases, with a corresponding reduction in the maxima.
- 4) Figures 46 and 47. Ejected atom angular distributions: These figures present the most dramatic differences between the potential functions, with the RHBM results being very sharply peaked at 25° for both energy regimes, compared to broad distributions peaking at larger angles for the Molière results.
- 5) Figures 48 and 49. Atom yield per impact point: These figures are presented for general information. No significant differences were noted.

Table 8 presents the raw yields for each of the four simulations compared, and a percent change in the yields, to emphasize the magnitude of the effect the choice of potential function can have.

TABLE 8
COMPARISON OF RAW YIELDS

Ion Energy (eV)	500	2000
Yield (RHBM)	376	1032
Yield (RH74, RH7X)	457	1022
Percent change	-18	+1

V. CONCLUSIONS

While this study has made no attempt to compare the simulation results to experimental results that are currently available, it has demonstrated that the presence of defects on single crystal surfaces can produce measurable differences in the quantities that characterize sputtering. By investigating yet another variable in the simulation of sputtering, this study has laid to rest some of the criticisms leveled against the simulations in general, e.g., a simulation's lack of accuracy due to the incomplete modelling of the system. In the future, the placement of vacancies and adatoms may be considered when any system is modelled in order to provide: i) a more accurate prediction of experimental results, ii) possibly greater correlation with the existing experimental results, and iii) greater insight into the actual sputtering mechanisms as simulations more closely reflect actual sputtering events. These statements are predicated upon the assumption that future experiments will be conducted with the precision evident in the EARN experiments conducted by N. Winograd, et. al. [Refs. 48 - 50].

The correct choice of a modified Molière/Morse potential over a Born-Mayer/Morse potential was verified when the results of the simulations were compared to preliminary

EARN results [Ref. 58]. Garrison's simulations, using the RHBM potential function, fail to correctly predict the peaks occurring in the angular and energy distributions, while the simulation results of this study are a very good correlation for the angular distribution only. Correlation of the energy distribution is left for later studies.

The choice of potential function does, however, cloud the issue of the effect of the surface defects. The choice of an appropriate potential function is still considered to be a "black art", since little is known of the behavior of potential functions in general at the low energies at which the sputtering processes operate. The choice of an appropriate function only has to fit a few parameters, such as the surface atomization energy of the crystal. Beyond that, the person creating the model's environment has wide latitude.

The magnitude of the effect of the potential function choice is at least as great as that of the surface defects reported here, so it can be argued that possibly an incorrect potential function was chosen for this model. I do not believe that this is born out by the results presented in this study. Surface defects exist on all surfaces used in experiments and simulations should take them into account.

Future studies into the $\text{Rh}(111)/\text{Ar}^+$ system using QDYN simulations should increase the ion energy to 5 keV to

match the experiments currently being conducted in this area. Also, more attention should be paid to investigating the mechanisms that may be responsible for the results observed, by tracing the progress of the collision events.

LIST OF REFERENCES

1. J. Bohdanský, J. Roth, A. P. Martenelli, Fourth Intern. Conf. Solid Surfaces, Paper 344 (Cannes 1980).
2. K. Besoke, S. Berger, W. O. Hofer, U. Littmark, Radiat. Eff. 66, 35 (1982).
3. W. O. Hofer, K. Besoke, B. Stritzker, Appl. Phys. A 30, 83 (1983).
4. W. R. Grove, Trans. Roy. Soc. (London) 142, 87 (1852).
5. W. R. Grove, Philos. Mag. 5, 203 (1853).
6. E. Goldstein, Verh. Dtsch. Phys. Ges. 4, 228, 237 (1902).
7. F. M. Penning and J. H. A. Moubis, Koninkl. Ned. Akad. Wetenschap. Proc. 43, 41 (1940).
8. A. Guntherschultze and K. Meyer, Zeits. f. Physik 62, 607 (1931).
9. K. Meyer and A. Guntherschultze, Zeits. f. Physik 71, 279 (1931).
10. U. A. Arifov, Radio Tekhnika i Elektronika 8, 1, 138 (1963).
11. O. C. Yonts and D. E. Harrison, Jr., J. Appl. Phys. 31 (9), 1583 (1960).
12. J. Stark, Die Elektrizitat in Gasen (Barth, Leipzig 1902).
13. J. Stark, Z. Elektrochem. 14, 752 (1908); 15, 509 (1909).
14. K. H. Kingdon and I. Langmuir, Phys. Rev. 20, 107 (1922); 21, 210 (1923); 22, 148 (1923).
15. G. K. Wehner, Phys. Rev. 102, 690 (1956).
16. G. K. Wehner, J. Appl. Phys. 26, 1056 (1955).
17. F. Keywell, Phys. Rev. 87, 160 (1952).

18. F. Keywell, Phys. Rev. **97**, 1611 (1955).
19. D. E. Harrison, Jr., Phys. Rev. 102, 1473 (1956); 105, 1202 (1957); J. Chem. Phys. 32, 1336 (1960).
20. G. Liebfried, J. Appl. Phys. 30, 1388 (1959).
21. J. Lindhard, V. Nielsen, M. Scharff, and P. V. Thomsen, K. Dan. Vidensk. Selsk. Mat. Fys. Medd. 33, 10 (1963).
22. P. H. Dederichs, Phys. Status Solidi 10, 303 (1965).
23. M. T. Robinson, Philos. Mag. 12, 145, 741 (1965).
24. M. W. Thompson, Philos. Mag. 18, 377 (1968).
25. P. Sigmund, J. B. Sanders, Proc. Int. Conf. Applications of Ion Beams to Semiconductor Technology, P. Glotin (Ed.), (Editions Ophrys, Grenoble 1967) p. 215.
26. P. Sigmund, Radiat. Eff. 1, 15 (1969).
27. P. Sigmund, Phys. Rev. 184, 383 (1969); 187, 768 (1969).
28. M. W. Thompson and R. S. Nelson, Philos. Mag. 7, 2015 (1962).
29. R. H. Sillsbee, J. Appl. Phys. 28, 1246 (1957).
30. C. Lehmann and P. Sigmund, Phys. Status Solidi 16, 507 (1966).
31. J. B. Gibson, A. N. Goland, M. Milgram, and G. H. Vineyard, Phys. Rev. 120, 1229 (1960).
32. D. E. Harrison, Jr., N. S. Levy, J. P. Johnson, III and H. M. Effron, J. Appl. Phys. 39, 3742 (1968).
33. M. T. Robinson and O. S. Oen, Appl. Phys. Letts. 2, 30 (1963).
34. D. Onderdelinden, Appl. Phys. Lett. 8, 189 (1966); and Can. J. Phys. 46, 739 (1965).
35. I. M. Torrens and M. T. Robinson, Phys. Rev. B **9**, 5008 (1974).

36. J. P. Bierseck and L. G. Haggmark, Nucl. Instrum. Methods 174, 257 (1980).
37. E. Taglauer, U. Beitatt, G. Marin, and W. Heiland, J. Nuc. Materials 63, 193 (1976).
38. R. P. Webb, D. E. Harrison, Jr., and M. M. Jakas, Nucl. Instrum. Methods B 15, 1, (1986).
39. S. P. Holland, B. J. Garrison, and N. Winograd, Phys. Rev. Lett. 43, 220 (1979).
40. R. A. Gibbs, S. P. Holland, K. E. Foley, B. J. Garrison and N. Winograd, Phys. Rev. B 24, 6178 (1981).
41. R. A. Gibbs, S. P. Holland, K. E. Foley, B. J. Garrison and N. Winograd, J. Chem. Phys. 76, 684 (1982).
42. K. E. Foley, N. Winograd, B. J. Garrison, and D. E. Harrison, Jr., J. Chem. Phys. 80, 5254 (1984).
43. D. E. Harrison, Jr., Appl. Phys. Lett. 8, 33 (1966).
44. N. Winograd, B. J. Garrison, and D. E. Harrison, Jr., Phys. Rev. Lett. 41, 1120 (1978).
45. M. H. Shapiro, P. K. Haff, T. A. Tombrello, D. E. Harrison, Jr., and R. P. Webb, Radiat. Eff. 89, 234 (1985).
46. S. Kapur and B. J. Garrison, J. Chem. Phys. 75, 445 (1981); *ibid*, Surf. Sci. 109, 435 (1981).
47. P. H. Kobrin, J. P. Baxter, and N. Winograd, J. Vac. Sci. Technol. A 3, 1596 (1985).
48. P. H. Kobrin, G. A. Schick, J. P. Baxter, and N. Winograd, Rev. Sci. Instrum. 57, 1354 (1986).
49. J. P. Baxter, G. A. Schick, J. Subbiah-Singh, P. H. Kobrin, and N. Winograd, J. Vac. Sci. Technol., preprint of Angular Distribution of Sputtered Particles (1986).

50. N. Winograd, P. H. Kobrin, G. A. Schick, J. Subbiah-Singh, J. P. Baxter, and B. J. Garrison, Surf. Sci. Lett., preprint of Energy and Angle-Resolved Detection of Neutral Atoms Desorbed from Ion Bombarded Single Crystal. Rh(111) and p(2x2)O/Rh(111) (1986).
51. G. Binnig, H. Rohrer, Ch. Gerber, and E. Weibel, Surf. Sci. Lett. **131**, L379 (1983).
52. A. M. Baro, G. Binnig, H. Rohrer, Ch. Gerber, E. Stoll, A. Baratoff, and A. Salvan, Phys. Rev. Lett. **52**, 1304 (1984).
53. D. E. Harrison, Jr., W. L. Gay and H. M. Effron, J. Math. Phys. **10**, 1179 (1969).
54. D. E. Harrison, Jr., W. L. Moore, Jr. and H. T. Holcombe, Rad. Eff. **17**, 167 (1973).
55. D. E. Harrison, Jr., Radiat. Eff. **70**, 1 (1983).
56. P. Sigmund, Scattering by Particle Bombardment I, Topics in Applied Physics, Vol. 47, R. Berisch (Ed.), (Springer-Verlag, 1981).
57. I. M. Torrens, Interatomic Potentials, (Academic, New York, 1972).
58. B. J. Garrison, preprint of Energy and Angular Distribution of Rh Atoms from Rh(111): A Theoretical Study (1986).

APPENDIX: FIGURES

This appendix includes all figures referred to in the body of this report. The data presented in these figures are the measurement of various parameters of the ejected rhodium atoms. The energies presented on each graphic refer to the impacting argon ion energy utilized in that simulation.

YIELD VS. LATTICE SIZE

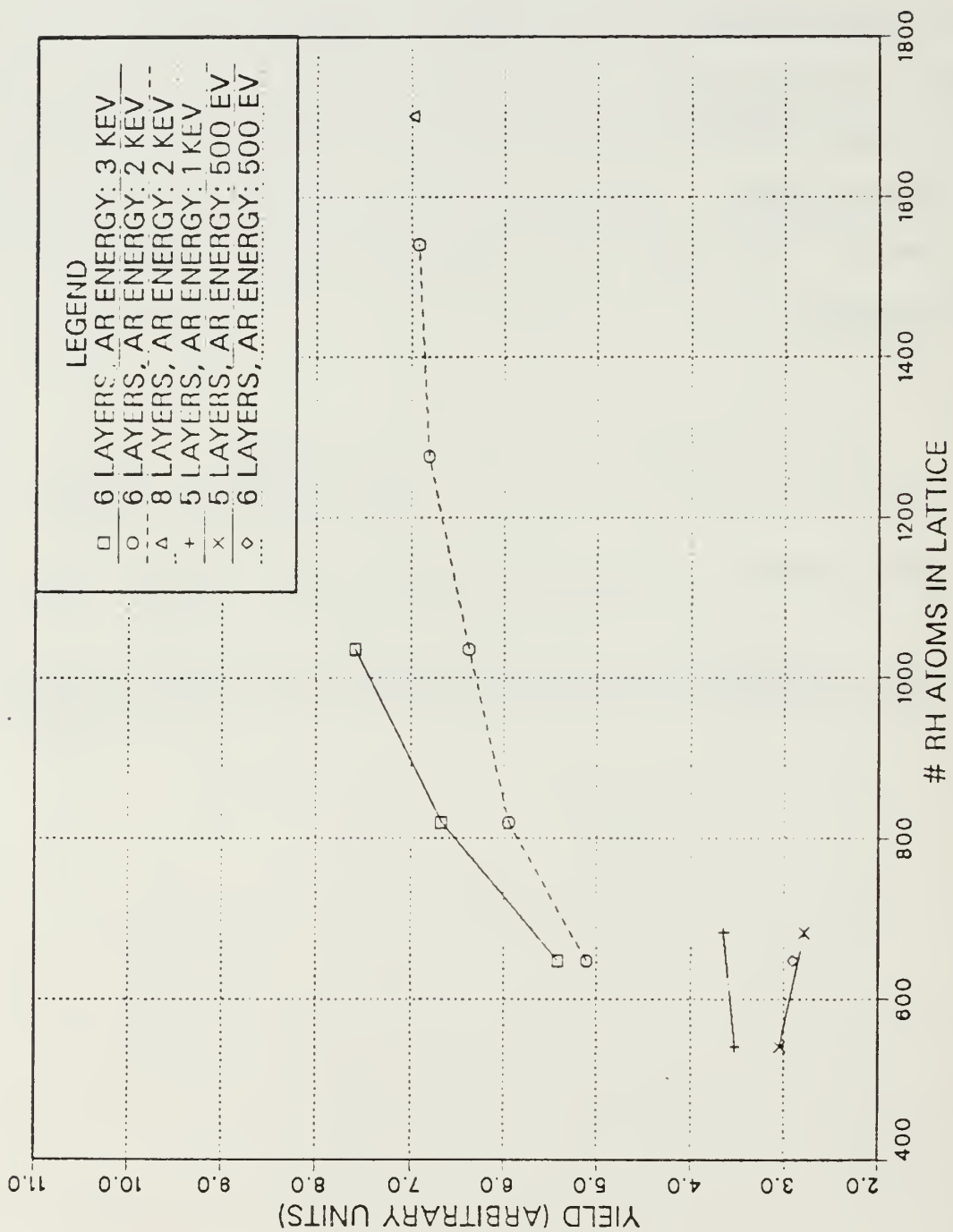


Fig. 1 Yield versus Lattice Size.

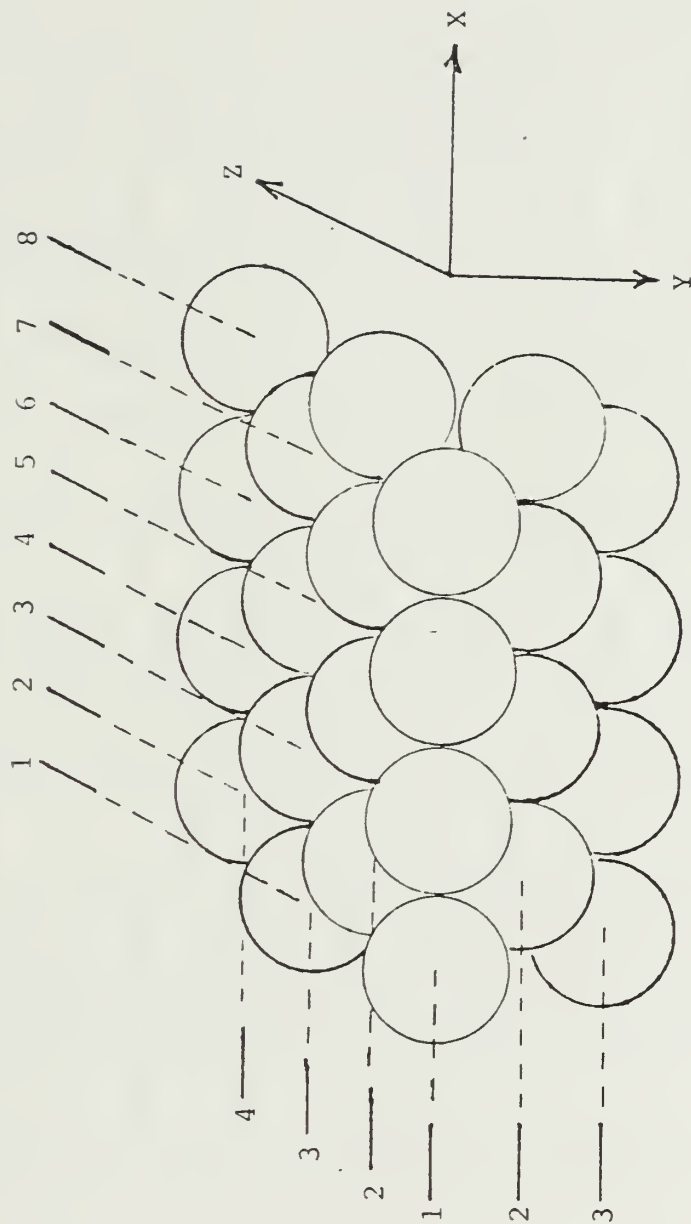


Fig. 2 Lattice Plane Numbering System.

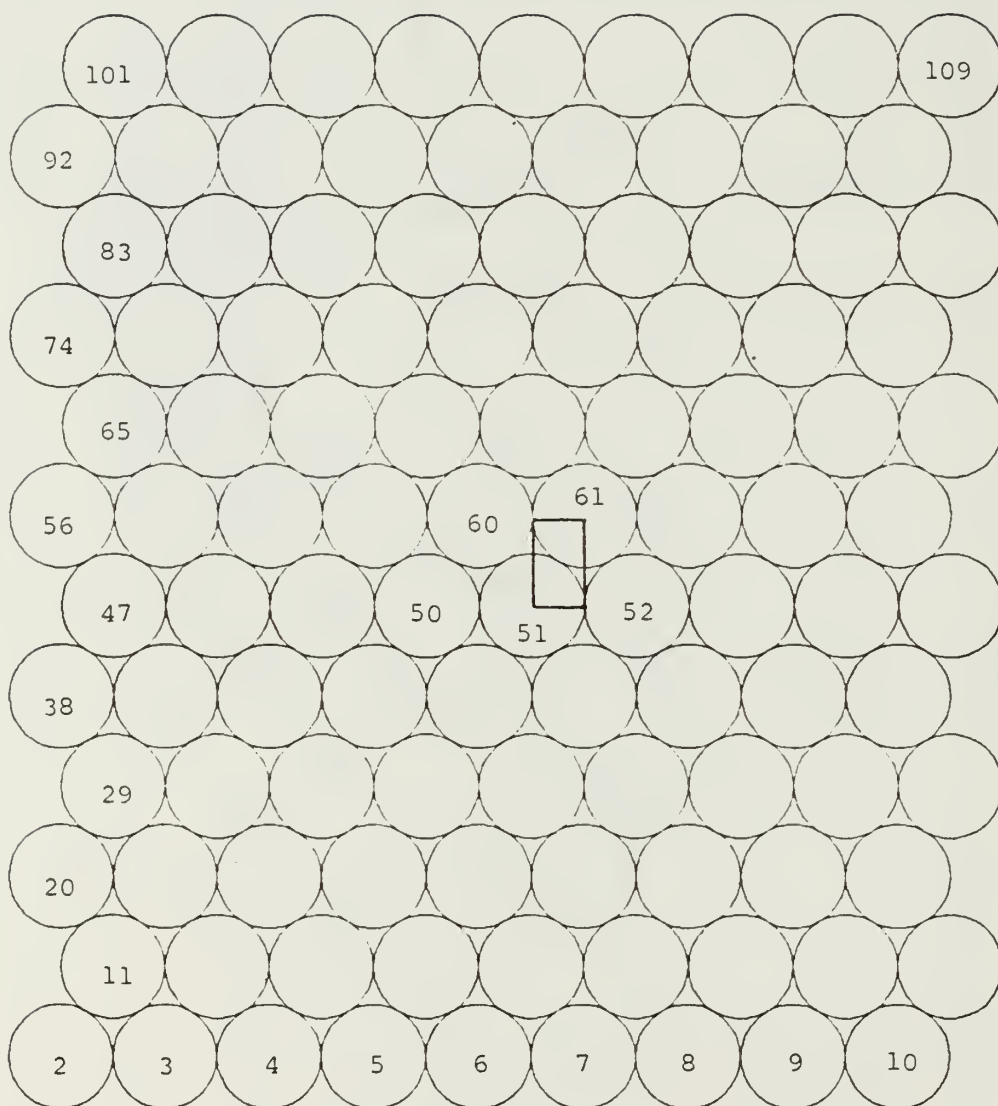


Fig. 3 18x5x12 Lattice Numbering System.

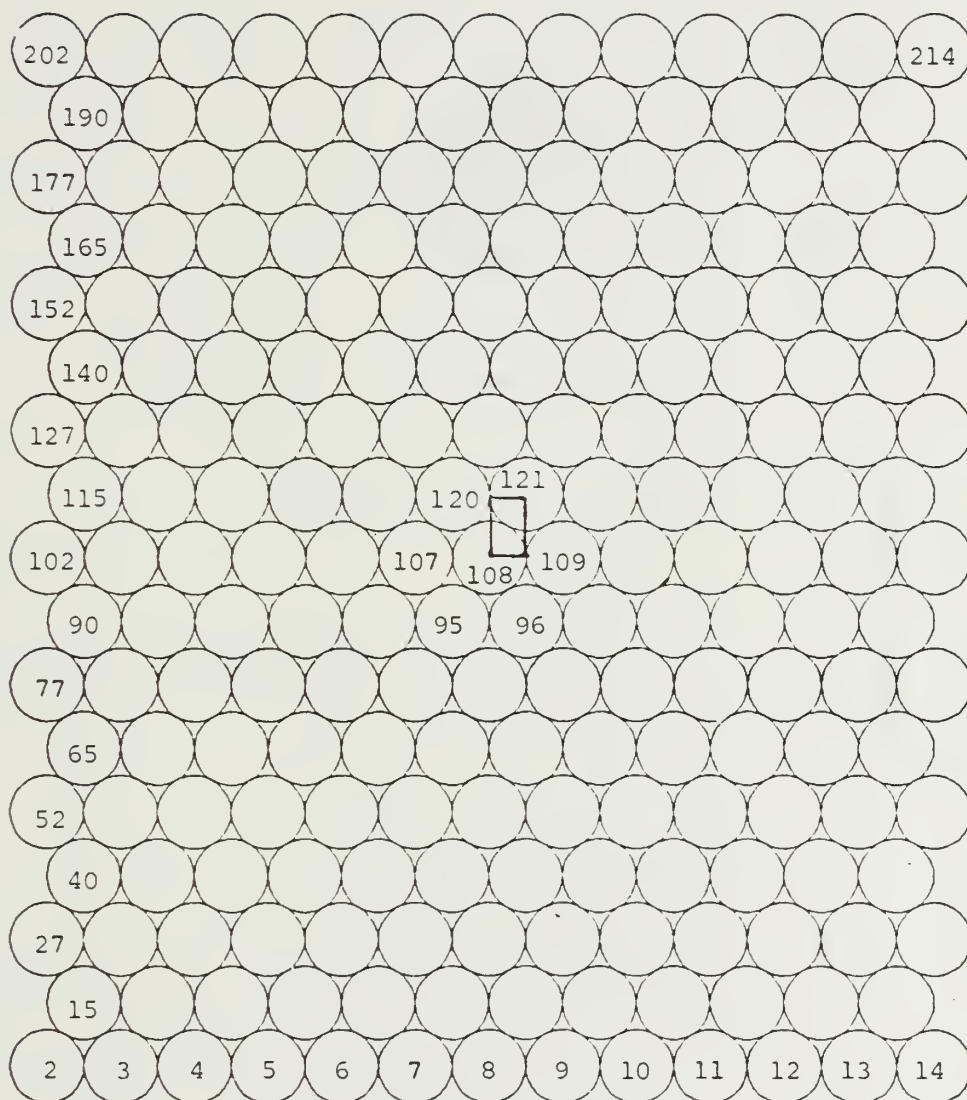


Fig. 4 21x6x17 Lattice Numbering System.

IMPACT POINTS

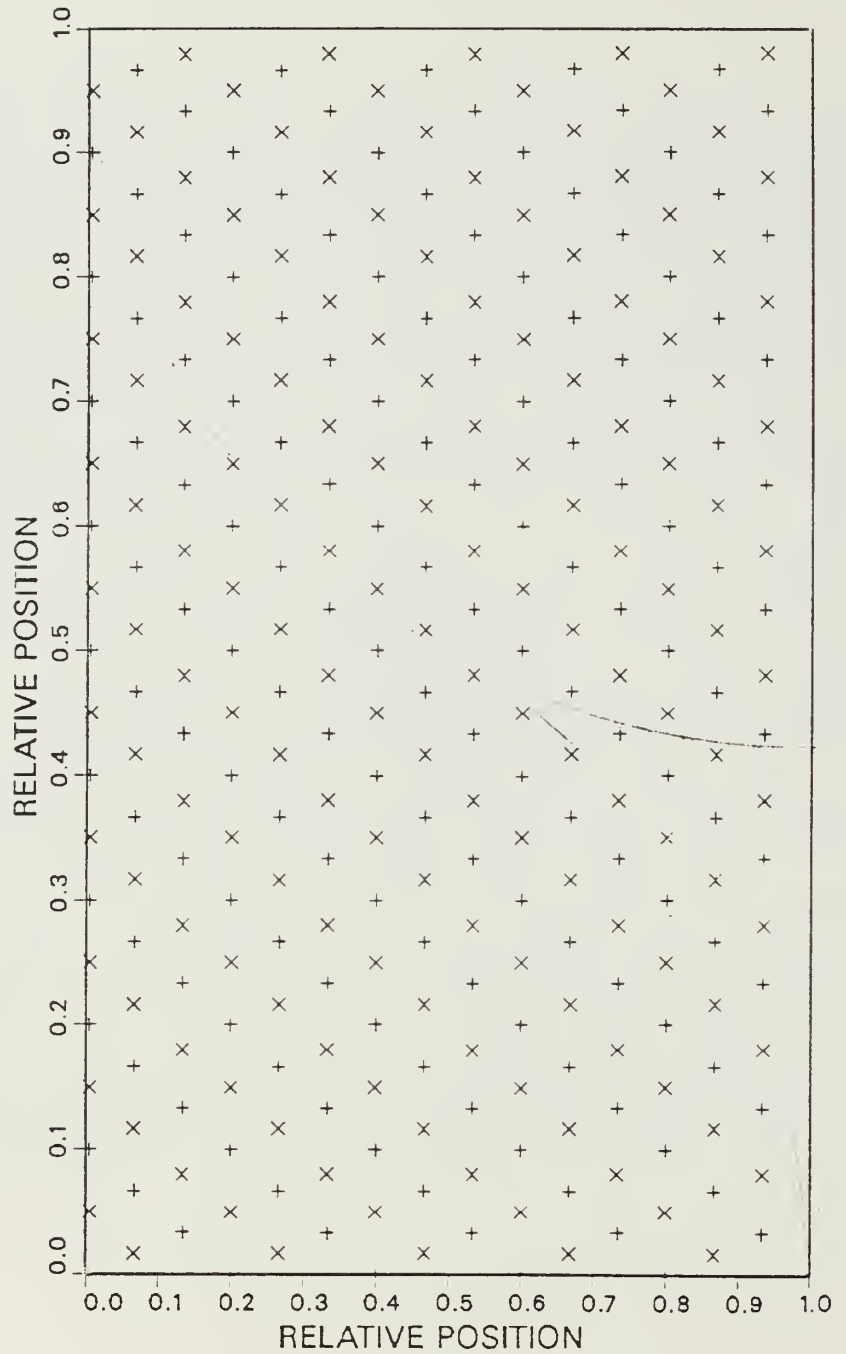
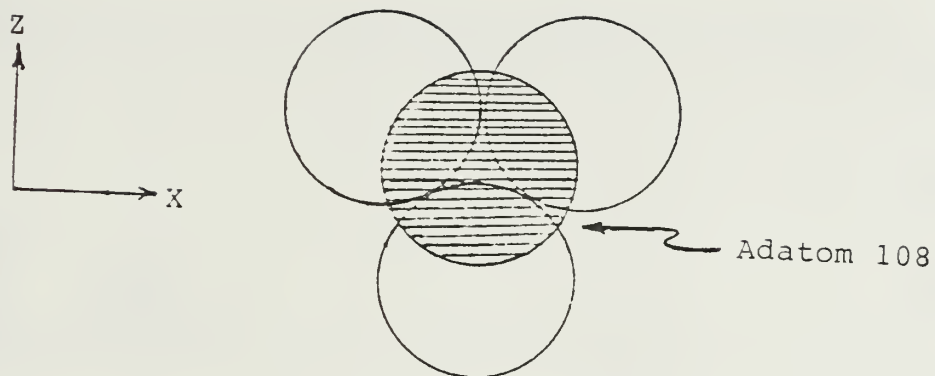
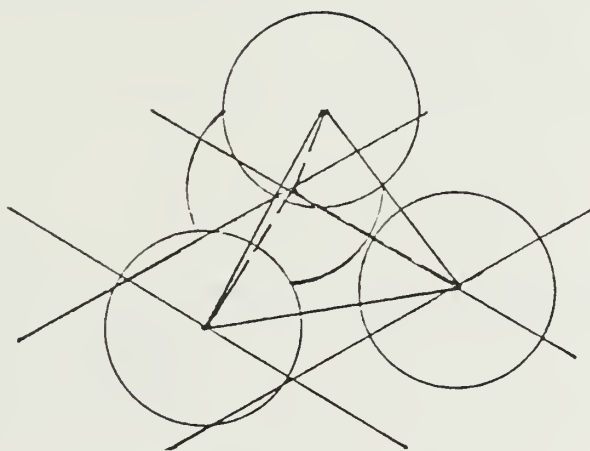


Fig. 5 Impact Point Positions within the Representative Area.



Adatom Numbering System



3-Fold Bridge Position

Fig. 6 Adatom Position.

RHODIUM-RHODIUM POTENTIALS

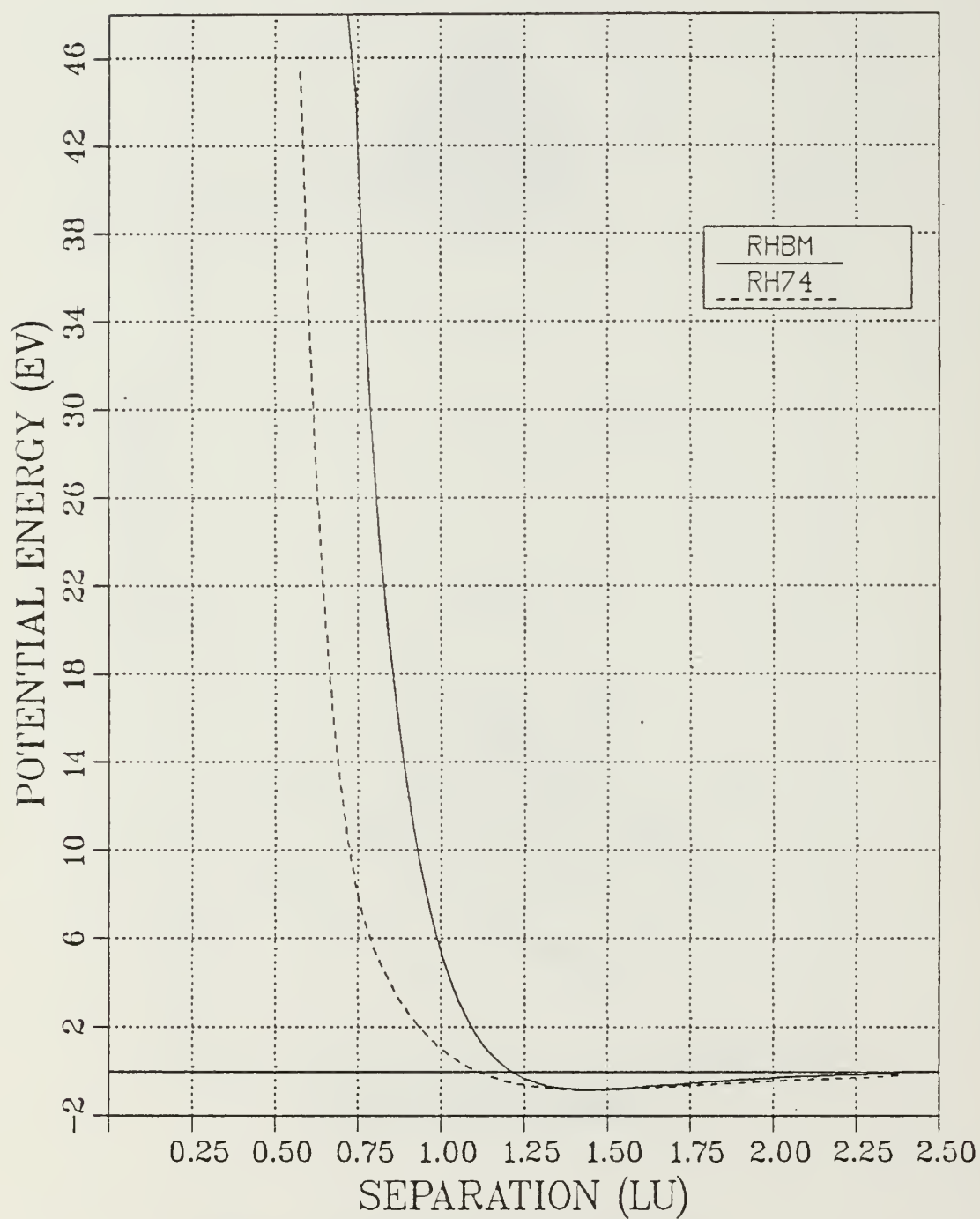


Fig. 7 Rhodium-Rhodium Potential Function.

RHODIUM-RHODIUM FORCES

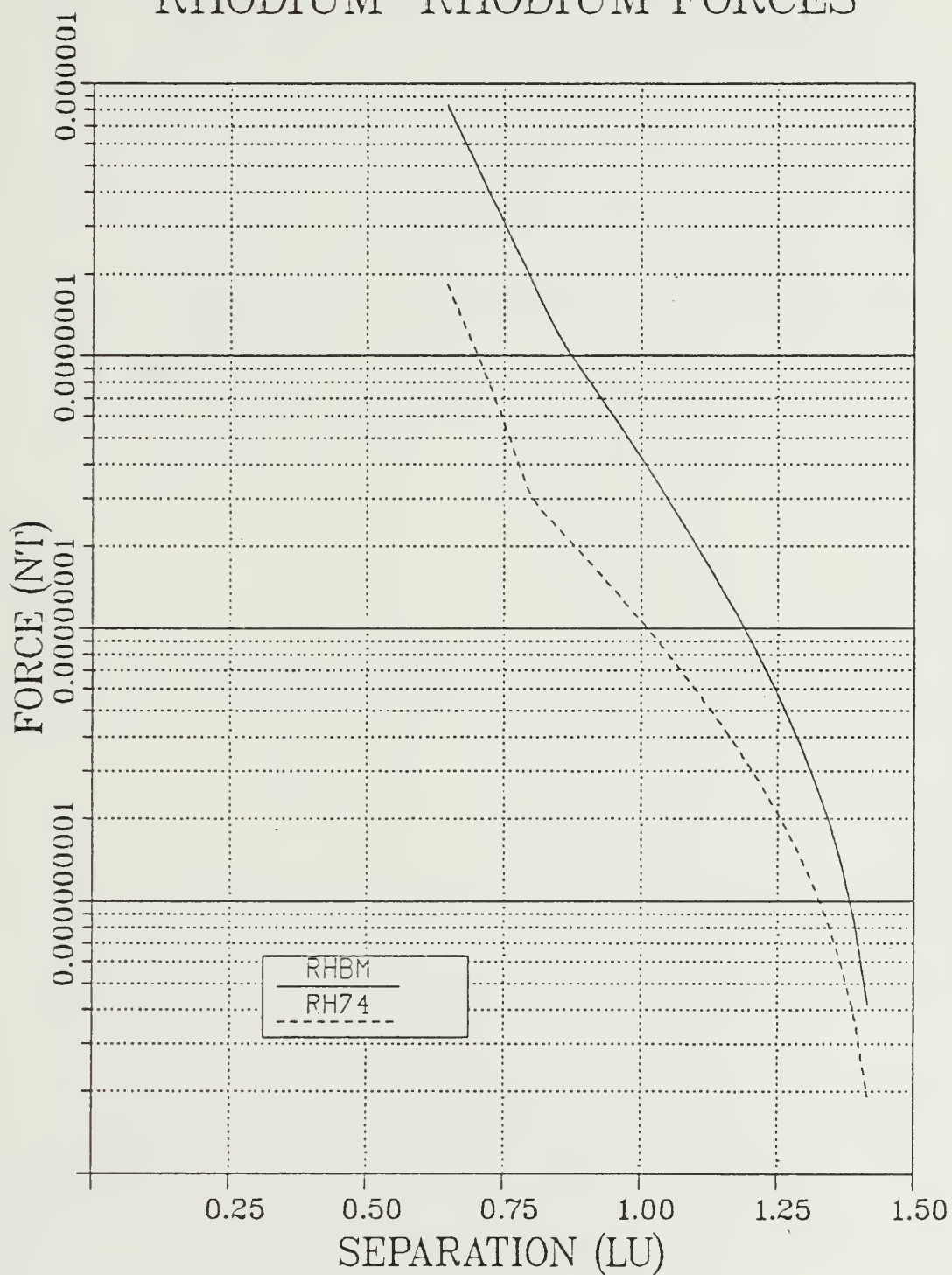


Fig. 8 Rhodium-Rhodium Forces.

RHODIUM-RHODIUM POTENTIALS

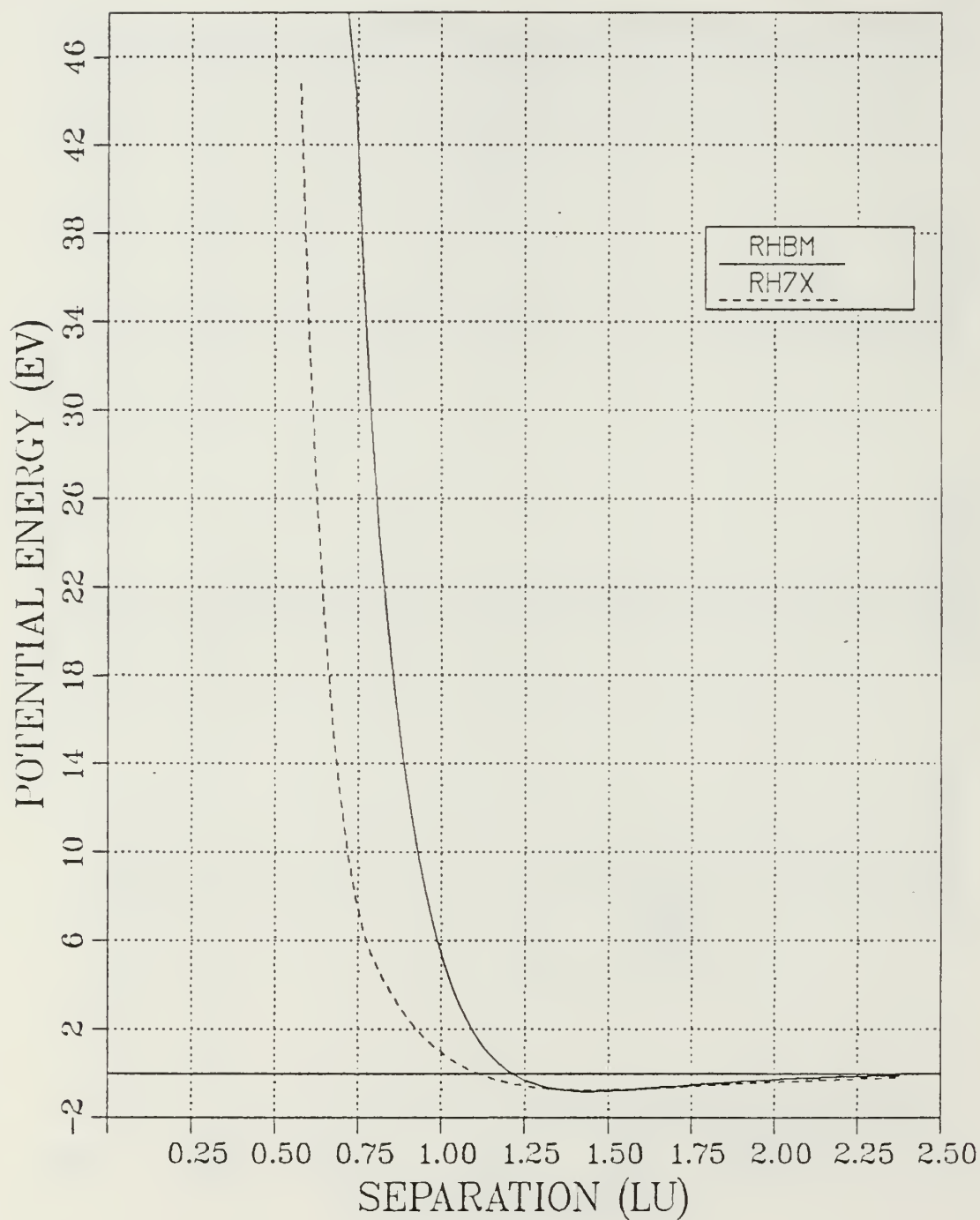


Fig. 9 Rhodium-Rhodium Potential Function.

RHODIUM-RHODIUM FORCES

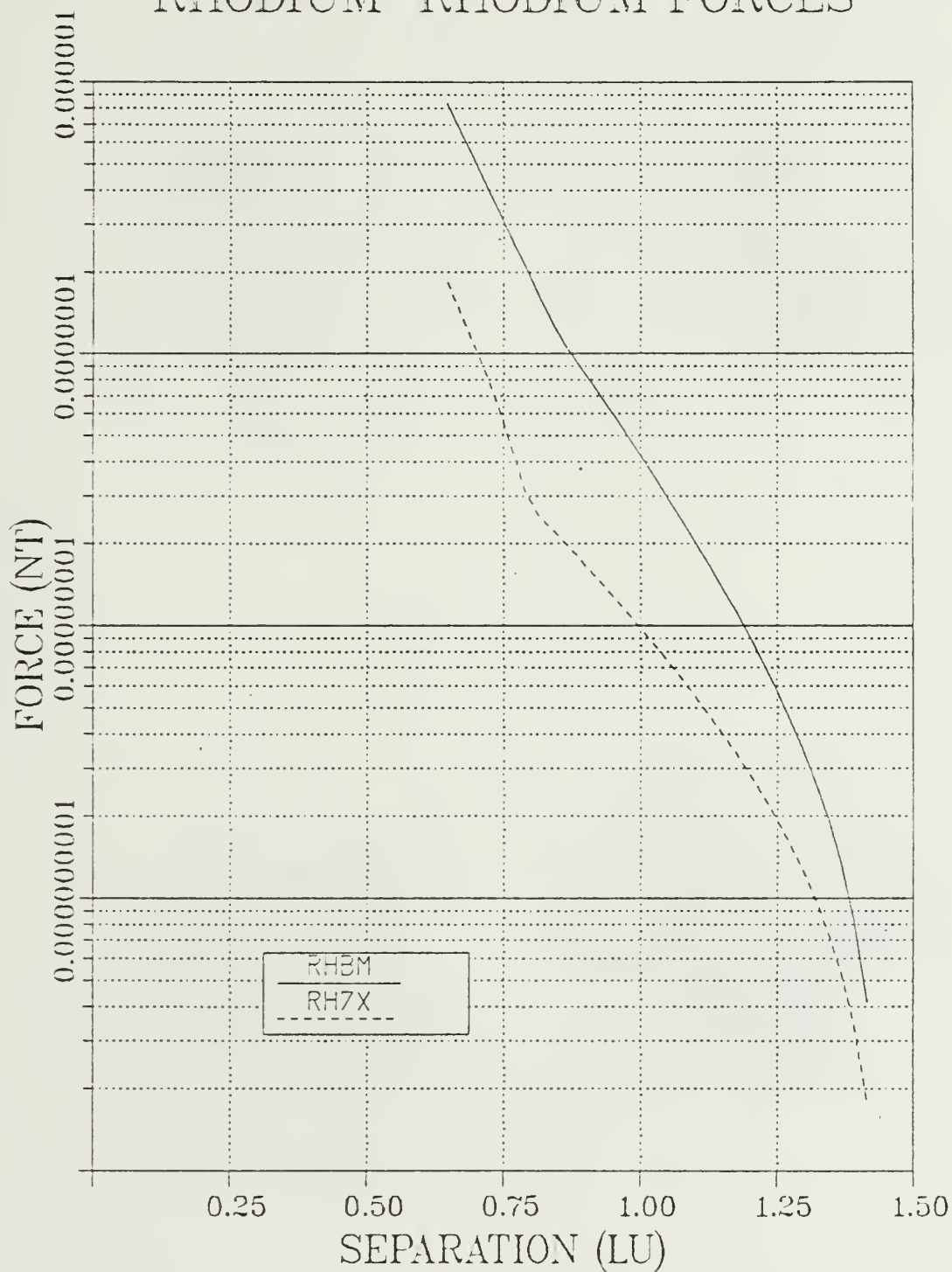
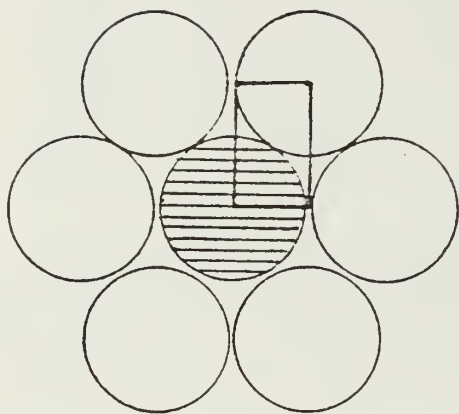
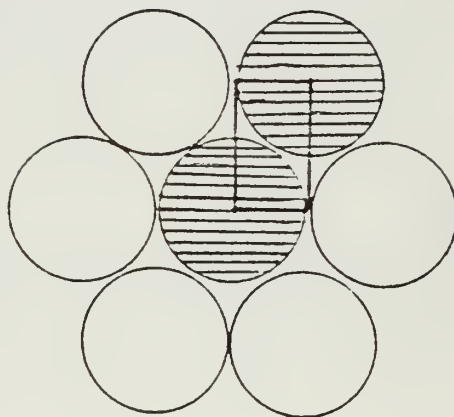


Fig. 10 Rhodium-Rhodium Forces.

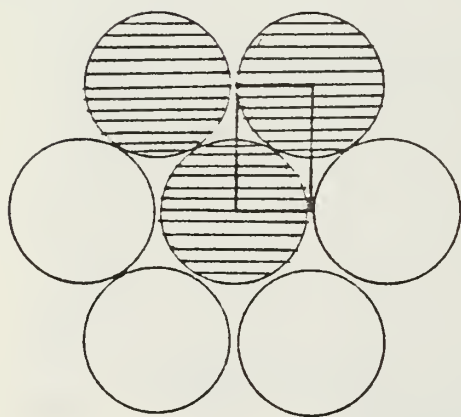
1 Vacancy



2 Vacancies



3 Vacancies



7 Vacancies

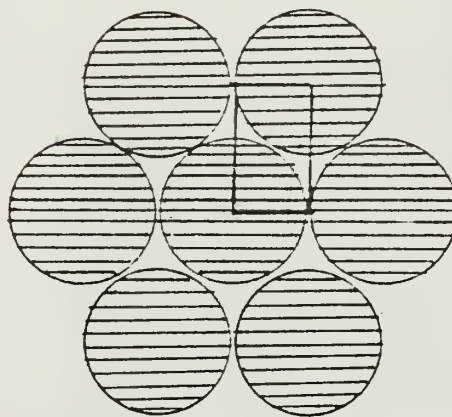
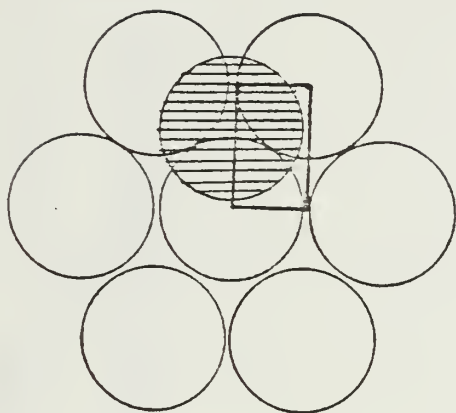
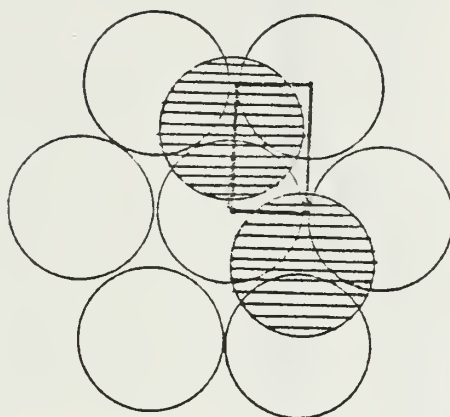


Fig. 11 Relative Vacancy Positions.

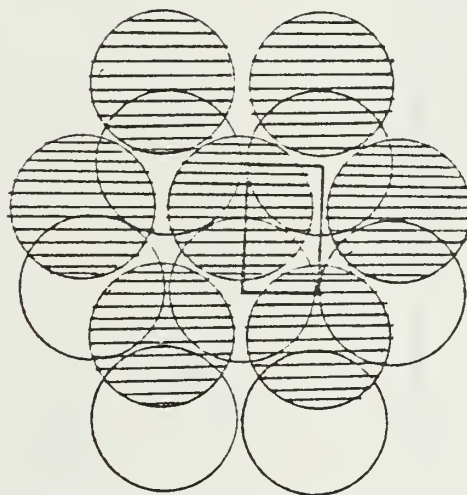
1 Adatom



2 Adatoms



7 Adatoms



3 Adatoms

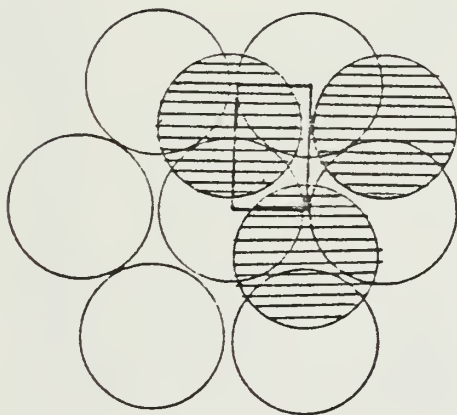


Fig. 12 Relative Adatom Positions.

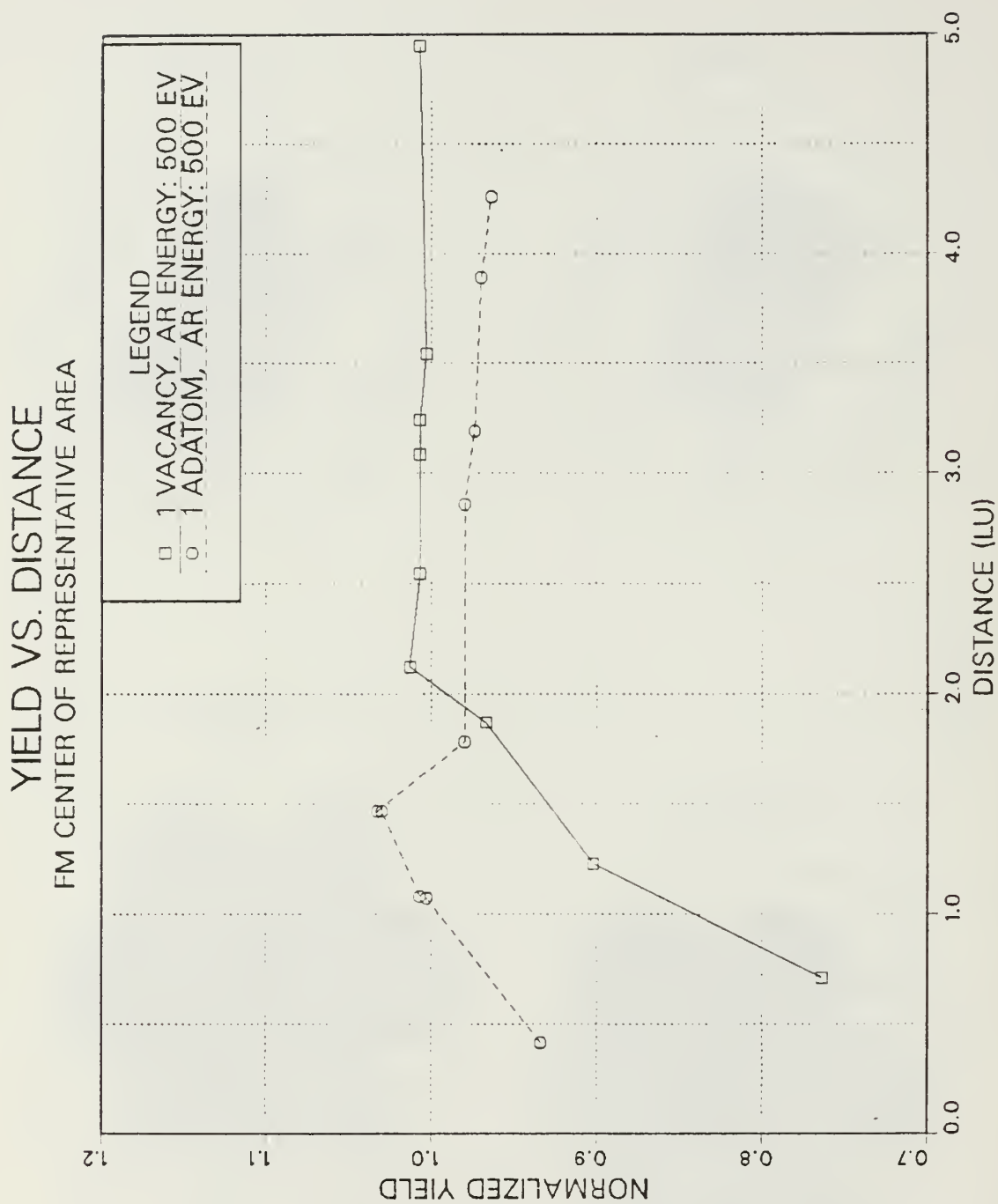


Fig. 13 Yield versus Distance from
Center of Representative Area.

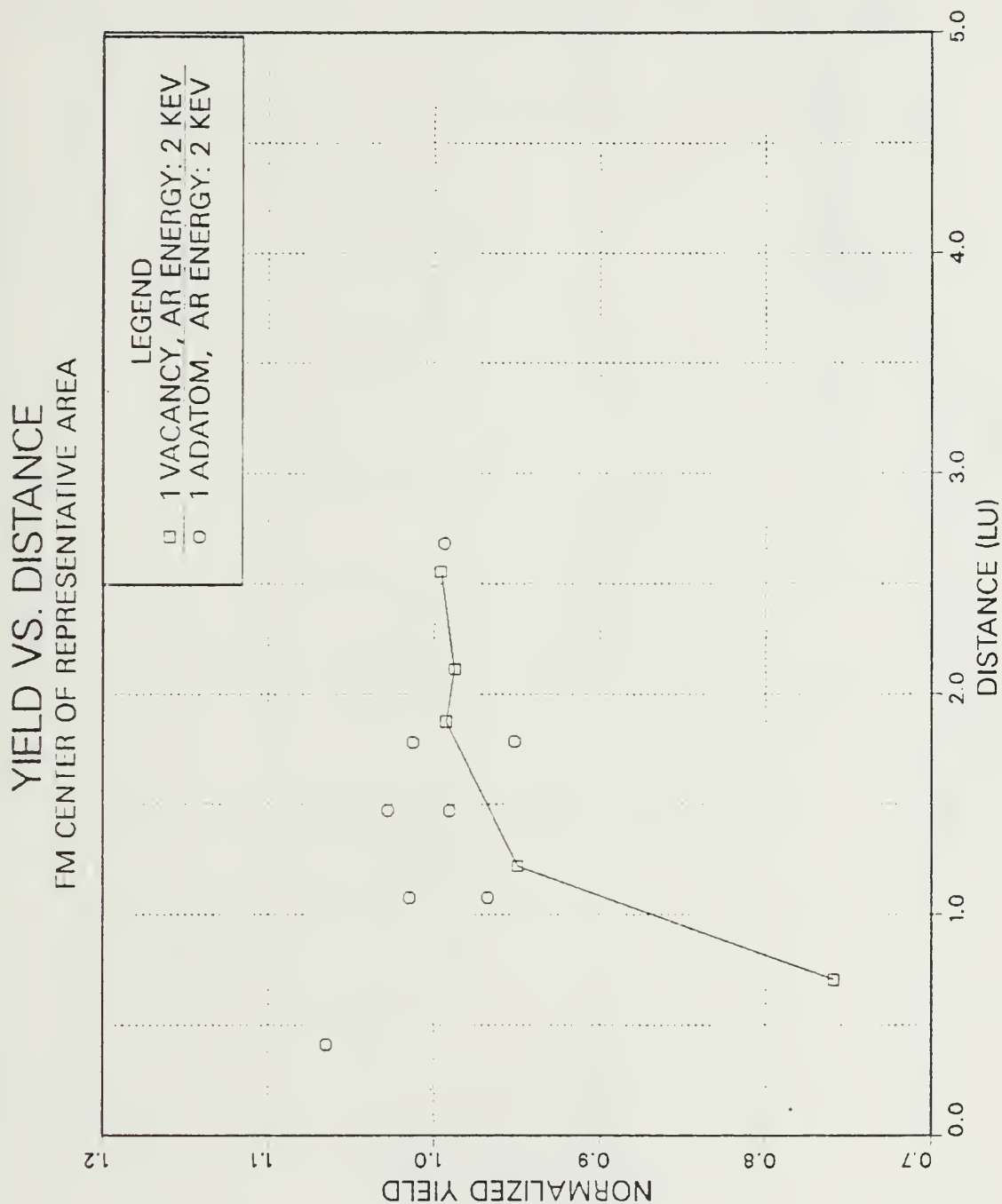


Fig. 14 Yield versus Distance from Center of Representative Area.

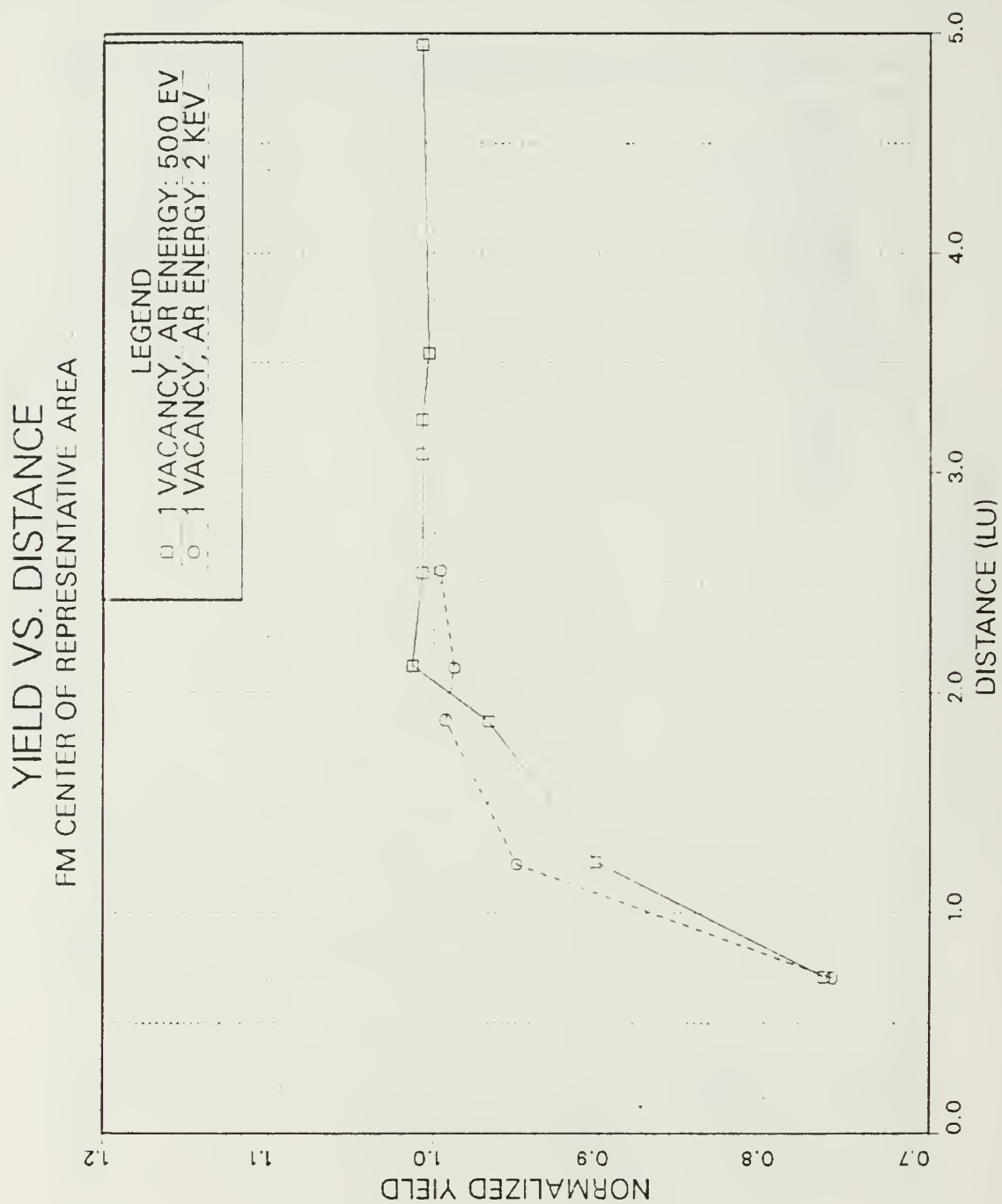


Fig. 15 Yield versus Distance from
Center of Representative Area.

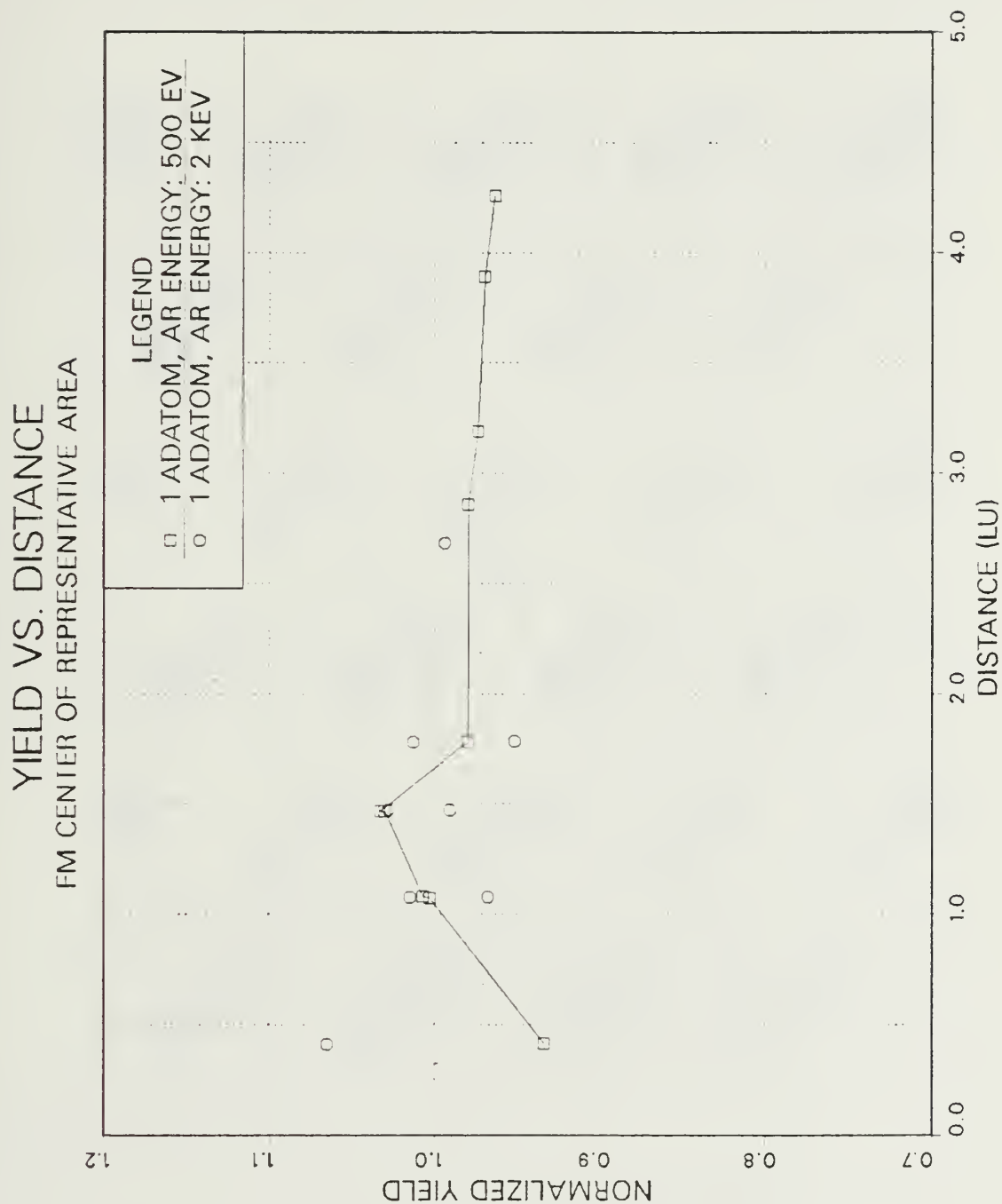


Fig. 16 Yield versus Distance from
Center of Representative Area.

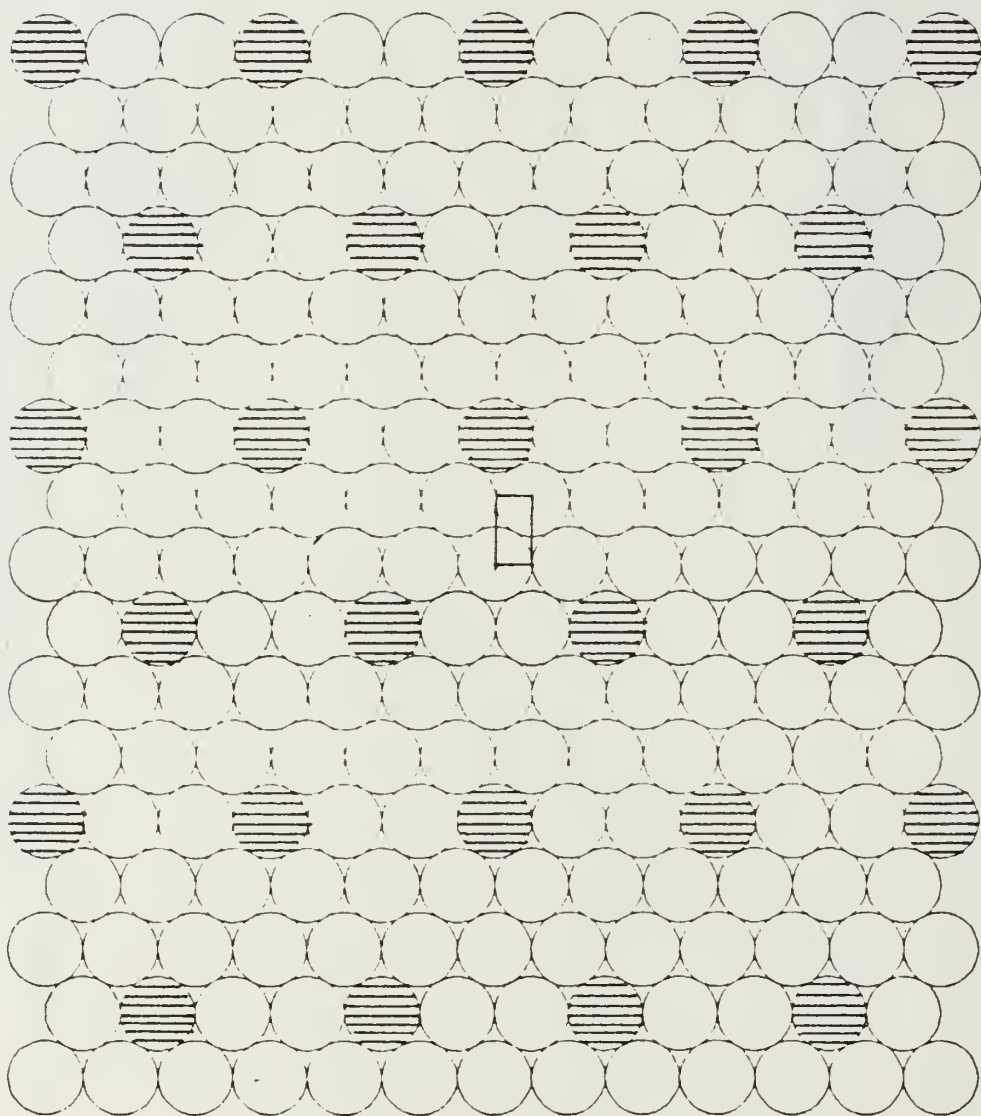


Fig. 17 Distributed Vacancy Positions.

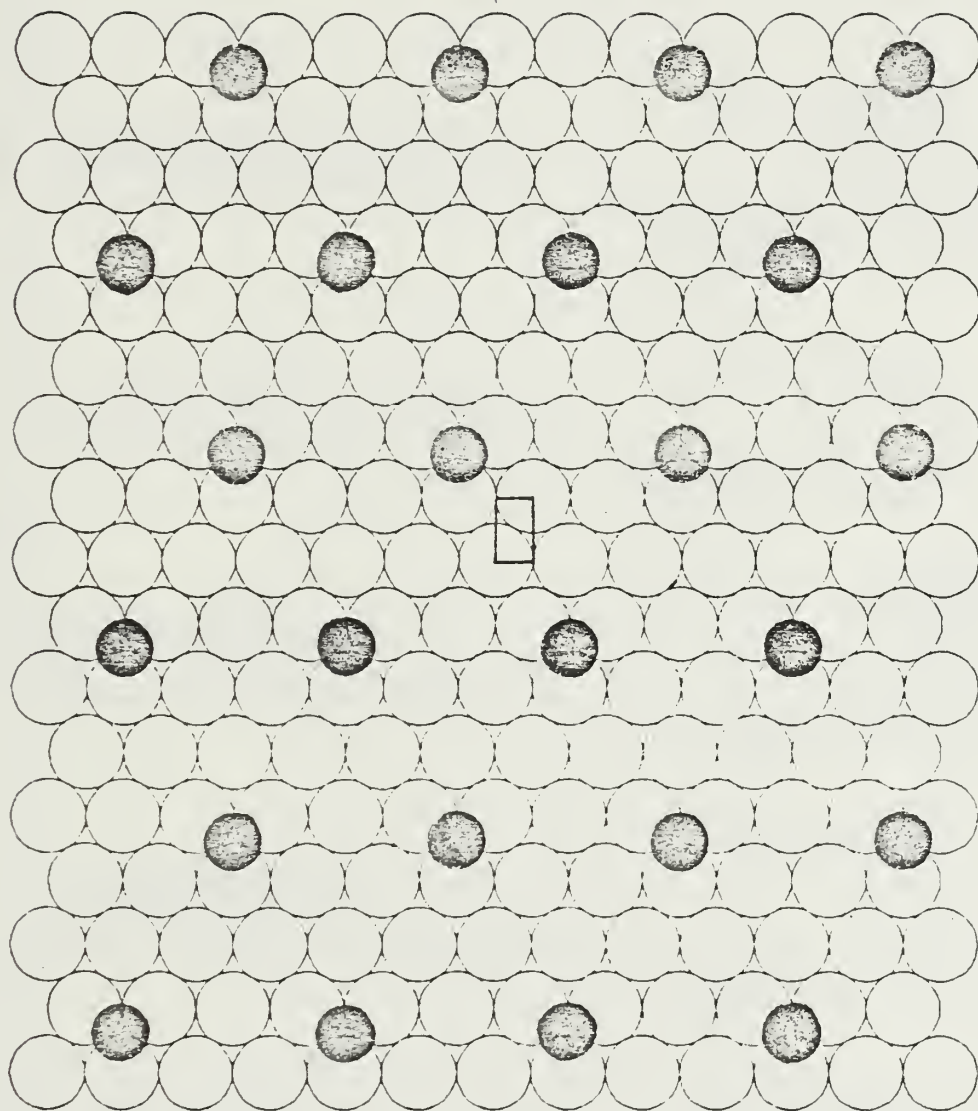


Fig. 18 Distributed Adatom Positions.

ATOMS PER SINGLE ION, AR ENERGY: 500EV

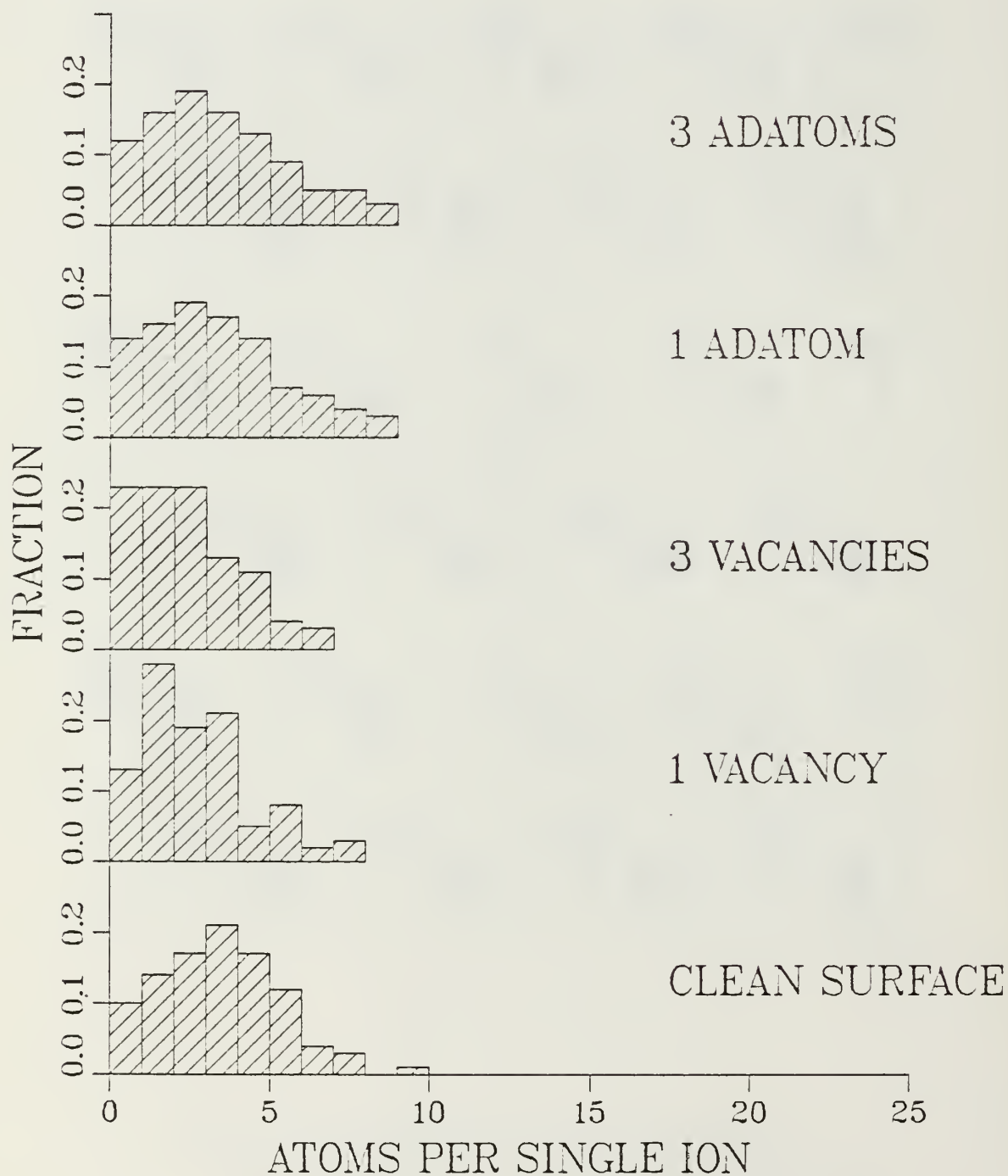


Fig. 19 Atoms per Single Ion Distribution.

ATOMS PER SINGLE ION, AR ENERGY: 2KEV

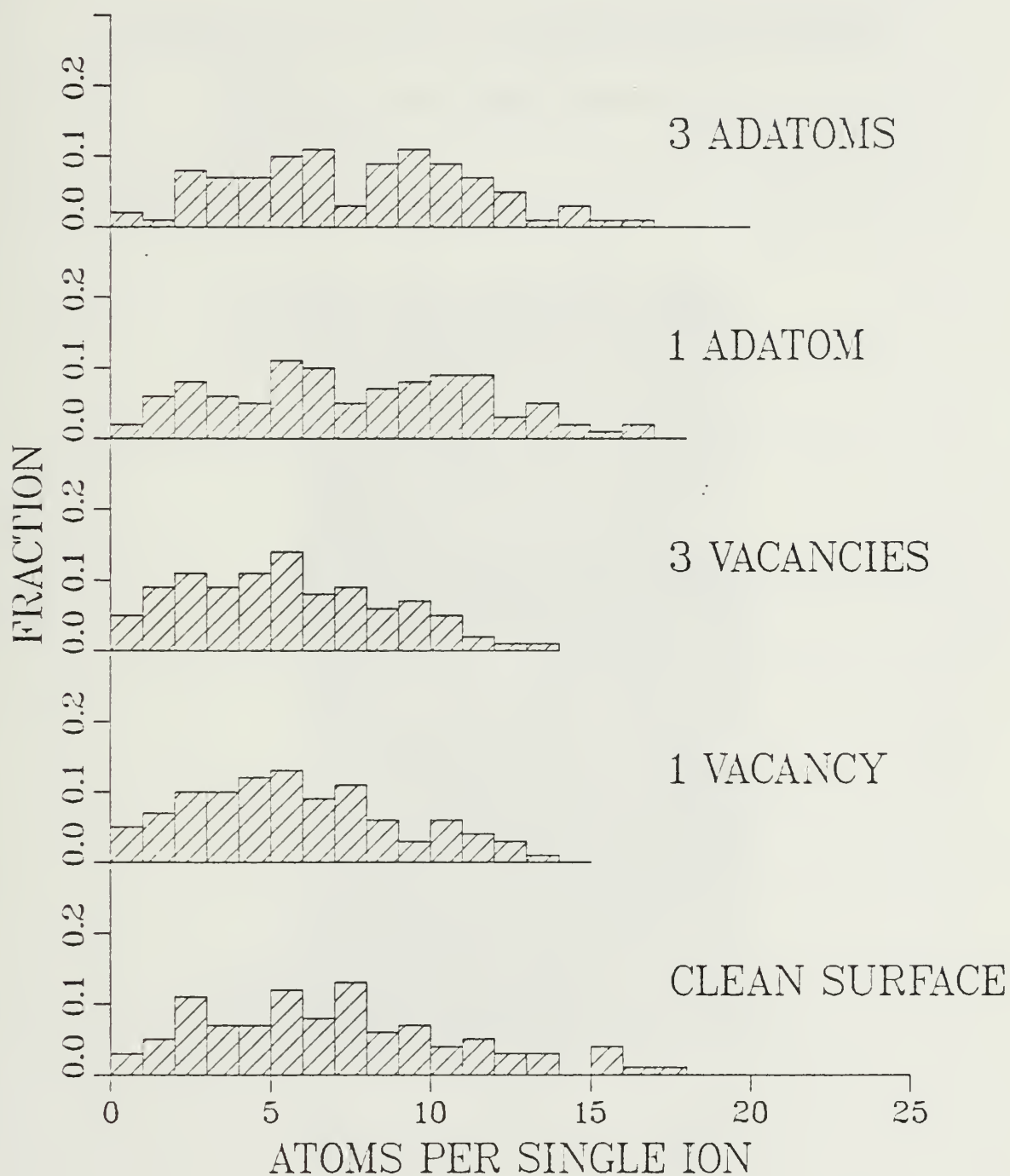


Fig. 20 Atoms per Single Ion Distribution.

500EV RH(111)/AR<111> CLEAN SURFACE

ATOM YIELD PER IMPACT POINT

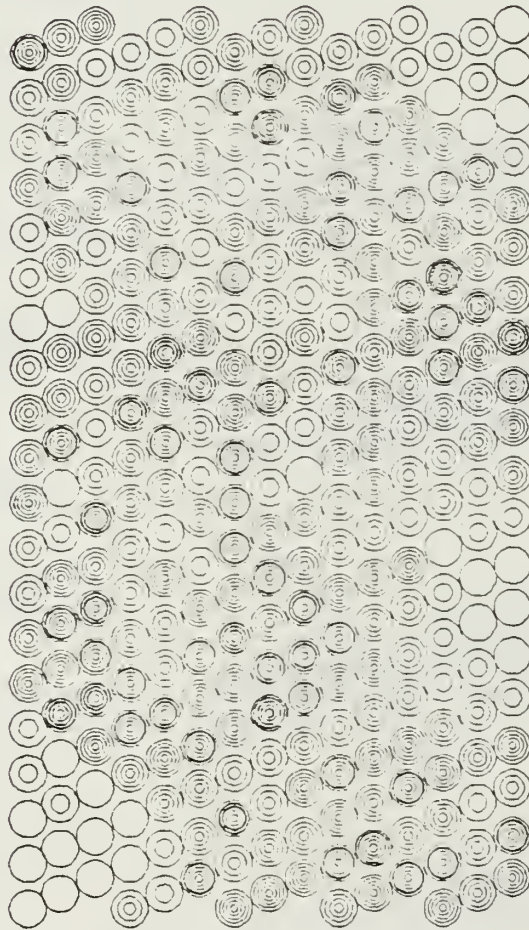


Fig. 21 Atom Yield per Impact Point.

TIME DISTRIBUTION, AR ENERGY: 500EV

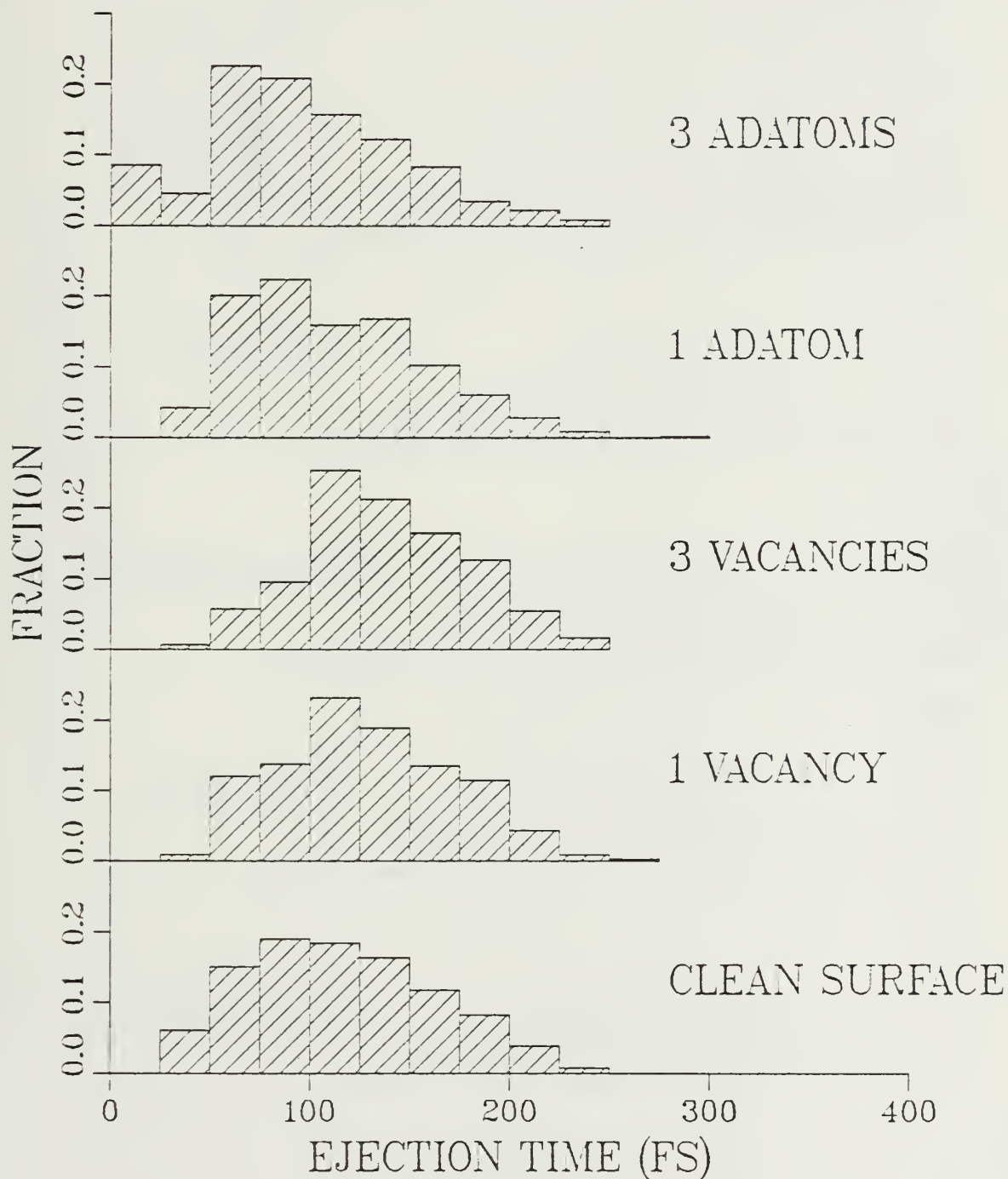


Fig. 22 Atom Ejection Time Distribution.

TIME DISTRIBUTION, AR ENERGY: 2KEV

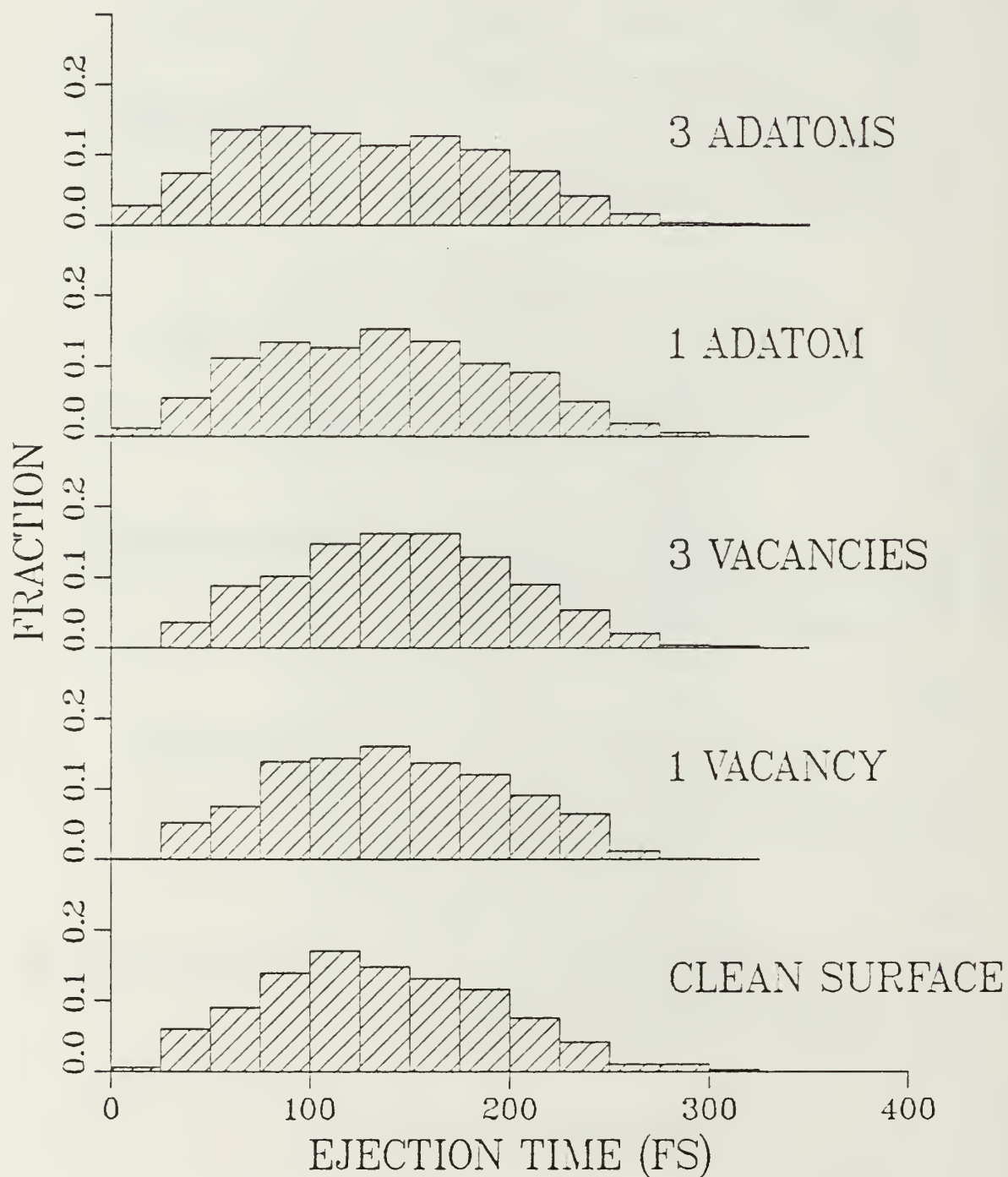


Fig. 23 Atom Ejection Time Distribution.

YIELD RATIO VS. SIZE OF DEFECT

AR ENERGY: 500 EV

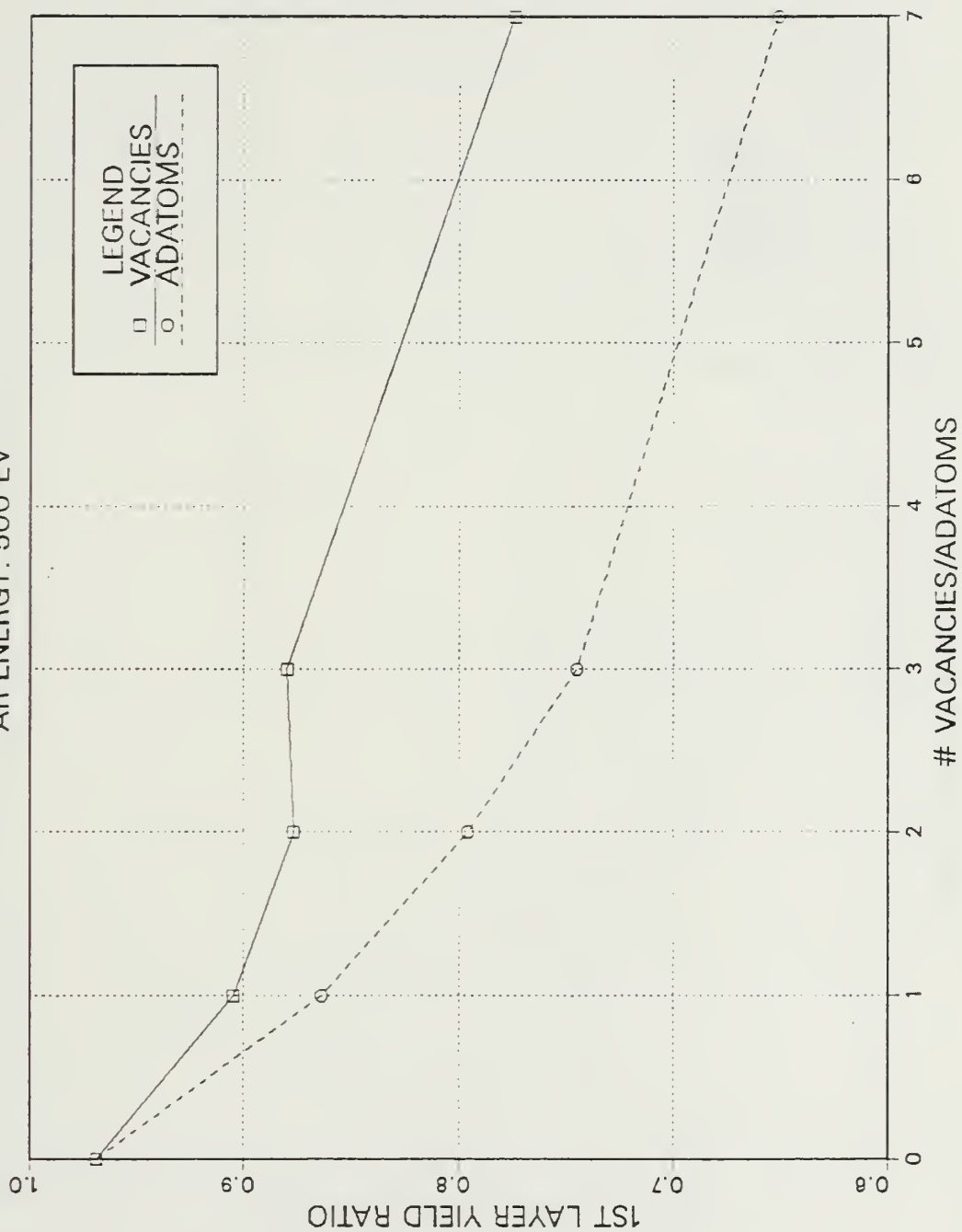


Fig. 24 Yield Ratio versus Size of Defect.

YIELD RATIO VS. SIZE OF DEFECT

AR ENERGY: 2 KEV

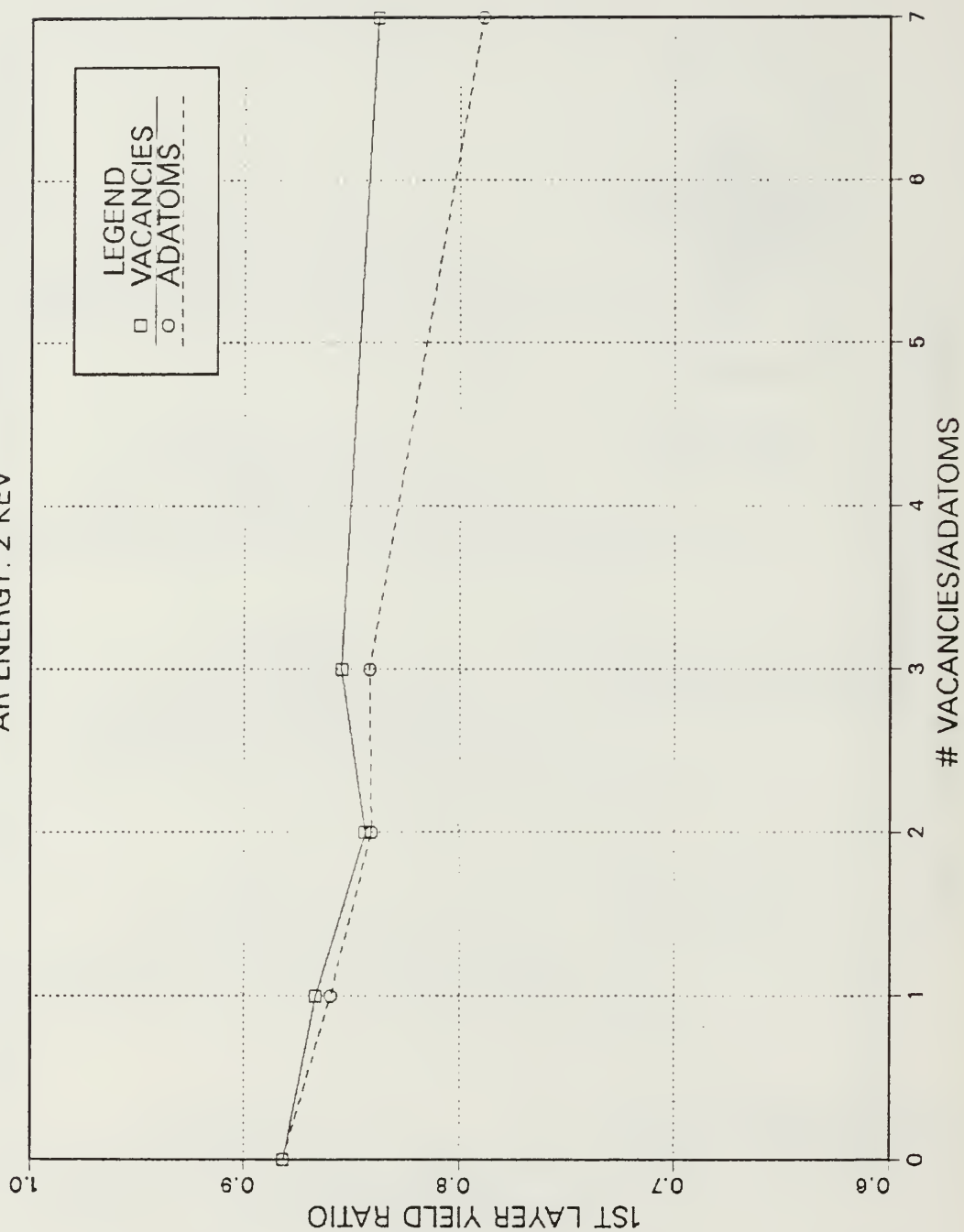


Fig. 25 Yield Ratio versus Size of Defect.

ENERGY DISTRIBUTION: RH

AR ENERGY: 2 KEV

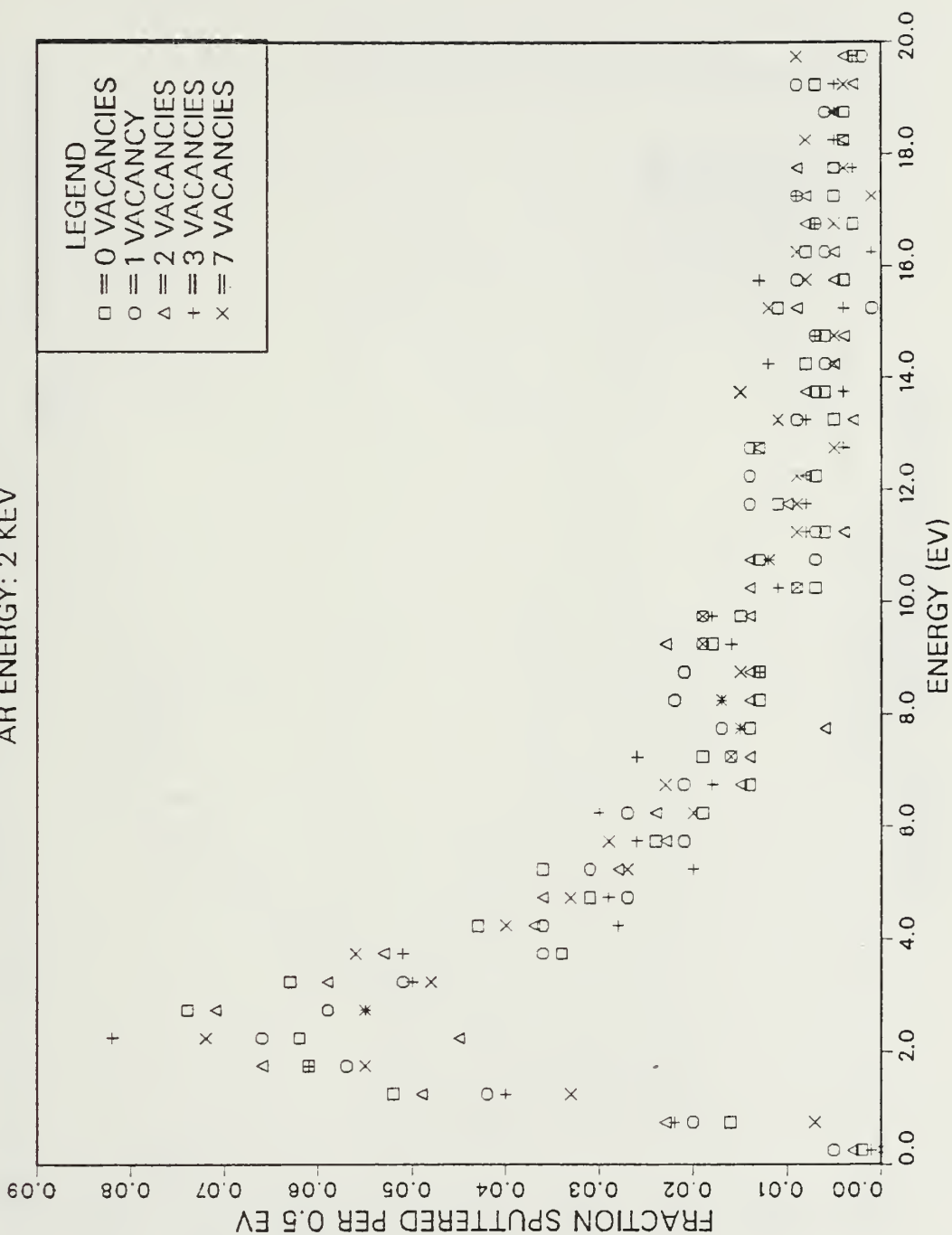


Fig. 26 Ejected Atom Energy Distribution.

ENERGY DISTRIBUTION: RH

AR ENERGY: 2 KEV



Fig. 27 Ejected Atom Energy Distribution.

ENERGY DISTRIBUTION: RH

AR ENERGY: 500 EV

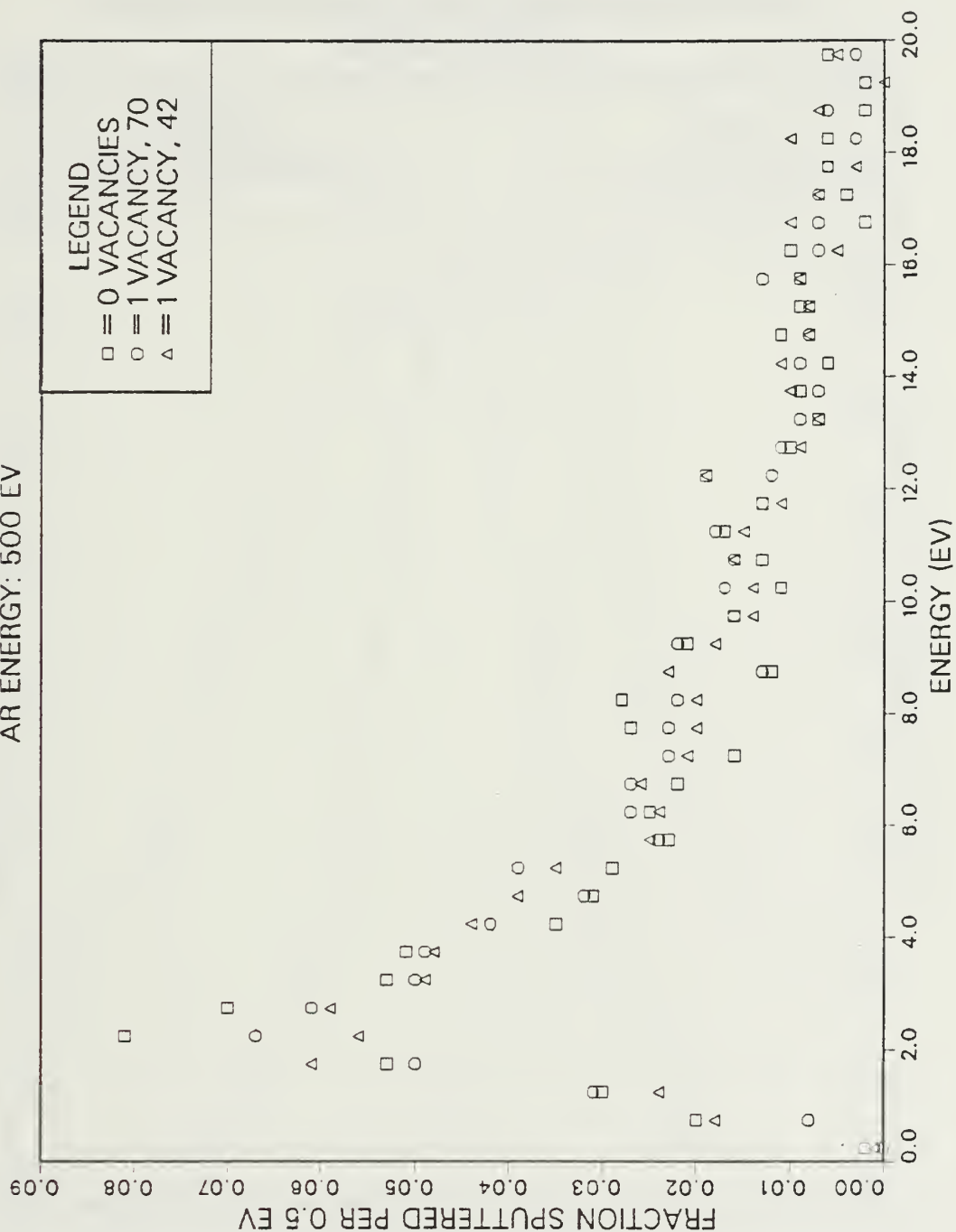


Fig. 28 Ejected Atom Energy Distribution.

ANGULAR TALLY: RH ENERGY > 5 EV

BARE SURFACE

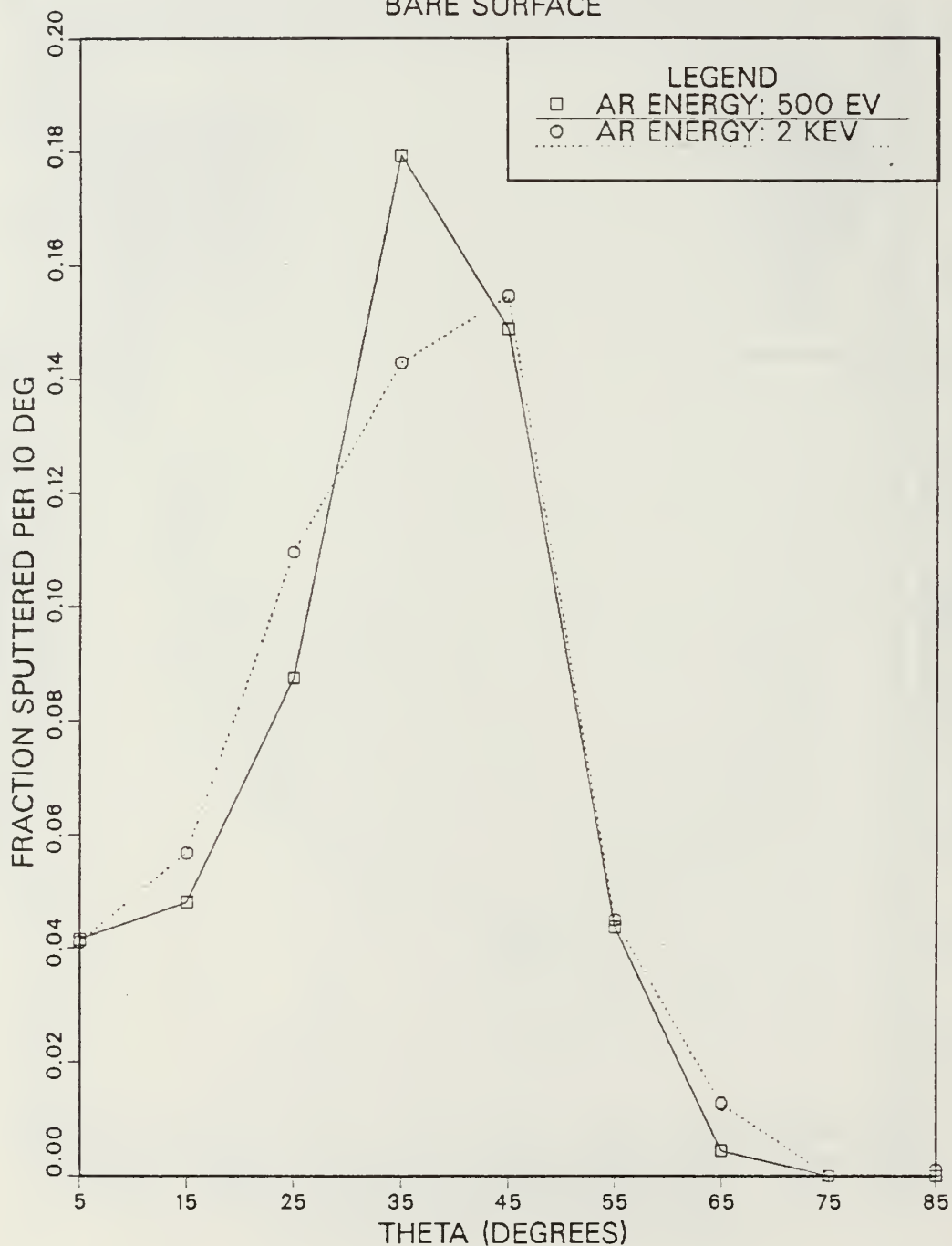


Fig. 29 Ejected Atom Angular Distribution.

ANGULAR TALLY: RH ENERGY > 5 EV

AR ENERGY: 2 KEV

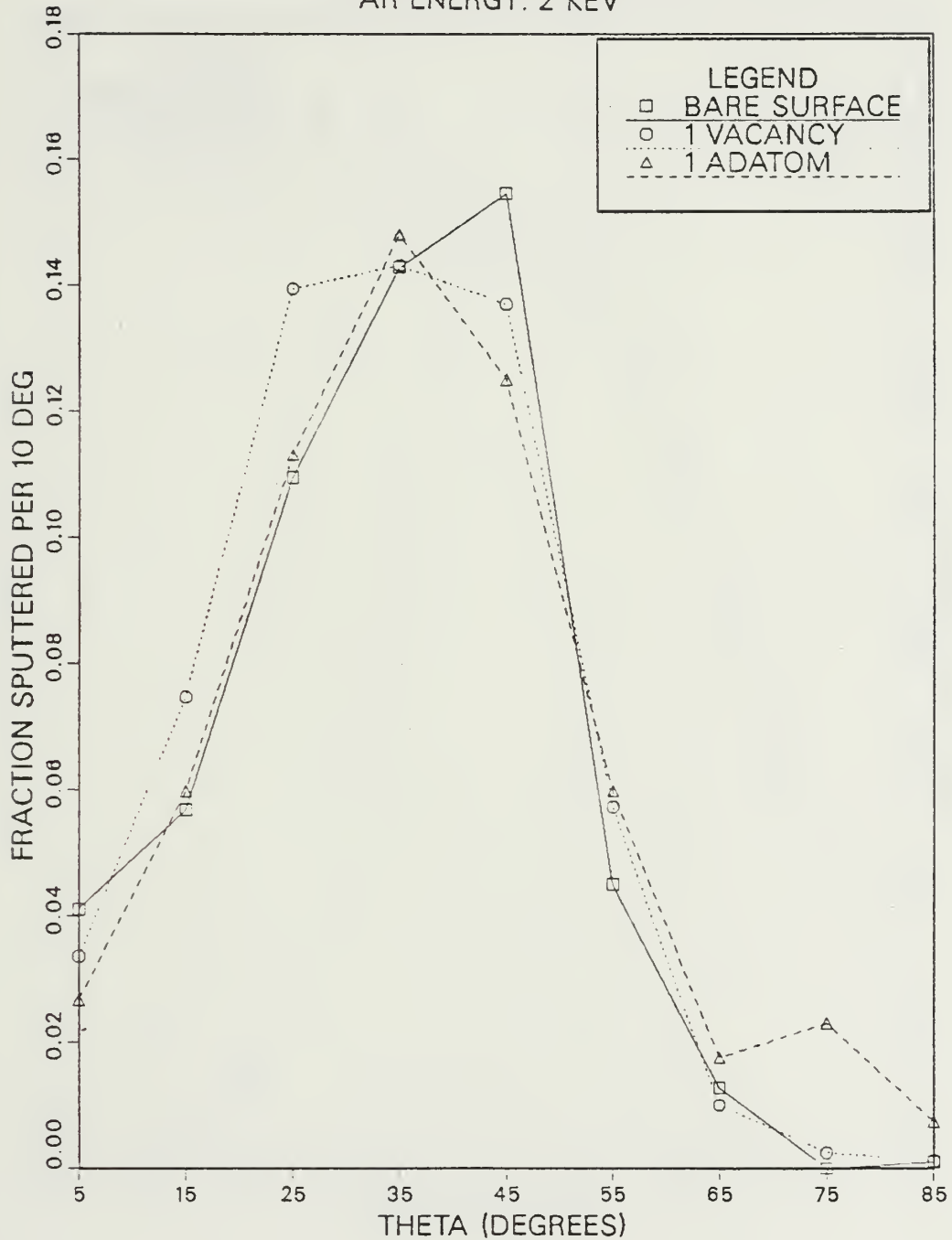


Fig. 30 Ejected Atom Angular Distribution.

ANGULAR TALLY: RH ENERGY > 5 EV

AR ENERGY: 2 KEV

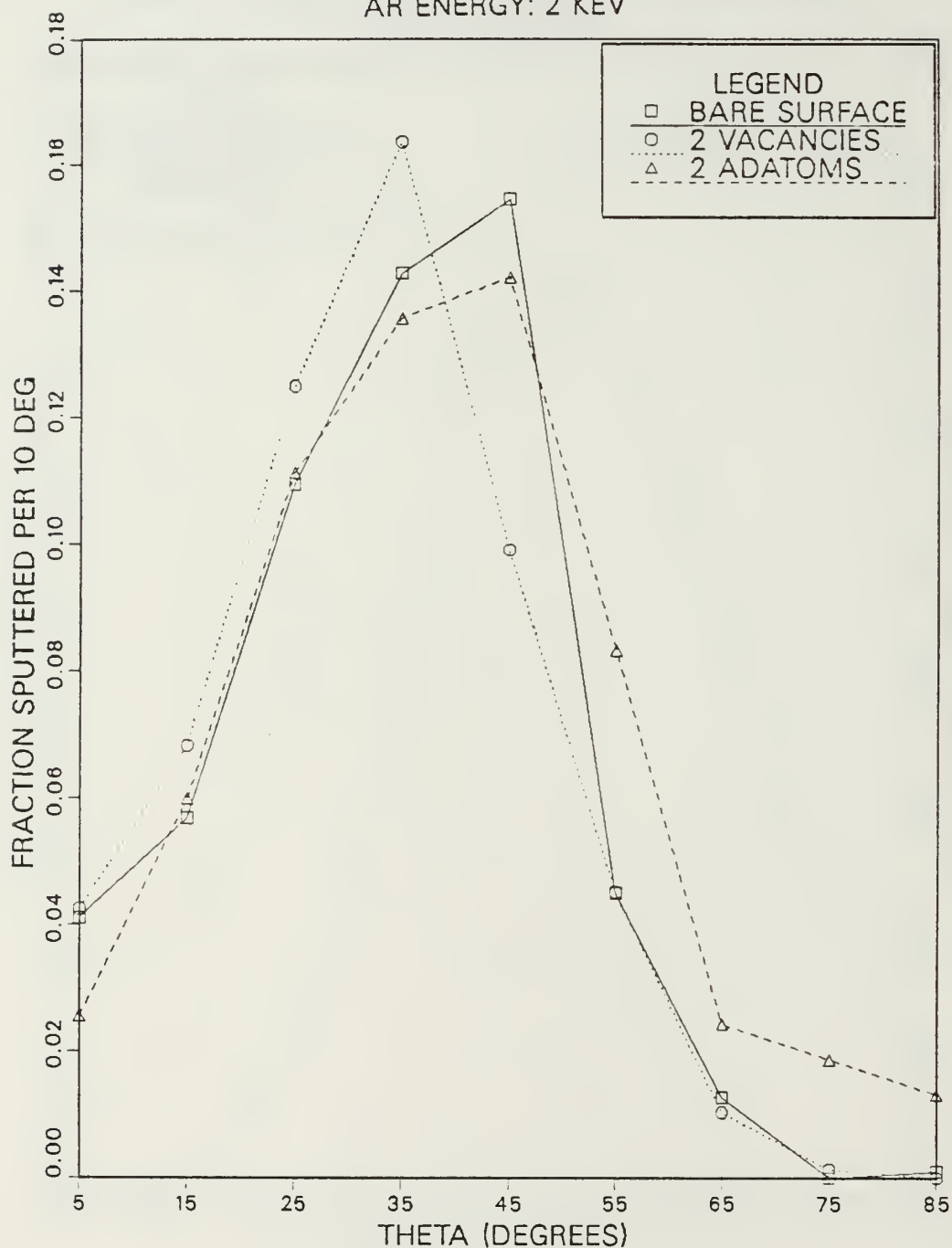


Fig. 31 Ejected Atom Angular Distribution.

ANGULAR TALLY: RH ENERGY > 5 EV

AR ENERGY: 2 KEV

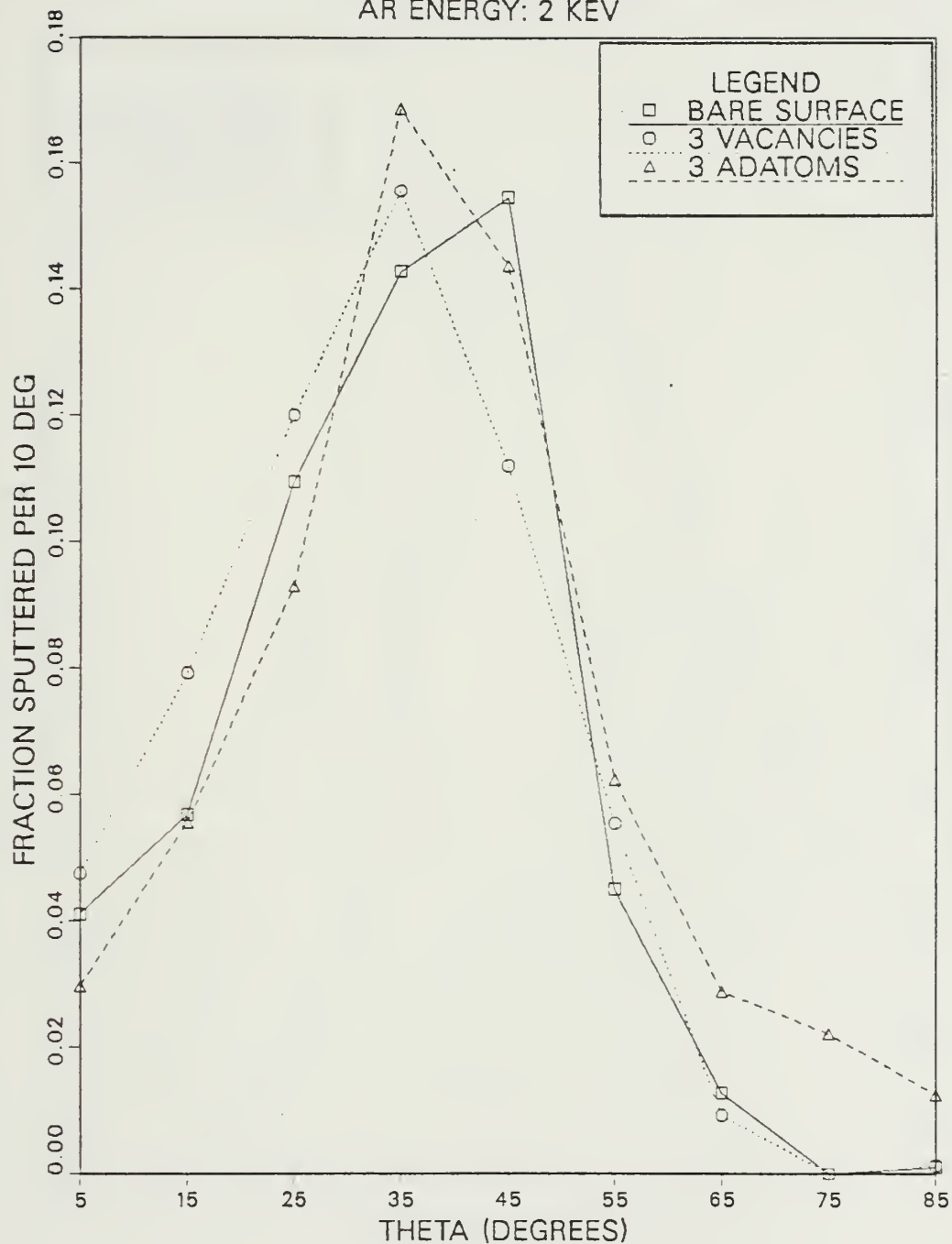


Fig. 32 Ejected Atom Angular Distribution.

ANGULAR TALLY: RH ENERGY > 5 EV

AR ENERGY: 2 KEV

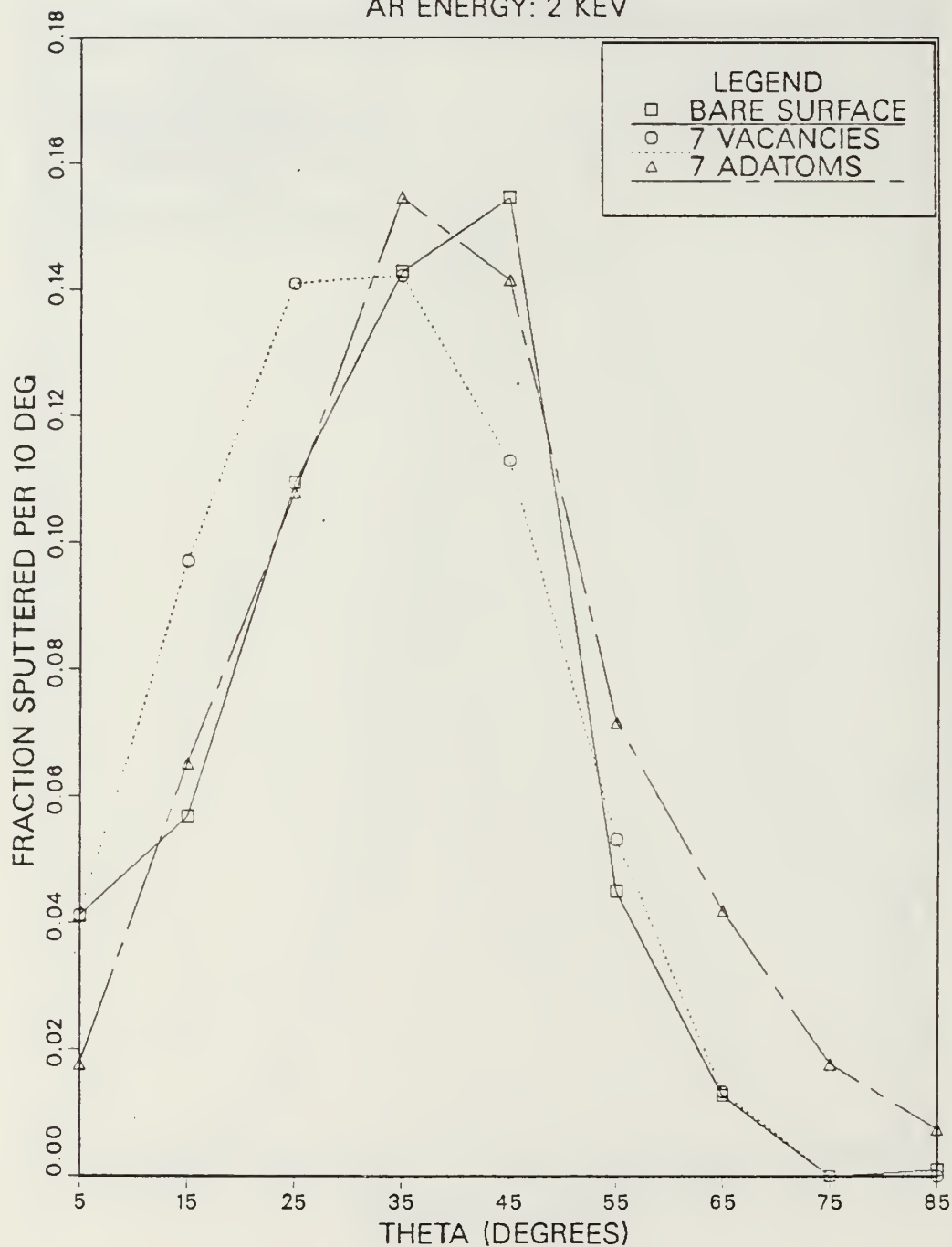


Fig. 33 Ejected Atom Angular Distribution.

ANGULAR TALLY: RH ENERGY > 5 EV

AR ENERGY: 500 EV

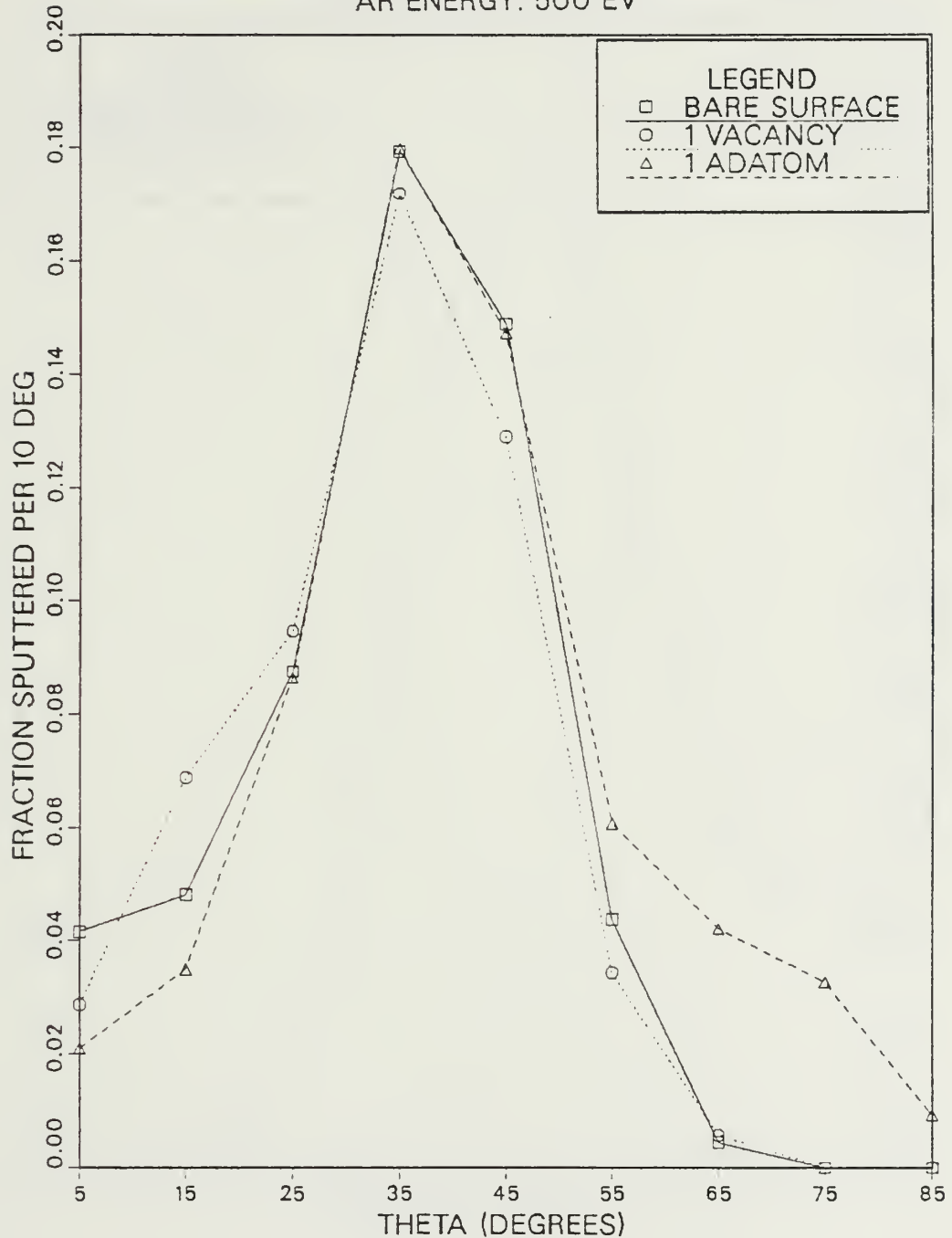


Fig. 34 Ejected Atom Angular Distribution.

ANGULAR TALLY: RH ENERGY > 5 EV

AR ENERGY: 500 EV

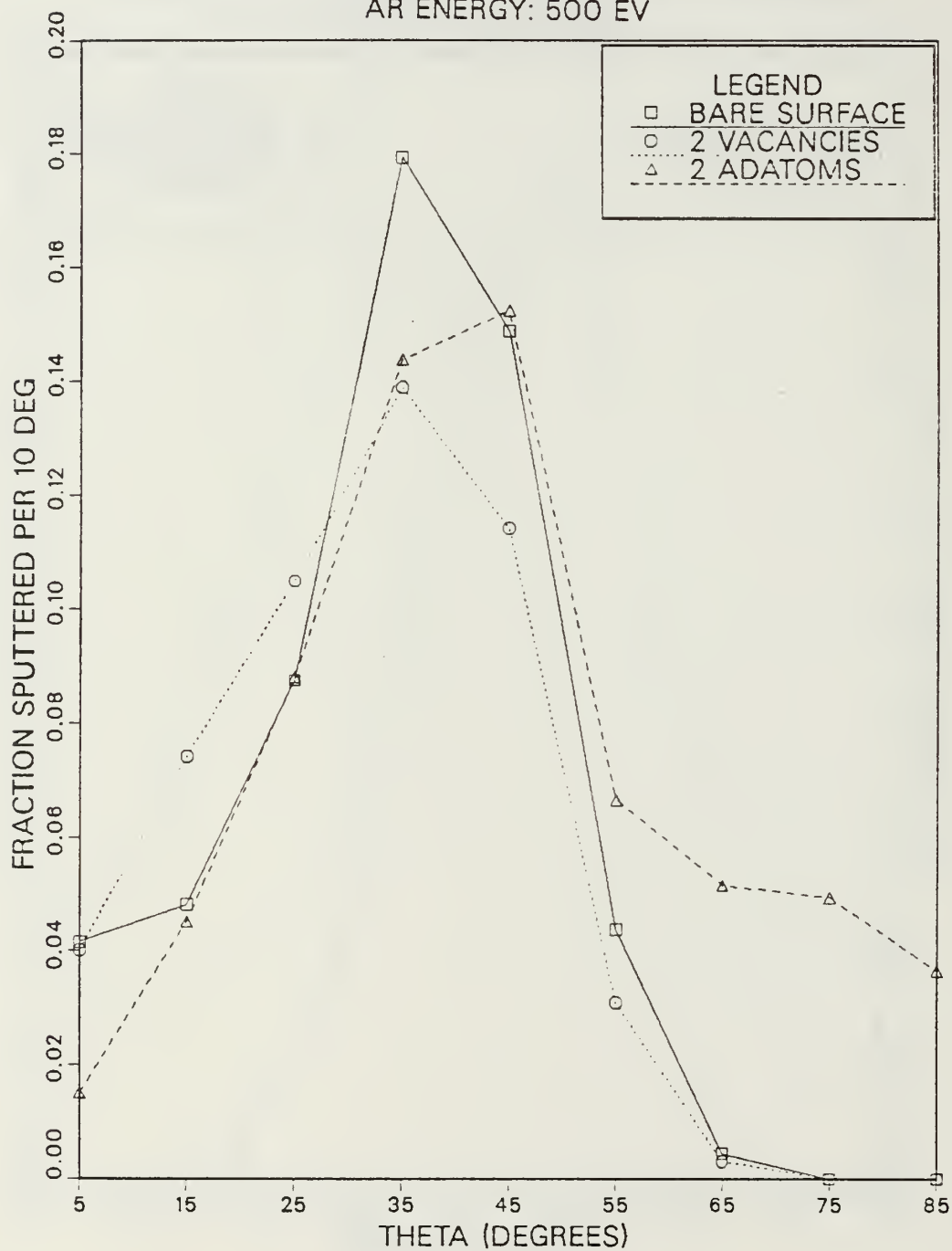


Fig. 35 Ejected Atom Angular Distribution.

ANGULAR TALLY: RH ENERGY > 5 EV

AR ENERGY: 500 EV

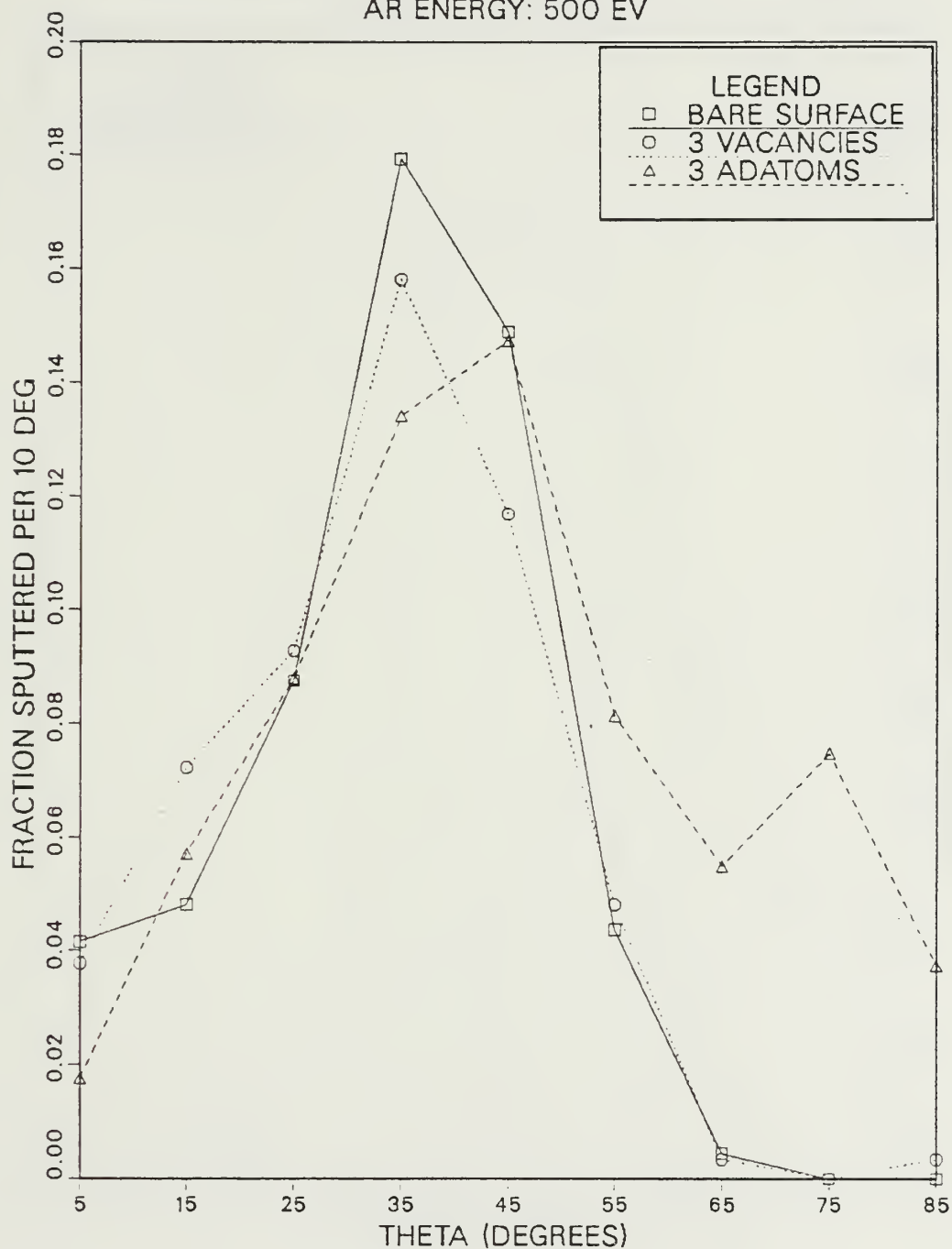


Fig. 36 Ejected Atom Angular Distribution.

ANGULAR TALLY: RH ENERGY > 5 EV

AR ENERGY: 500 EV

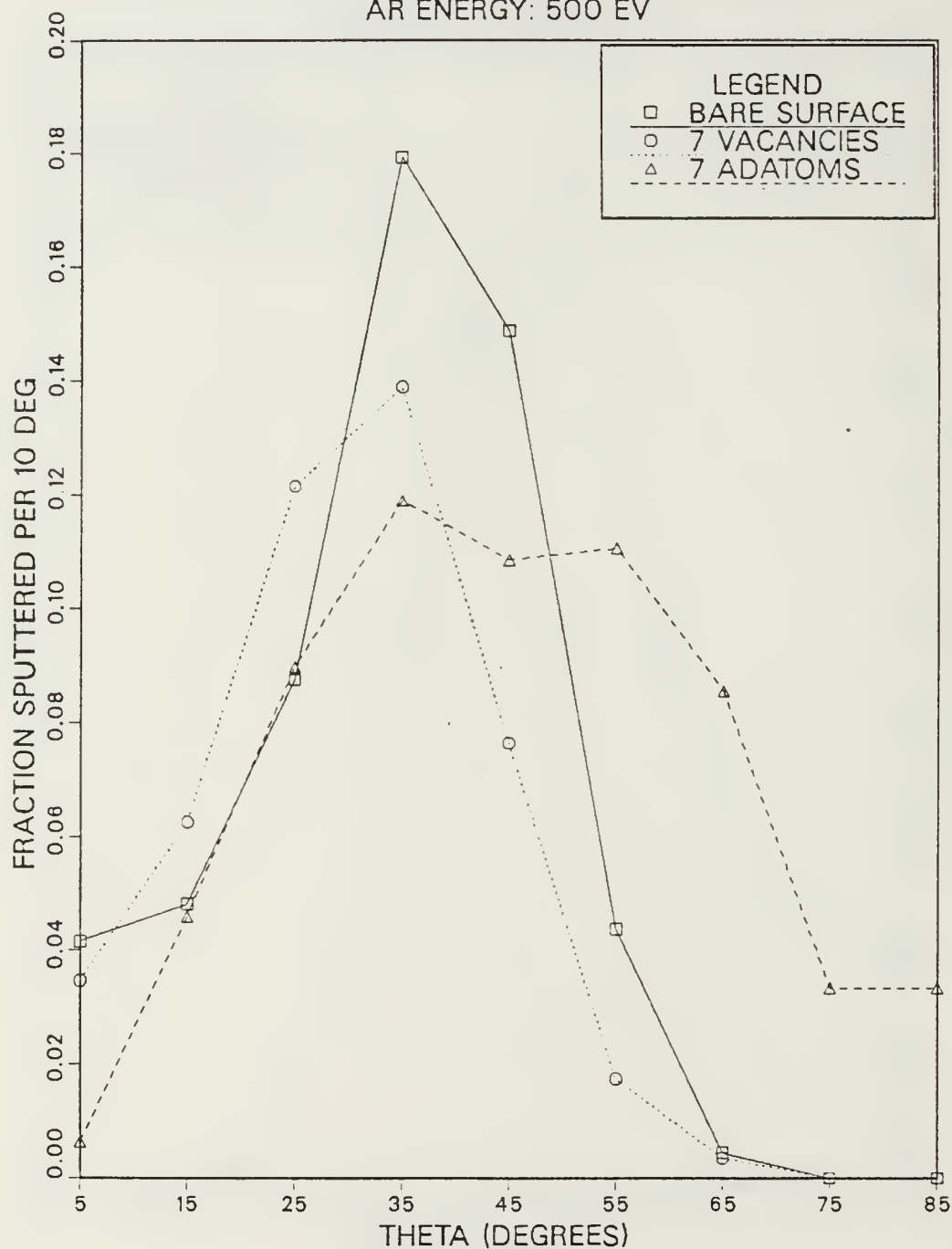


Fig. 37 Ejected Atom Angular Distribution.

ANGULAR TALLY: RH ENERGY > 5 EV

AR ENERGY: 2 KEV

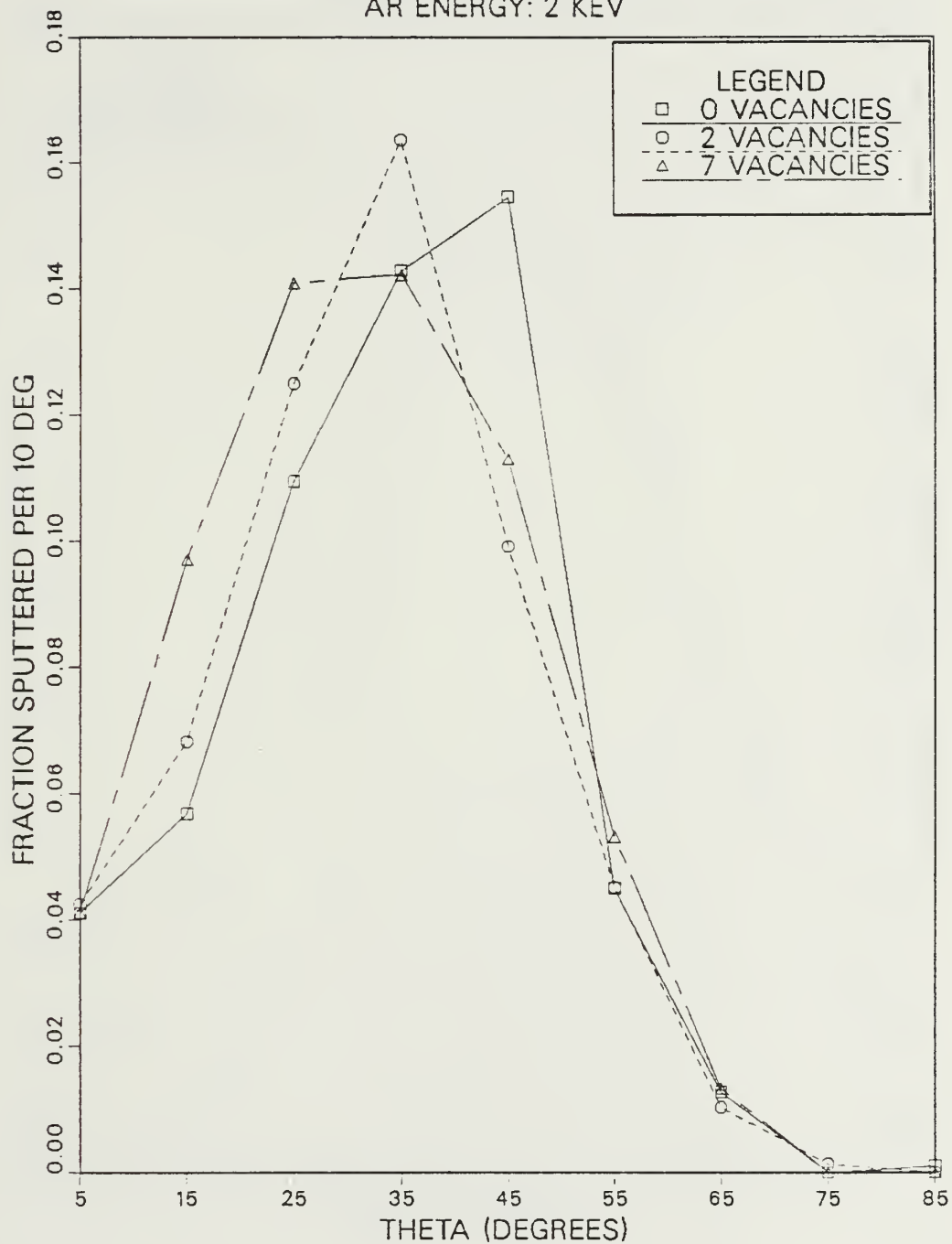


Fig. 38 Ejected Atom Angular Distribution.

ANGULAR TALLY: RH ENERGY > 5 EV

AR ENERGY: 2 KEV

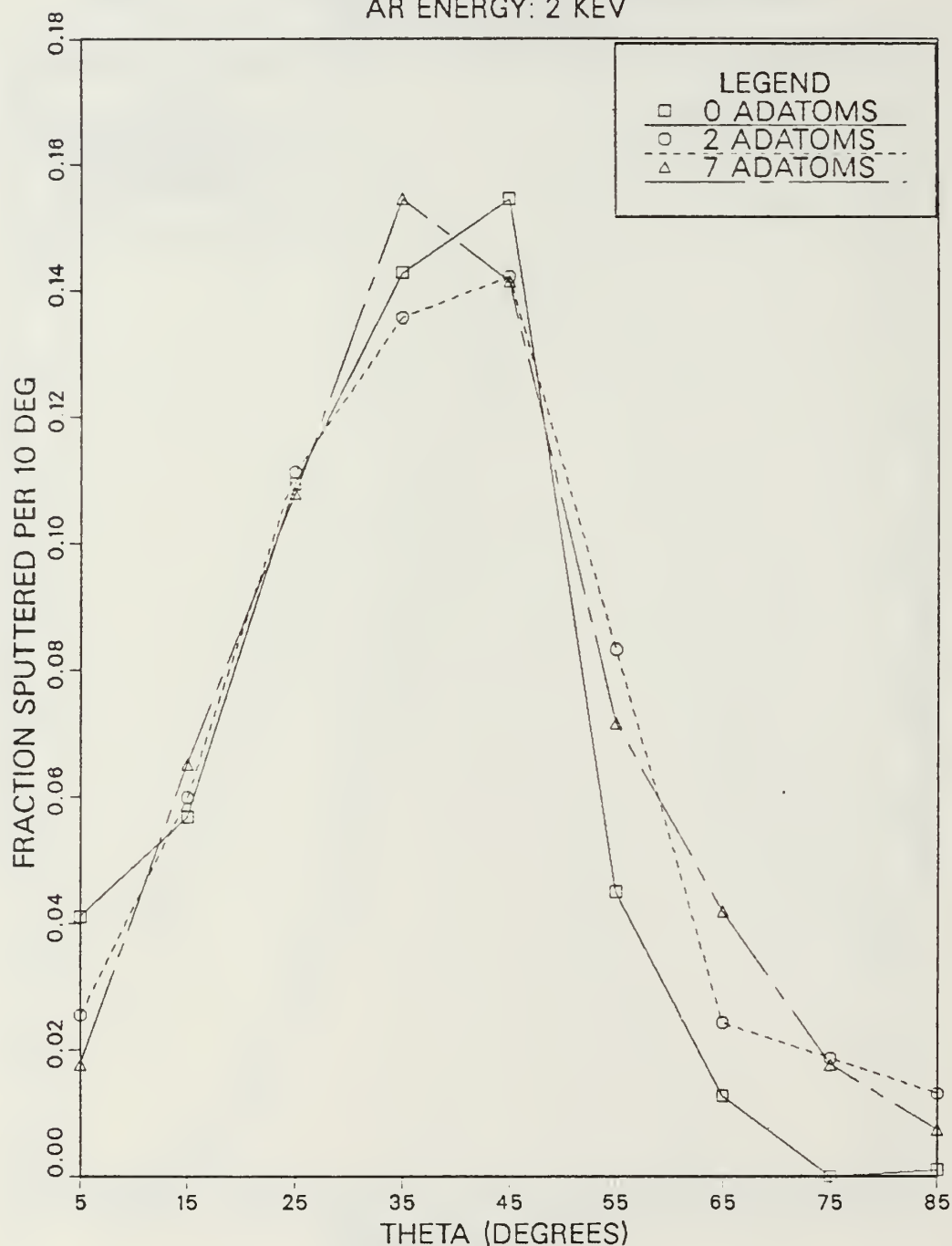


Fig. 39. Ejected Atom Angular Distribution.

ANGULAR TALLY: RH ENERGY > 5 EV

AR ENERGY: 500 EV

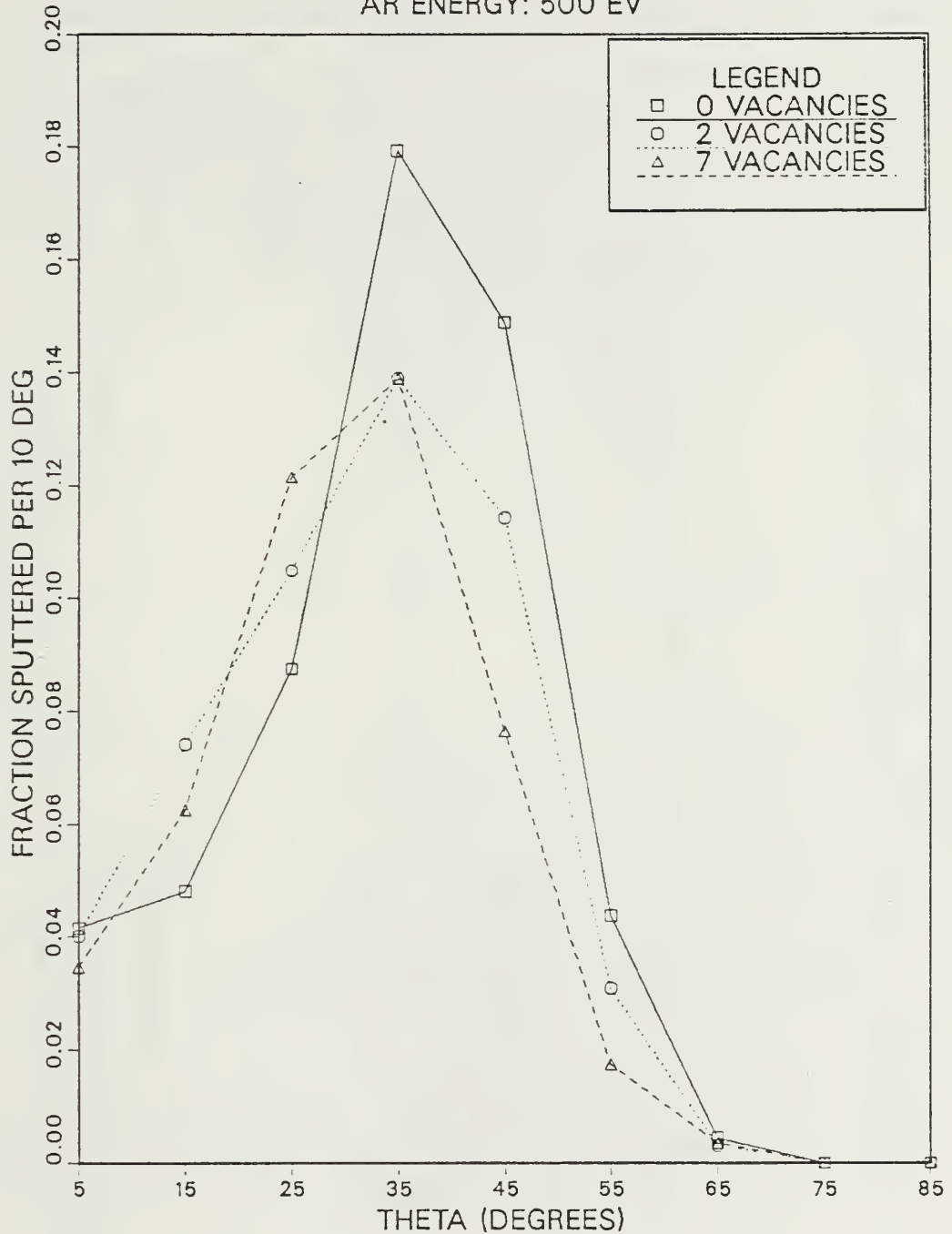


Fig. 40 Ejected Atom Angular Distribution.

ANGULAR TALLY: RH ENERGY > 5 EV

AR ENERGY: 500 EV

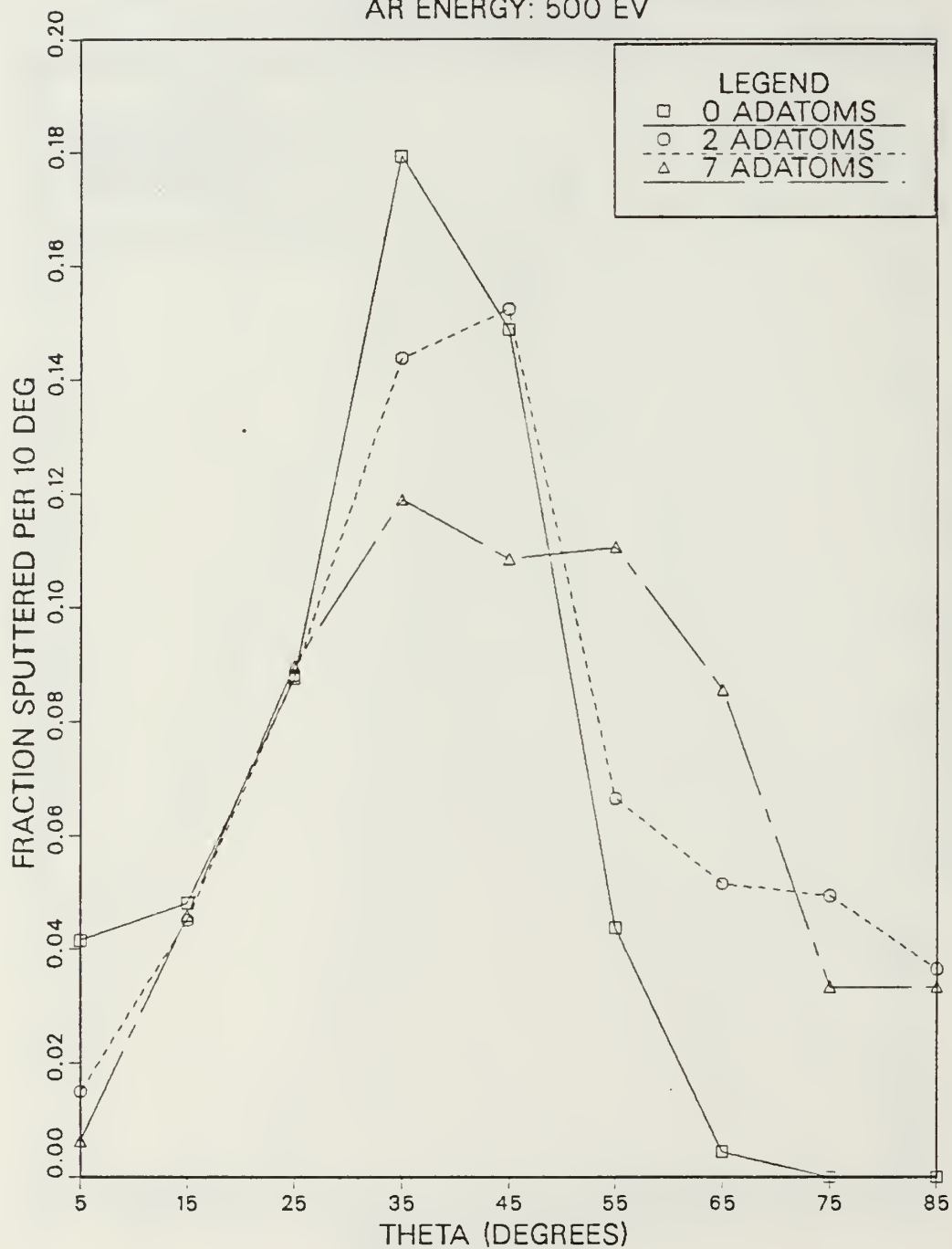
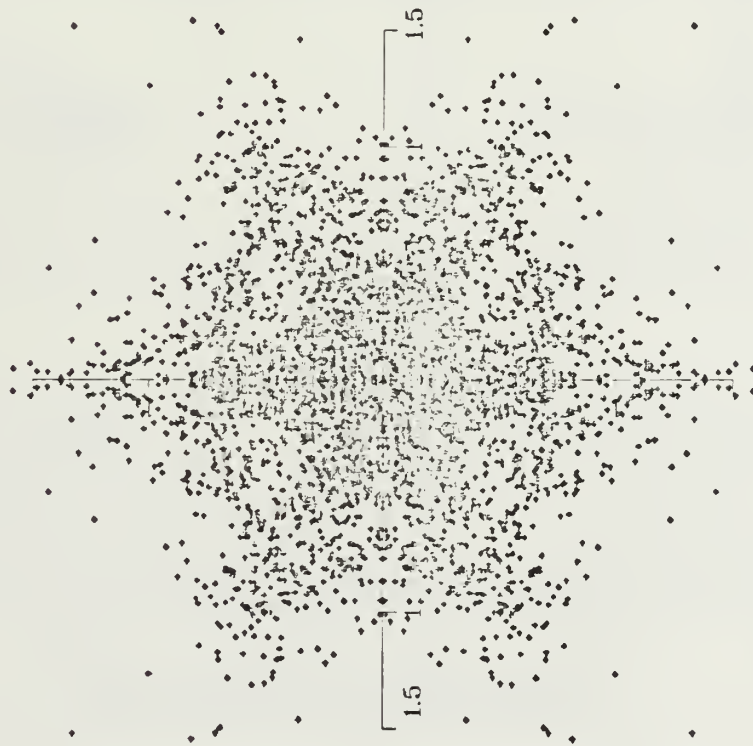


Fig. 41 Ejected Atom Angular Distribution.

500EV RH(111)/AR<111> CLEAN SURFACE

SPOT PATTERN



2KEV RH(111)/AR<111> CLEAN SURFACE

SPOT PATTERN



Fig. 42 Spot Patterns.

ATOMS PER SINGLE ION, CLEAN SURFACE

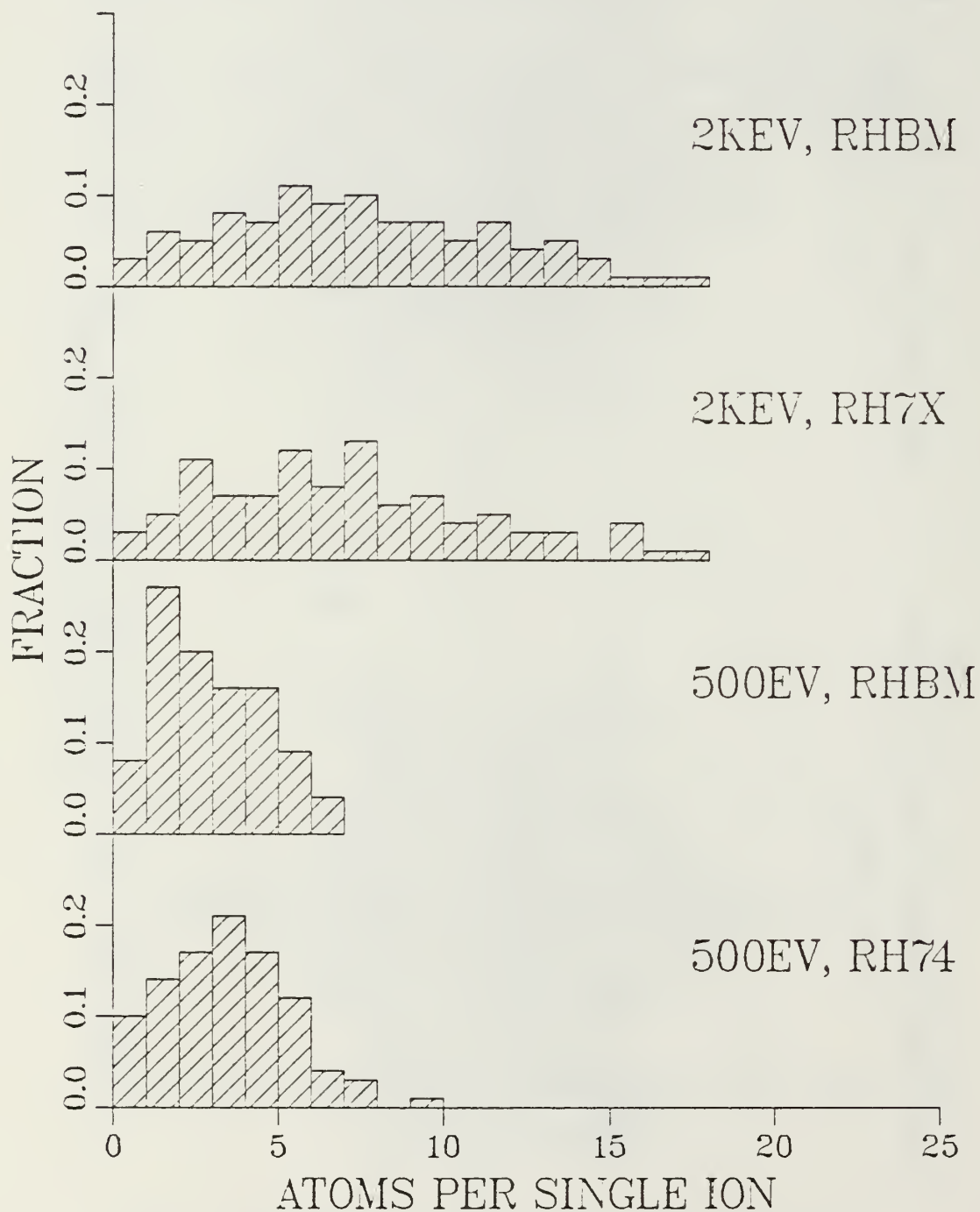


Fig. 43 Atoms per Single Ion Distribution.

TIME DISTRIBUTION, CLEAN SURFACE

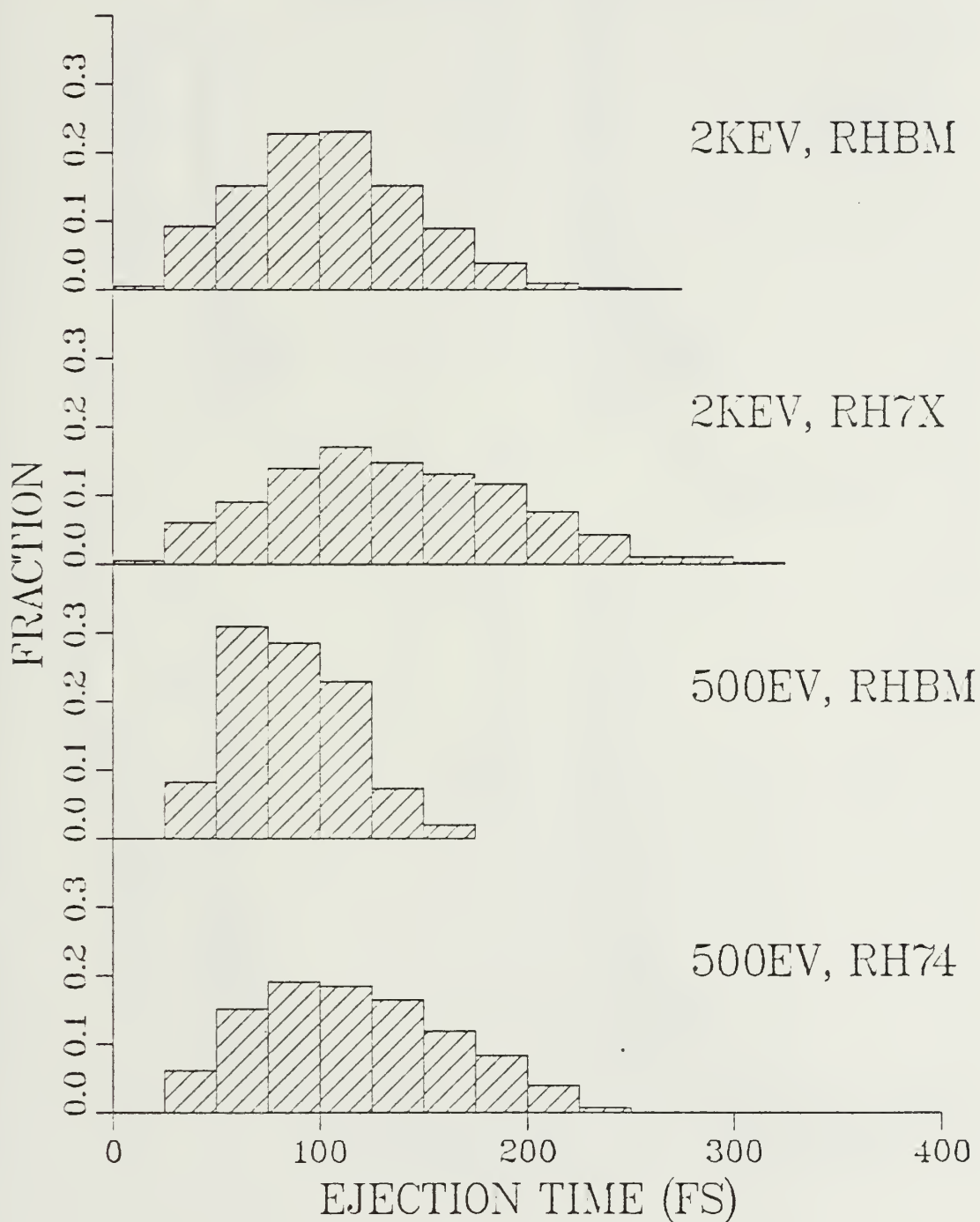


Fig. 44 Atom Ejection Time Distribution.

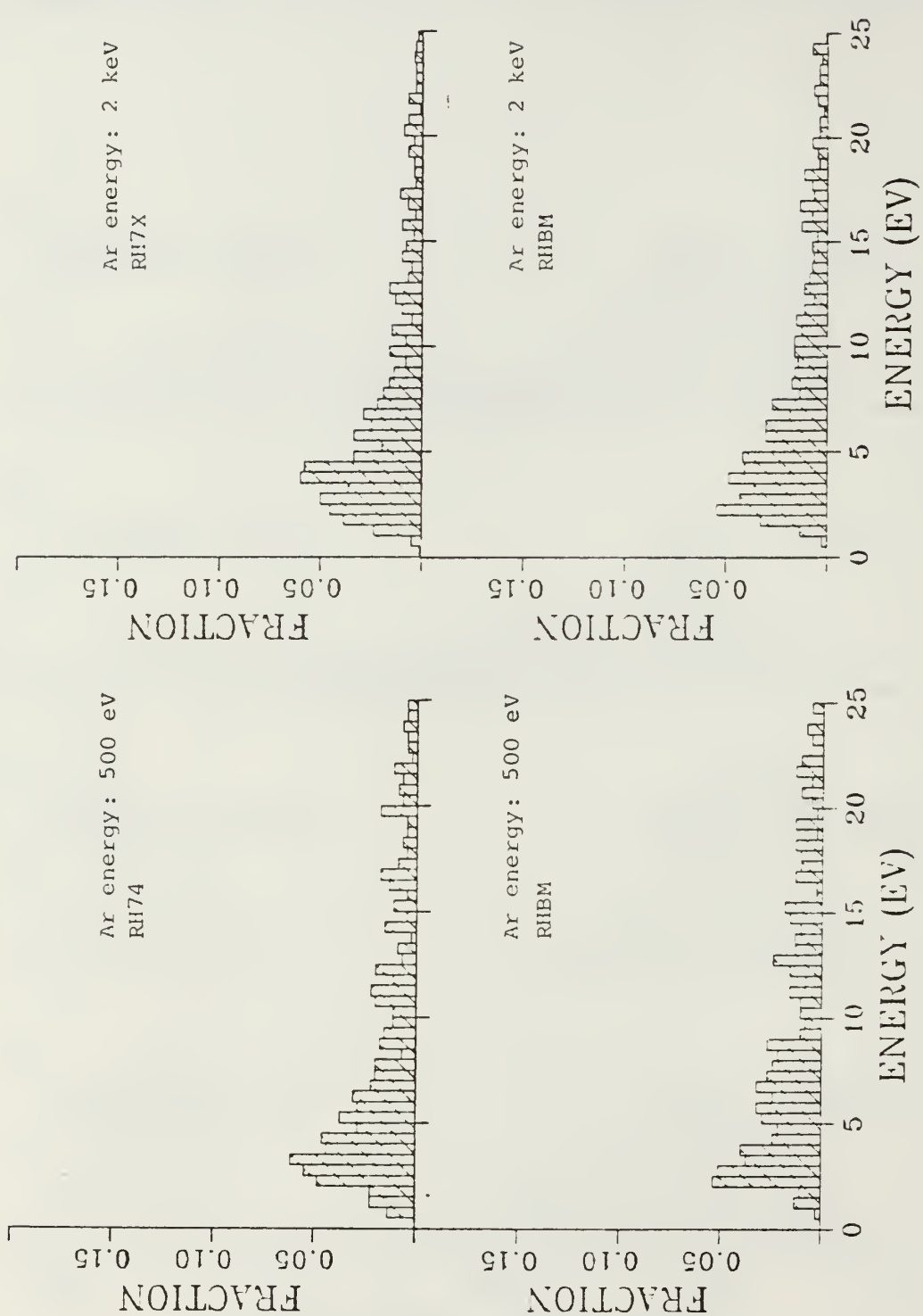


Fig. 45 Ejected Atom Energy Distribution.

ANGULAR TALLY: RH ENERGY > 5 EV

CLEAN SURFACE, AR ENERGY: 500EV

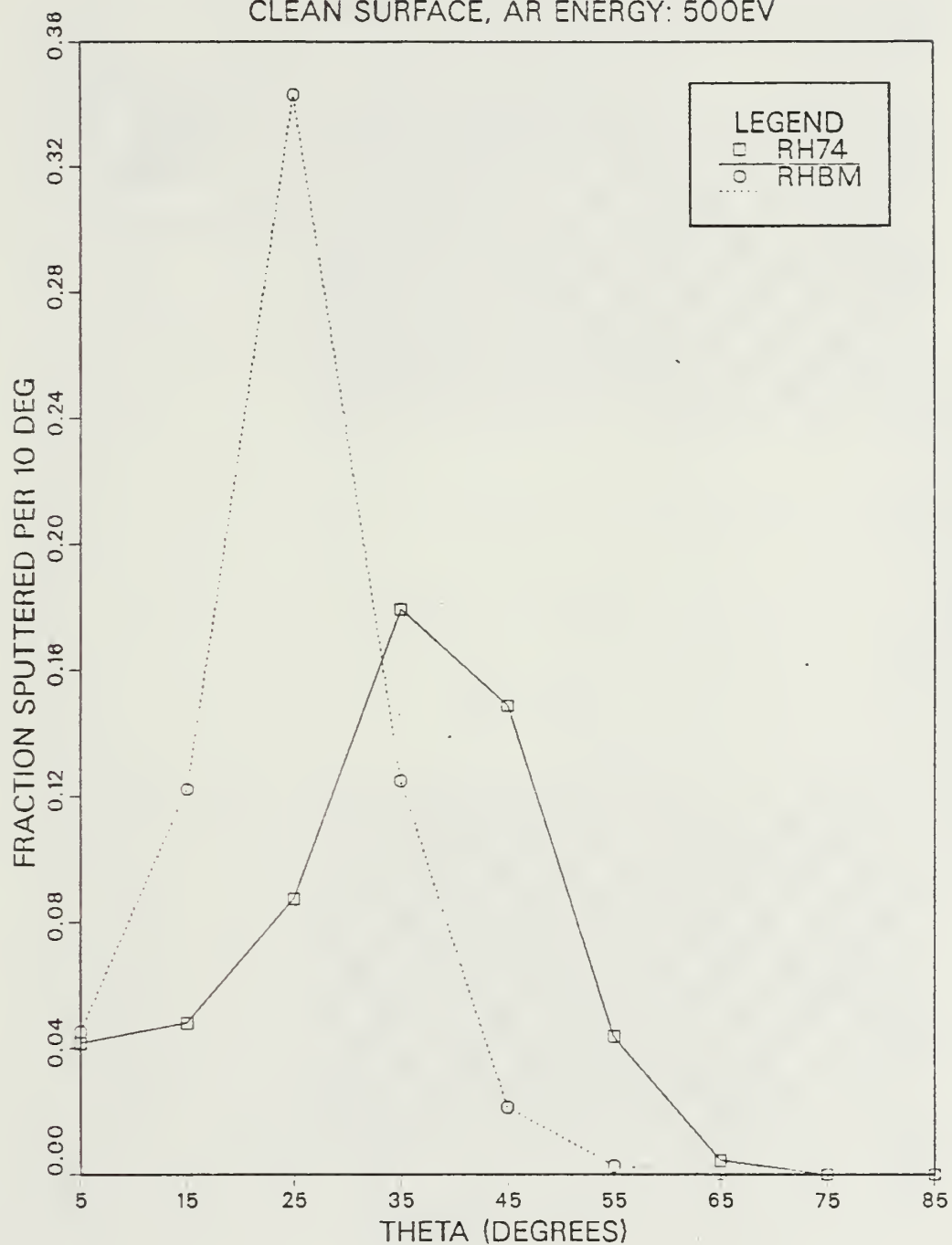


Fig. 46 Ejected Atom Angular Distribution.

ANGULAR TALLY: RH ENERGY > 5 EV

CLEAN SURFACE, AR ENERGY: 2KEV

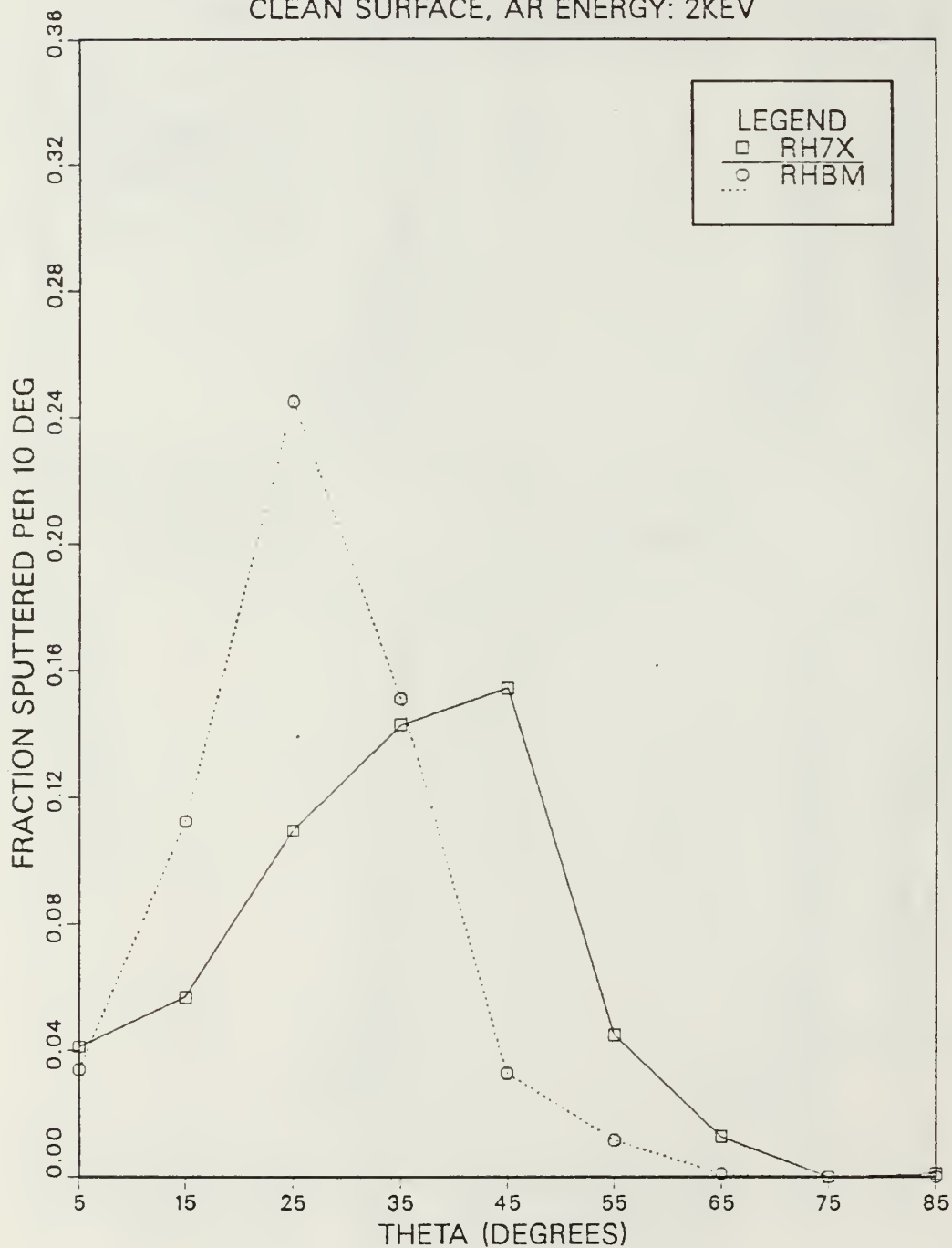


Fig. 47 Ejected Atom Angular Distribution.

500EV RH(111)/AR<111> CLEAN SURFACE
 ATOM YIELD PER IMPACT POINT

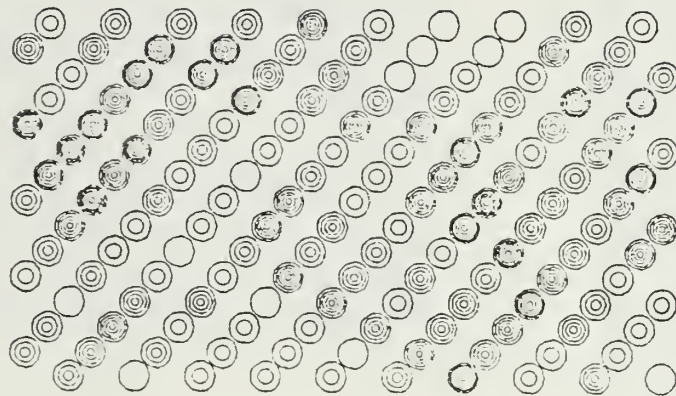
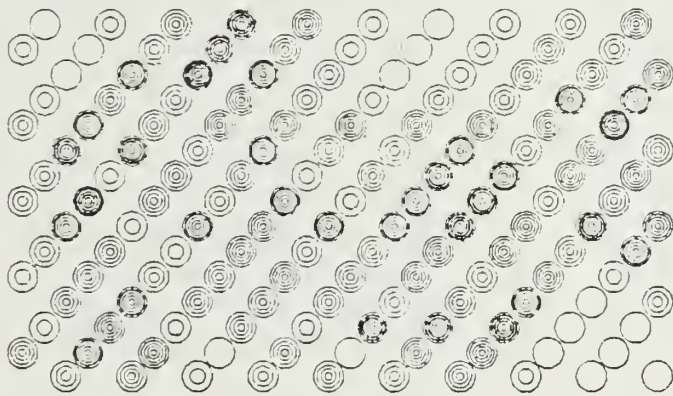
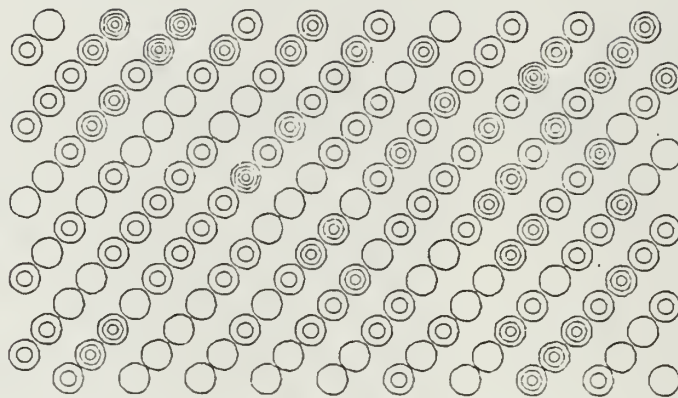


Fig. 48 Atom Yield per Impact Point.

2KEV RH(111)/AR<111> CLEAN SURFACE (RHBM)
 ATOM YIELD PER IMPACT POINT



2KEV RH(111)/AR<111> CLEAN SURFACE
 ATOM YIELD PER IMPACT POINT

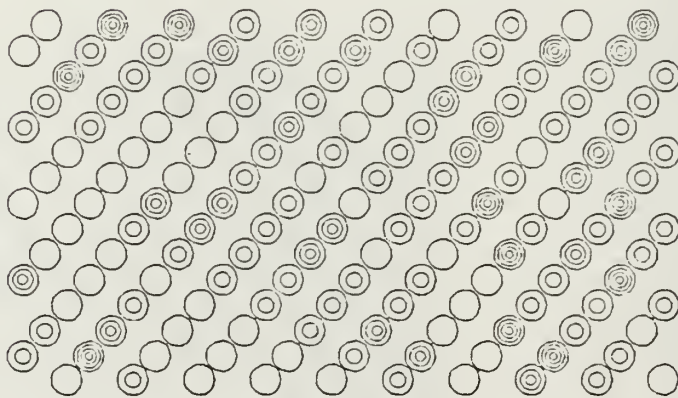


Fig. 49 Atom Yield per Impact Point.

INITIAL DISTRIBUTION LIST

	No. Copies
1. Defense Technical Information Center Cameron Station Alexandria, Virginia 22304-6145	2
2. Library, Code 0142 Naval Postgraduate School Monterey, California 93943-5002	2
3. Professor D. E. Harrison, Jr., Code 61HX Naval Postgraduate School Monterey, California 93943-5000	12
4. Department of the Navy Attn: CDR Offerle Office of the Chief of Naval Operations (OP-981N1) Washington, District of Columbia 20350-2000	1
5. Mr. Lyle Cox, L-24 University of California Lawrence Livermore National Laboratory P. O. Box 808 Livermore, California 94550	1
6. LT Steven G. Miller 279 Northwood Commons Livermore, California 94550	4

18070

2

67

DUDLEY KNOX LIBRARY
NAVAL POST GRADUATE SCHOOL
MONTEREY, CALIFORNIA 95043-5002

221109

Thesis
M591
c.1

Miller
A molecular dynamics
simulation study of small
scale surface defects
upon atom ejection pro-
cesses.

221109

Thesis
M591
c.1

Miller
A molecular dynamics
simulation study of small
scale surface defects
upon atom ejection pro-
cesses.

thesM591

A molecular dynamics simulation study of



3 2768 000 75934 4

DUDLEY KNOX LIBRARY